ANION-Π COMPLEXES AND ELECTRON-TRANSFER REACTIONS OF p-BENZOQUINONES WITH HALIDE ANIONS

A THESIS

SUBMITTED TO THE GRADUATE SCHOOL

IN PARTIAL FULFILLMENT OF THE REQUIREMENTS

FOR THE DEGREE

MASTERS OF SCIENCE

BY

MATT KEPLER

DR. SERGIY ROSOKHA – ADVISOR

BALL STATE UNIVERSITY

MUNCIE INDIANA

MAY 2019

ABSTRACT

THESIS: Anion-π Complexes and Electron-Transfer Reactions of p-Benzoquinones with Halide Anions

STUDENT: Matt Kepler

DEGREE: Master of Science

COLLEGE: Science and Humanities

DATE: May 2019

PAGES: 91

Anion-π bonding, the counter-intuitive attraction of anions to electron-deficient π-systems, has recently become a subject of significant interest. Many works have demonstrated its considerable potential for anion sensing and transport, as well as for catalysis. However, although this interaction has been observed in many solid-state structures recently, characterization of anion-π complexes in solutions are very rare. p-Benzoquinones are known to be very important electron acceptors in chemical and biochemical systems, for example in the electron transport chain, and have potential to participate in anion-π interactions. Even so, investigations of their participation in anion-π bonding are scarce. In this work, interchange between complex formation and electron-transfer reactions between halide anions and a series of p-benzoquinones were established via UV-Vis spectral and x-ray structural measurements. Solution-phase interaction of p-benzoquinone acceptors with chloride (Cl^-), bromide (Br^-), or iodide (I^-) donors led to formation of anion-π complexes showing strong absorption bands in the UV-Vis range. Formation constants and calculated interaction energies of these complexes increased and donor/acceptor interatomic separations decreased with the increase of p-benzoquinone reduction potentials. Mulliken correlation indicated charge-transfer nature of these anion-π associates. Most notably, an increase in π-acceptor strength led to transition between formation of the persistent anion-π complexes to electron-transfer reactions. Thermodynamic analysis accounted for the experimental observations of radical anions and trihalide anions in solutions of p-benzoquinones with strong I^- or (for the strongest acceptor) Br^- donors. Kinetics of these processes indicated that anion-π complexes represent critical intermediates of

redox reactions. In contrast to Cl^-, Br^-, or I^-, interaction of p-benzoquinones with fluoride (F^-) anions led to formation of σ-complexes, and appearance of radical anions in such systems was related to the follow-up reactions of these complexes.

ACKNOWLEDGEMENTS

First and foremost, I would like to thank my research advisor, Dr. Sergiy Rosokha, for teaching me much this past year. I would also like to thank Brandon Watson, Olivia Grounds, and Jon Hager of the Rosokha research group, the first two for their work in the purification of several halide salts I used during my research, and the latter for his work with DDQ/halide interactions before me.

Thanks to Amar Kumar and Emoke Lukacs for their preliminary UV-Vis measurements of DDQ with chloride anions as well as crystallization of the [DDQ, Cl^-] complex, and also to Charlotte Stern for the x-ray crystallography measurements of this complex. Thanks as well to Matthias Zeller for x-ray crystallography measurements of the structures included in my research.

TABLE OF CONTENTS

LIST OF FIGURES, TABLES, AND EQUATIONS

Figures

Tables

Equations

CHAPTER 1: INTRODUCTION AND LITERATURE REVIEW

I. Anion-π interactions: definition, importance, and examples

Noncovalent bonding is an important phenomenon in chemical systems, for example in the assembly and stabilization of supramolecular structures and for designing anion sensor molecules. Well-known examples are π-π stacking which occurs between nucleic acid base pairs in DNA and stabilize its structure,[1] and hydrogen bonding, which is critical for maintaining the folded structure of proteins.[2] Anion-π interactions (also called anion-π bonding or the formation of the anion-π complex) is another class of noncovalent bonding which was recognized by chemists only during the last couple decades.

Anion-π bonding is frequently compared to the better known cation-π bonding, the noncovalent reversible attraction of a cation to a π-system. This can be attributed to the easily discernable nature of its interaction: since π-systems are generally thought of as being electron-rich in nature, the electrostatic attraction of an electron-deficient cation to it is a straightforward conclusion. This interaction is exemplified by the attraction of a given cation to benzene, which has a negative quadrupole moment (Figure 1-1A).

Anion-π bonding is the inverse of cation-π bonding. It is the reversible interaction between an anion and a π-system which has been made electron-deficient (referred to as a π-acceptor in this case). A common approach to make a π-system more electrophilic is through the addition of electron-withdrawing substituents. By changing benzene from the above example to hexafluorobenzene, electron density is drawn away from the π-bonds, making the quadrupole moment of the molecule positive (Figure 1-1B). An early theoretical study demonstrated that hexafluorobenzene attracts various mono- and polyatomic anions, including some of the halides (X^-) used in this work, and found that these interactions are energetically favorable.[3] This in part has spurred other groups into looking past the counterintuitive nature of anion-π interactions and has encouraged experimental studies that have helped to unravel the nature of the attraction, determine its importance, and discover its potential applications.

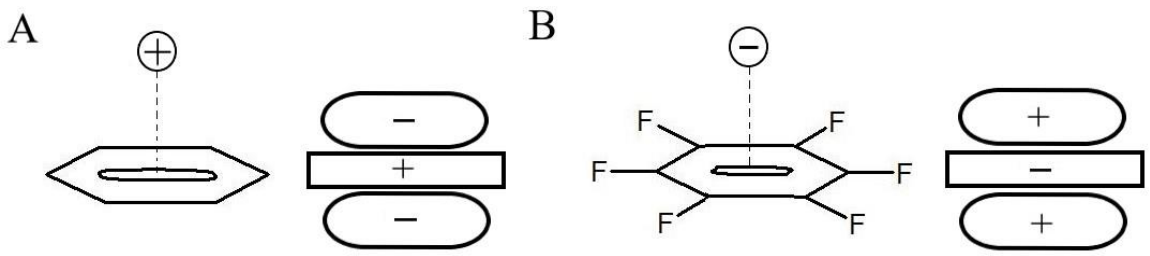

Figure 1-1. The electrostatic nature of cation-π and anion-π interactions. **A)** Interaction of a benzene molecule with a cation. Figure on the right shows benzene's negative quadrupole moment above and below the plane of the ring, making attraction to a cation favorable. **B)** Interaction of a hexafluorobenzene molecule with an anion. Figure on the right shows hexafluorobenzene's positive quadrupole moment, making attraction to an anion favorable.

Anion-π interactions are partially influenced by the quadrupole moment of the π-system, as previously mentioned. The more positive the quadrupole moment, the stronger the interaction with anions. The ability of the π-system to be polarized is also an important quality because an easily polarized compound can still form a complex with an anion, even if its quadrupole is less positive. An anion in the vicinity of a polarizable system can push its electron density away, creating an area of positive charge in the space adjacent to the anion. This factor becomes increasing important in examples where a cation is interacting simultaneously on the opposite side of the compound.[4]

A recent paper found that along with electrostatics and polarizability, the HOMO-LUMO overlap between the anion donor and π-acceptor facilitates an anion-π interaction.[5] This suggestion arose when it was noticed in crystal structures of anion-π bonded complexes that there were several instances where the anion was not located over the most positive area of the π-system, which many times is ring centroid. Instead, the anion would often be offset from the center of the ring, even as far as over the bonds of the π-system. The report focused specifically on the interaction of tetracyanopyrazine (TCP) with different halide anions. TCP was previously studied and found to be a strong π-acceptor for forming anion-π complexes. It was shown that the halides interacting with TCP did so over the carbon-carbon bonds of the

ring or over the carbon-nitrile bonds, which fits well with the HOMO-LUMO orbital interaction of the two species calculated from computational studies.

Along with computational studies and the solid-state crystallographic analysis of anion-π bonding, information about anion-π complexes were in rare cases also collected from solution-phase measurements. In particular, a study of the interaction of TCP and different halides using UV-Vis spectroscopy showed that anion-π bonding resulted in the formation of a new broad band in the spectrum. For the TCP/Br^- interaction, for example, a band formed and grew in intensity as halide concentration increased with a peak absorption (λ_{max}) at 400 nm, while previously neither reactant had absorbed above 300 nm.[6] A Mulliken correlation was graphed, plotting the energy of the absorption band against the reduction potential (E_{red}) of several π-acceptors, and the relationship was very linear (Figure 1-2). The Mulliken correlation showed that as E_{red} decreases, there is a linear increase in the energy of the anion-π complex, which indicated that the formation of the complex is related to the HOMO-LUMO interaction.

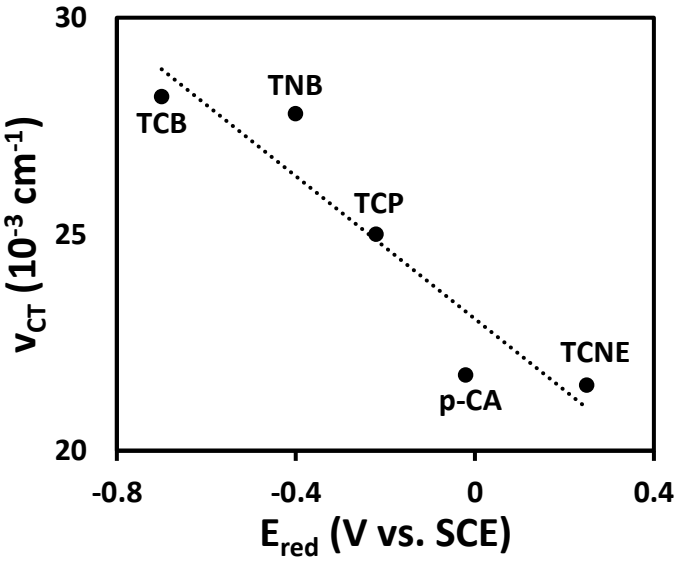

Figure 1-2. Mulliken correlation between the energy of absorption bands of anion-π complexes formed upon interactions of Br^- with different π-acceptors and the reduction potential (E_{red}) of these acceptors (TCB: tetracyanobenzene, TNB: trinitrobenzene, p-CA: p-chloranil, TCNE: tetracyanoethylene).

With the understanding behind the nature of anion-π interactions growing exponentially, many groups began looking into its applications. Some of the usages being investigated are in the fields of anion-sensing, synthetic transmembrane channels, and electron-transfer catalysis.

Traditionally, molecular receptors have employed noncovalent interactions (including everything from hydrogen bonding to hydrophobic properties) because of their reversibility. One of the first groups to utilize anion-π bonding for anion sensing prepared two similar sensor (host) molecules: one comprising an electron-deficient π-system and one without (Figure 1-3). The study of the interactions of these molecules with halides showed that only the molecule containing an electron-poor aromatic ring bonded halides (with equilibrium constants from 20-34 M^{-1}) while the other did not show substantial binding.[7]

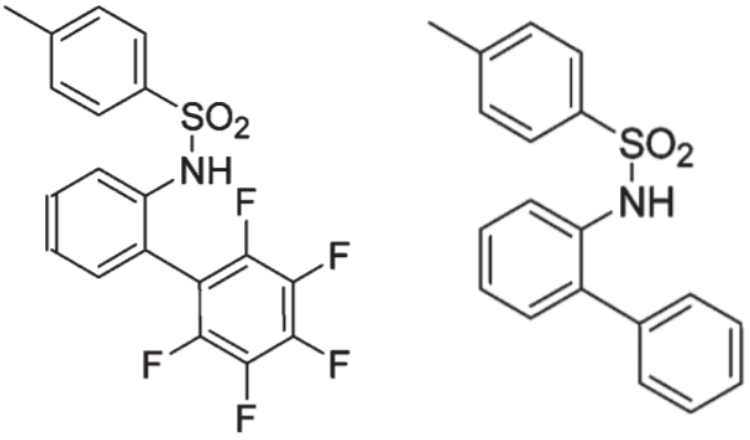

Figure 1-3. Molecules designed for use as anion sensors. Both were tested for their efficacy at binding halide anions (Cl^-, Br^-, I^-) via ^1H NMR titrations and only the first molecule showed a moderate interaction ability (K_{eq} of 30, 20, and 34 respectively) due to its anion-π bonding ability with its electron deficient ring.

The novel use of anion-π interactions in the design of cellular transmembrane "slides" is one of the more ambitious applications since anion-π bonding has not been found to occur naturally in membrane channel proteins. A group looking to develop such synthetic channels as possible treatment for diseases that target membrane channels (e.g. cystic fibrosis) constructed oligo-(p-phenylene)-N,N-naphthalene-diimide (O-NDI) rods that showed an ability for transporting halides, with selectivity following the trend

$Cl^- > F^- > Br^- > I^-$.[8] The molecules were synthesized specifically to have the NDI cores extremely electron-deficient in nature, helping to create a large positive quadrupole that could interact with the halides strongly enough via anion-π interactions to transport anions across the membrane, but not strongly enough to irrevocably bind them (Figure 1-4).

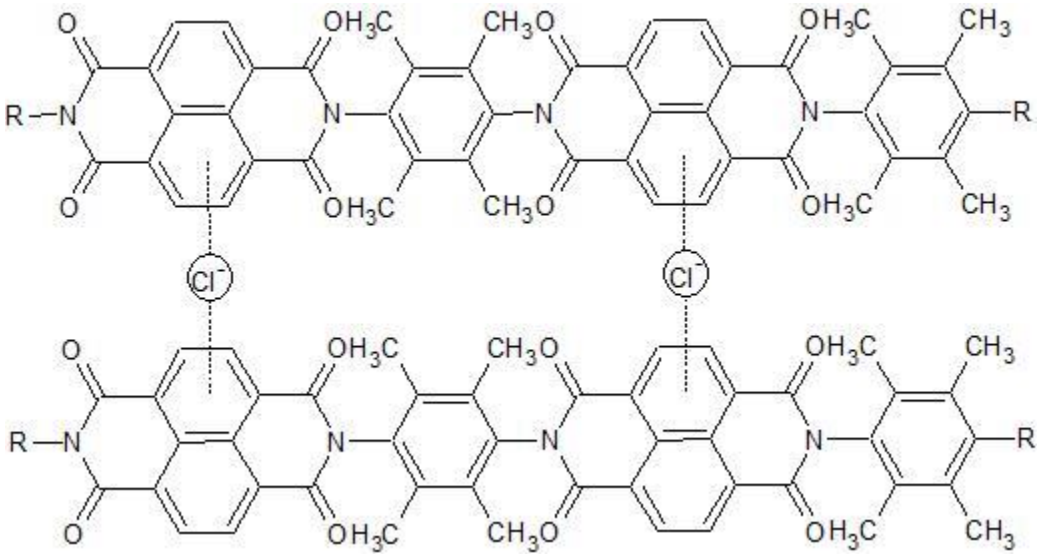

Figure 1-4. Design for transmembrane channels using O-NDI rods showing the synthetic channel constructed to use anion-π interactions for selectively transporting halides.

Lastly, several studies have discovered that in some instances the formation of an anion-π complex could be a precursor for electron transfer. For example, one group investigated reactions of 1,4,5,8,9,11-hexaazatriphenylenehexacarbonitrile ($HAT(CN)_6$) with halide anions. They observed one-electron reduction of acceptor to its radical anion or two-electron reduction to its dianion by different anions.[9] The spectra of both products were obtained via electrolysis, and when the spectra of solutions containing $HAT(CN)_6$ with either OH^- or F^- were compared to them, it was found that both anions could reduce $HAT(CN)_6$ to either species depending on how many equivalents of the anion was added. To determine whether a charge-transfer complex was an intermediate in the reaction, the competitive molecule meso-tetra p-nitrophenyl-tetramethyl calix[4]pyrrole (C4P), a compound known to form strong hydrogen bonds with F^-, was introduced into the $HAT(CN)_6/F^-$ solution to establish whether F^- would still reduce

$HAT(CN)_6$ or if it would complex with C4P (Figure 1-5). It was found that F^- favored complexation, as no radical anion or dianion spectra was observed. From this, it was concluded, although indirectly, that the formation of a noncovalent complex was more favorable than an electron transfer reaction, reinforcing the hypothesis that anion-π complexation is a predecessor and possibly a catalyst for electron transfer.

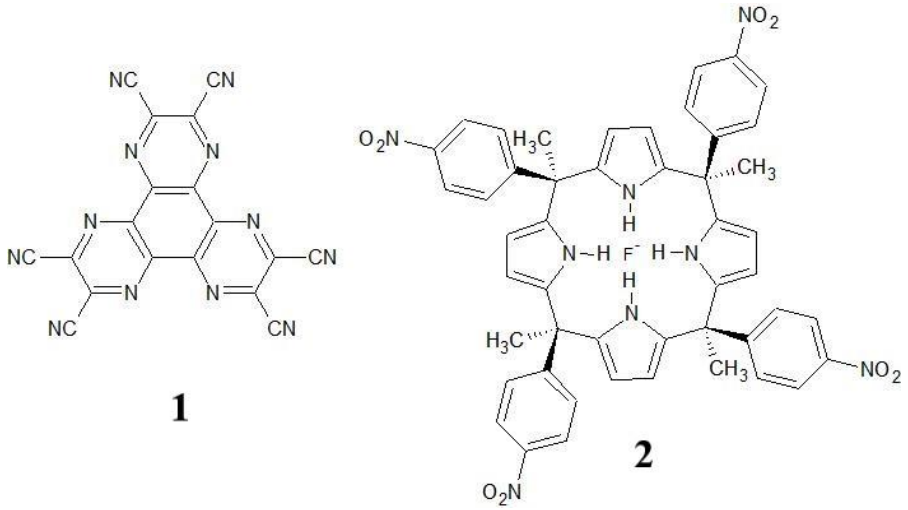

Figure 1-5. $HAT(CN)_6$ molecule (**1**) that was reduced by F^- to its radical anion or dianion. C4P molecule (**2**) that upon addition to $HAT(CN)_6/F^-$ solution forms strong hydrogen bonds with fluoride, preventing reduction of $HAT(CN)_6$. This indirectly shows the formation of a noncovalently-bonded complex is preferable to electron transfer by fluoride.

Although many studies have started looking into the applications of anion-π complexes, characterization of these interactions in solutions remains a challenging task.[10] In most reported solution-phase complexes, anion attraction to a π-system was facilitated and stabilized by hydrogen bonding, electrostatic attraction of the anion to a cationic π-system, and/or multi-dentate coordination of the anionic species with two to four aromatic rings.[7,9] An example of the latter is a study of the interfacing between Br^- and 2,4,6-trisubstituted-1,3,5-triethylbenzene analogues with a total of four electron-deficient rings that should promote anion-π complexation. It demonstrated that that the primary means of interaction between anion and aromatic ring was hydrogen bonding and σ-bonding (Figure 1-6).[11]

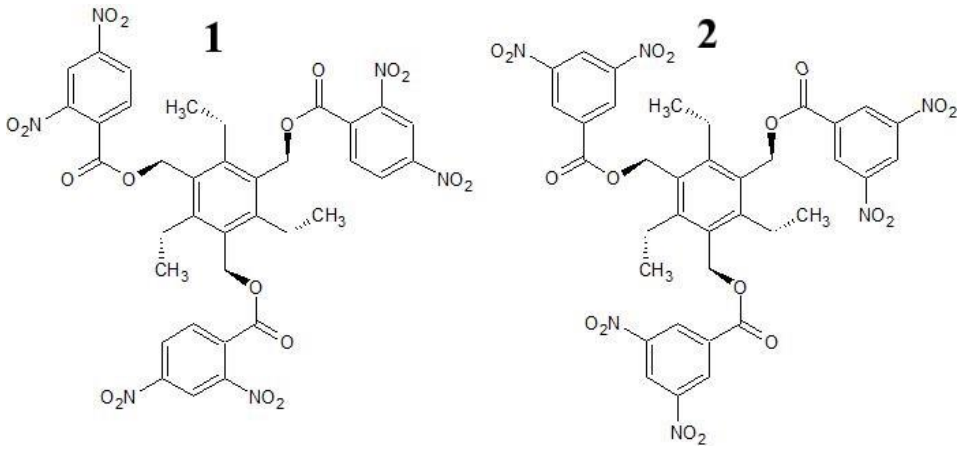

Figure 1-6. Two tri-substituted triethylbenzene (TEB) molecules, one with three substituents containing nitro groups at the 1,3 positions on the benzene ring (**1**) and one with three substituents containing nitro groups at the 2,4 positions on the benzene ring (**2**). Bromide anions interact with **1** primarily through hydrogen bonding and with **2** primarily through weak σ-bonding.

In the literature, there are only a few examples of definitive spectral and thermodynamic characterization of anion-π complexes in the solution phase where the interaction is attributed solely to the attraction of the anion to a neutral π-system. One such example involved the interaction of the aforementioned $HAT(CN)_6$ molecule with Cl^-, Br^-, and I^-.[12] Since $HAT(CN)_6$ has no hydrogens, hydrogen bonding is not an option for these interacting species. The clear Mulliken correlation between the oxidation potential (E_{ox}) of the halides and the energy of the band from the spectra shows, as discussed earlier, the charge-transfer nature of the interactions in these anion-π complexes (Figure 1-7A). The equilibrium constant (K_{CT}) and extinction coefficient (ε_{CT}) data for the interaction is also in the range typically observed for anion-π interactions (Figure 1-7B).

A

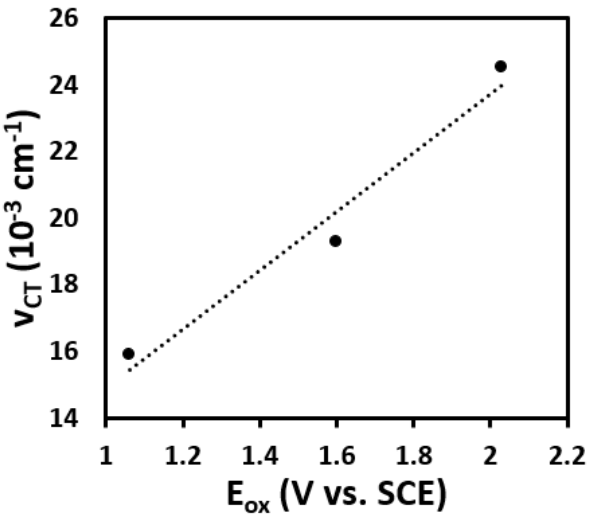

B

	Cl^-	Br^-	I^-
λ_{max} (nm)	408	519	630
K_{CT} (M^{-1})	3780	2200	940
ε_{CT} (M^{-1} cm^{-1})	12785	8258	4437

Figure 1-7. Characteristics of $HAT(CN)_6/X^-$ complexes in THF (X^- = Cl^-, Br^-, I^-). **A)** Mulliken correlation between the energies of absorption bands of complexes and the oxidation potential (E_{ox}) of the halides in acetonitrile. **B)** Table showing spectral and thermodynamic data of the anion-π interactions. λ_{max} is the band peak wavelength, K_{CT} is the equilibrium constant, and ε_{CT} is the extinction coefficient.

Other than this data and that from a handful of other studies, however, characterization of anion-π interactions in solution is sorely lacking. This information is even more crucial since electron-deficient π-systems are very common organic electron acceptors, and many anionic species, such as iodide, are strong electron donors. Therefore, anions were used as reducing agents for preparation of the radical anions of these acceptors. The study of anion-π complexes, therefore, is critical in order to more fully understand the nature of the reactions, especially with π-acceptors that are of great organic and biochemical importance.

II. p- Benzoquinones as electron acceptors in chemical and biochemical systems

p-Benzoquinone (BQ) (Figure 1-8) plays an important role as a core structural unit of redox reagents in many chemical and biochemical systems. It has a one-electron reduction potential (E_{red}) of -0.5V vs. SCE in acetonitrile.[13]

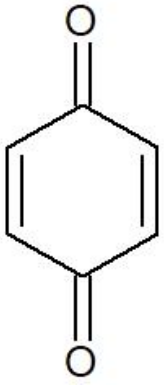

Figure 1-8. Structure of p-benzoquinone (BQ).

In the human body, BQ is essential in the form of the compound ubiquinone (UBQ), also known as coenzyme Q in biological and medical studies (Figure 1-9). UBQ is most well known for its role in aerobic respiration as part of the electron transport chain in the mitochondrial membrane. There, it acts as an electron carrier, undergoing a one-electron reduction by complexes such as NADH and succinate dehydrogenases to its very stable semiquinone radical ($UBQ^{\bullet -}$) or a two electron reduction partnered with addition of two protons to form ubiquinol ($UBQH_2$). Afterwards, $UBQH_2$ transfers those electrons along to the cytochrome b complex, in turn being oxidized back to UBQ. $UBQH_2$ has also been identified as an antioxidant in mammals, helping lower the concentration of harmful oxygen radical species.[14] In both its function in respiration and as an antioxidant, BQ is acting as a redox mediator.

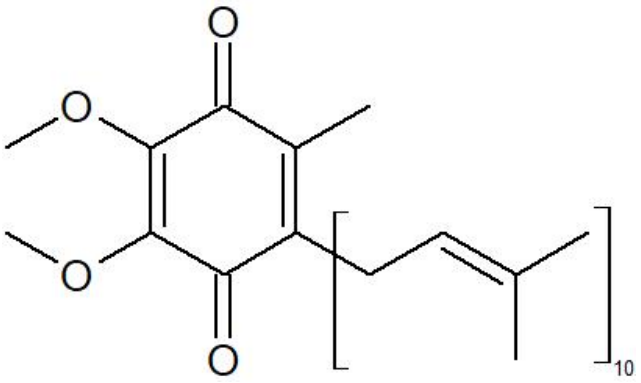

Figure 1-9. Structure of ubiquinone as it appears as coenzyme Q10 in the mitochondrial membrane as part of the electron transport chain for respiration.

Since the discovery of its natural proficiency at performing electron transfer reactions, many studies have harnessed BQs for use as redox reagents in different applications. One such group looked at their potential for increasing the voltage and capacity of Li-O_2 batteries.[15] They discovered that by the addition of 2,5-di-t-butyl-p-benzoquinone (DBBQ) to an aqueous Li-O_2 system, parasitic side reactions related to the formation of LiO_2 were minimized to a great extent. They highlight the importance of the switch from a nonaqueous system to an aqueous one, which caused greater preference for the desired DBBQ/$LiQ^{\bullet}$ and DBBQ/Li_2Q redox reactions. This outcome is attributed partly to DBBQ complexing with water through hydrogen bonding, showing the importance of noncovalent interactions.

Another study used p-benzoquinone for creating more efficient dye-sensitive solar cells.[16] The coupling of hydroquinone (HQ) with BQ in a 1.5:1 ratio worked better as an electrolyte for the cells by 0.4% more than the convential I^-/I_3^- redox couple. This coupling represents the formation of a charge-transfer complex between the good reducing agent HQ and BQ, so noncovalent interactions are once again an important factor in the applications of BQs (Figure 1-10).

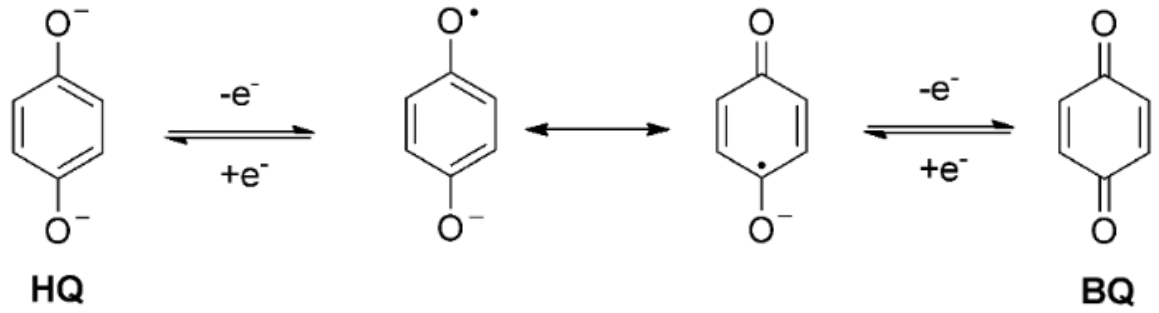

Figure 1-10. Scheme showing the step-by-step electron transfer occuring within the HQ/BQ complex being used as an electrolyte for dye-sensitive solar cells from reference 16.

These previous examples have shown the importance of BQ's noncovalent interactions and electron transfer abilities. Therefore, the study of their anion-π bonding possibilities is of great interest, but before these interactions can occur the BQs must be made electron-deficient. p-Benzoquinone itself has a E_{red} of -0.5V vs. SCE in acetonitrile,[13] which corresponds to a system too electron-rich to favorably interact with anions. Consequently, study of BQs with electron-withdrawing substituents was undertaken (Figure 1-11).

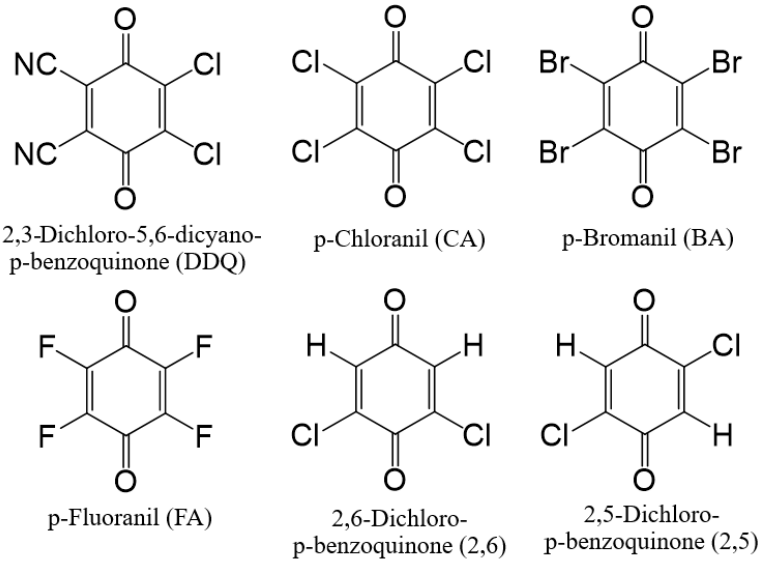

Figure 1-11. Structures and nomenclature of electron-deficient BQs used as π-acceptors in this study.

Changing the substituents on p-benzoquinone from hydrogens to different electron-withdrawing atoms or groups shifted the E_{red} of the BQ to values that are substantially more positive. Electrochemical studies of these compounds using cyclic voltammetry in acetonitrile solvent established that E_{red} values range from about -0.2V vs. SCE for the dichloro-substituted BQs to about 0.5V vs. SCE for the dicyano-dichloro-substituted DDQ (Table 1-1).[13,17]

Benzoquinone	**DDQ**	**CA**	**BA**	**FA**	**2,6**	**2,5**
E_{red} (V vs. SCE)[13,17]	0.52	0.02	0.00	-0.01	-0.18	-0.20
λ_{max} (nm)	375	367	384	337	338	333
ε ($M^{-1}cm^{-1}$)	804	250	283	189	465	245

Table 1-1. Reduction potentials and spectral characteristics of p-benzoquinones.

In addition, previous studies have also shown that one-electron chemical or electrochemical reduction of BQs such as those listed in Table 1-1 results in the formation of relatively stable radical anions. UV-Vis spectral data and, in some cases, X-ray crystal structures of these reduced species were obtained (Figure 1-12).[18,19]

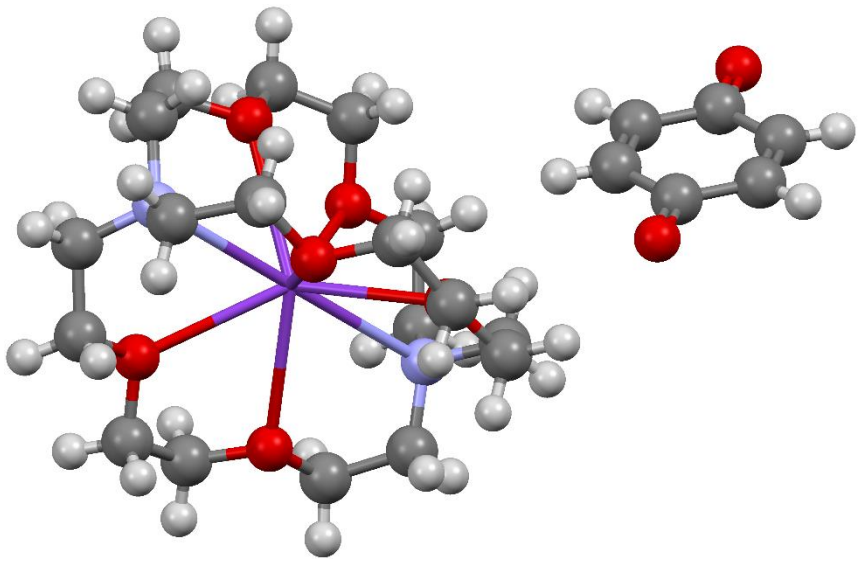

Figure 1-12. X-ray structure showing the crystal structure of [K(crown ether)$^{+}$, BQ$^{\bullet-}$] .

Earlier works reported a large number of charge-transfer complexes involving BQs, including the two above examples of BQ applications.[15,16] The anion-π interactions of the BQs from Table 1-1 with halides, which is a large portion of the study reported here, is a topic of such interest that very recently a different group reported their findings of anion-π contacts between iodides and perhalogenated quinoid rings in co-crystals with organic bases (Figure 1-15).[20] However, the scope of their study was much narrower, focusing on p-chloranil and p-bromanil interactions with iodide in the solid state only. The spectral characteristics of these anion-π complexes in solutions and any connection to electron-transfer processes are lacking.

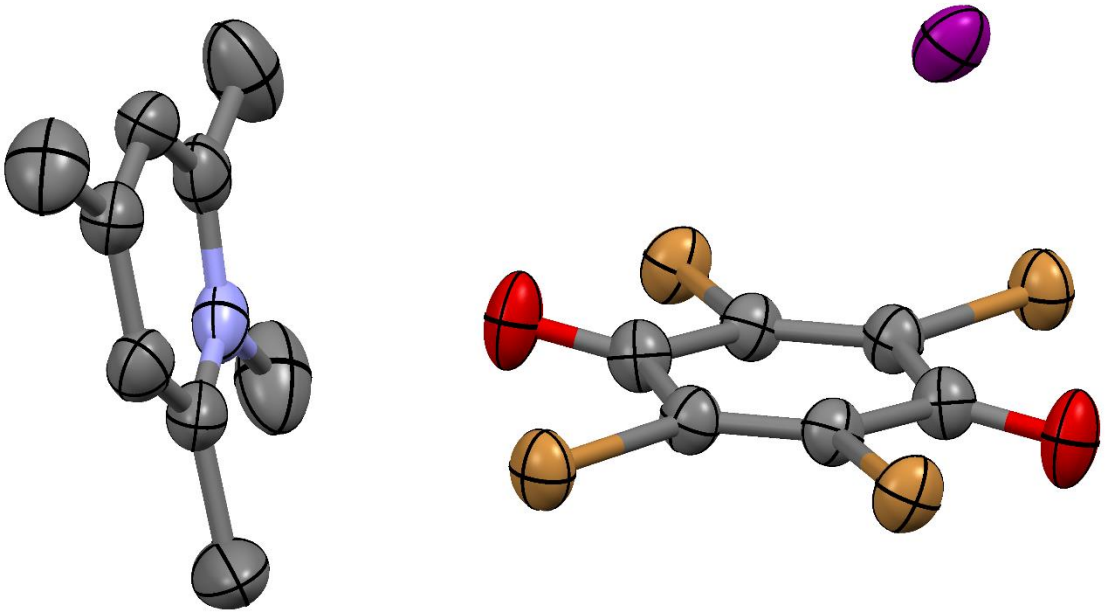

Figure 1-13. X-ray structural data showing anion-π interaction between p-bromanil (BA) and iodide (taken as a salt with N-methyl-4-methylcarboxypyridinium counter-ion). Structure shows the close separation between iodide and the carbons of BA.

III. Halides as electron donors

Iodide anions (I^-) have long been recognized as a good source of electrons for one-electron reductions. As early as 1912, a research study documented the effect of iodide on the benzoquinones p-chloranil (CA) and p-bromanil (BA), and while the research incorrectly assumes the reaction that occurs involves the replacement of ring halogens with iodine instead of an electron-transfer process, it nonetheless showed a knowledge that I^- salts were good reducing agents.[21]

All halides included in this study (fluoride, chloride, bromide, and iodide) have the capacity to perform electron-transfer reactions, even though in aprotic organic solvents I^- is known to have the greatest reduction efficiency.[9] The one-electron oxidation of halide anions (X^-) results in the reactive halide radical ($X^\bullet$). Therefore, oxidation potentials (E_{ox}) of halides, i.e. potentials of the $X^-/X^\bullet$ pairs, were established from computational studies.[22a] Redox potentials for other redox couples of halides, such

as X^-/X_2 and X^-/X_3^-, were established experimentally. The values of the redox potentials for these redox couples for all halides studied are shown in Table 1-2.[22]

	E_{ox} (V vs. SCE in acetonitrile)		
X	**$X^-/X^\bullet$**	**X^-/X_2**	**X^-/X_3^-**
F	3.06	-	-
Cl	2.03	0.79	0.79
Br	1.60	0.59	0.39
I	1.06	0.22	0.02

Table 1-2. Redox potentials vs. SCE in acetonitrile for the different halide couples (from reference 22).

Even with this well-established sequence of electron-donor strength and extensive usage of I^- as a reducing agent over other halides, some recent publications have shown that interactions of some π-acceptors with fluoride (F^-), but not I^-, resulted in the formation of radical anions.[9,23] In one such work, it was shown that F^- reduced N,N′-dipyridyl-1,4,5,8-naphthalenediimide (DPNDI) to either its radical anion or dianion depending on the equivalents of F^- added, similar to reactions between strong bases such as OH^- with DPNDI. The author of this work concluded that F^- was the strongest electron donor (Figure 1-16).[23] It is notable, however, that no evidence of anion-π complexation between DPNDI and F^- was found in their work.

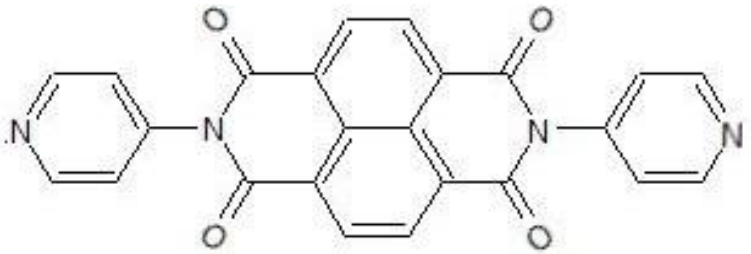

Figure 1-14. Structure of N,N′-dipyridyl-1,4,5,8-naphthalenediimide (DPNDI), which was shown to be reduced to its radical anion when F^- was added to solution.

Following studies pointed out that reduction of DPNDI by F^- is thermodynamically forbidden (DPNDI has a reduction potential E_{red} of about -0.49V vs. SCE in acetonitrile), suggesting that instead there were other redox pathways stemming from the strong basicity of fluoride.[24] These results raised questions about the nature of the shift from reversible anion-π complex formation to irreversible electron-transfer from X^- to π-acceptor, including what role anion-π interactions play in the electron-transfer processes.

p-benzoquinones are among the strongest organic π-acceptors known, and thus are a good choice for the study of anion-π bonding. Yet, their complexes in solutions were not yet characterized. Furthermore, a wide range of reduction potentials for the BQ π-acceptors and oxidation potentials for the X^- donors allows for a large variation in the free energy of electron transfer processes between these reactants. Consequently, a change from anion-π interactions (if they are observed at all) to electron-transfer reactions is expected. In this work, the nature of interactions between a variety of electron-deficient p-benzoquinones and halides was studied. The goals of this study are as follows:

1) Determine if anion-π complexes are formed between π-benzoquinones and halide anions;
2) Characterize quantitatively these complexes in solutions using UV-Vis spectral measurements and in the solid state using X-ray structural analysis;
3) Establish conditions of the transition between the complex formation and electron-transfer reactions;
4) Determine if π-bonded complexes are intermediates in redox processes in these systems.

CHAPTER 2: EXPERIMENTAL

I. Synthesis and purification of halide salts

All halide salts used were purchased from a supplier, except for Pr_4NF, which was synthesized as recorded in the following paragraph. Bu_4NF, Et_4NF, Bu_4NCl, Et_4NCl, Bu_4NI, Pr_4NI, and Et_4NI were obtained from Sigma Aldrich, while Pr_4NCl, Bu_4NBr, Pr_4NBr, and Et_4NBr were obtained from TCI.

i. Synthesis of tetrapropylammonium fluoride

Tetrapropylammonium fluoride ($(Pr_4N)F$) was synthesized following the procedure laid out in the reference 25, with some scaling and small modifications. $(Pr_4N)OH$ and HF starting materials were purchased from Sigma Aldrich. 25mL $(Pr_4N)OH$ (25 mmol) was added with stirring to a 100mL beaker along with 0.9mL HF (22 mmol) and 25mL deionized H_2O. Solution was at about pH 10, so added either $(Pr_4N)OH$ or HF in small increments to stabilize at pH 7, measuring with pH test strips. Solution was transferred to 100mL round bottom flask and rotovapped at 35°C for 10 hours. Next day, the flask was rotovapped at 40°C for 8 hours until only about 10mL of cloudy solution was left, then put in freezer. After 24 hours, rotovapped flask at 32°C until a lot of wet white crystals were observed. After an hour in the freezer, dry product was obtained and its composition was confirmed by NMR.

ii. Purification of halide salts

Purchased halide salts were purified via recrystallization. For chloride salts, approximately 2.25g were dissolved in 15mL warm ethanol with stirring. Solution was then cooled, using liquid nitrogen if necessary. If no crystals formed, hexane was added until precipitation commenced. Crystals were vacuum-filtered until dry.

Purification of purchased bromide salts was achieved by the dissolution of approximately 7.5g in 20mL of dichloromethane with heating. After salt was completely dissolved, a small volume of ethyl

acetate was added and solution was allowed to cool, both of which aided in precipitation of purified crystals. The product was vacuum filtered until dry.

Purification of purchased iodide salts was accomplished by dissolution of the salt in dichloromethane followed by the addition of a small amount of ethyl acetate. Solution was placed in freezer to initiate precipitation, and then the cold mixture was vacuum filtered until crystals were dry.

II. Purification of benzoquinones

All benzoquinones were purchased from Sigma Aldrich, except for bromanil, which was purchased from TCI.

i. Purification by sublimation

Purification was carried out when necessary by sublimation in vacuo using a sublimation apparatus. A small amount (around 1g) was taken and spread thinly at the bottom of the glass well, then the inside of the apparatus was subjected to a vacuum while heating in an oil bath. Depending on the benzoquinone, sublimation would start on the cold finger somewhere between 60 and 75°C. After at least an hour, the apparatus was disassembled and purified product was removed from the cold finger.

ii. Purification by recrystallization

Fluoranil was purified via recrystallization from acetone (approximately 2g in 10mL). Anything undissolved was filtered out of solution. Solution was then cooled, either in a freezer or rapidly using a dry ice bath, until yellow crystals formed. The cold mixture was then vacuum filtered until crystals were dry, and the filtrate was boiled down a little. Filtrate was then cooled again similarly until more yellow crystals appeared, which were subsequently vacuum filtered and dried.

III. Conventional UV-Vis spectroscopy

UV-Vis spectroscopy measurements were carried out using an Agilent Cary 5000 UV-Vis-NIR spectrophotometer using a 1mm, 2mm, or 1cm quartz cuvette at 20°C. Experiments were carried out

using acetonitrile for room temperature measurements and dichloromethane for cold temperature measurements. Measurements were made either in open air using standard cuvettes or under an inert argon atmosphere using a special vacuum cuvette.

i. Open-air experiments

Samples of BQ and X^- were weighed accurately to four decimal places using an analytical balance and transferred to a separate volumetric flask. Acetonitrile was added to each flask, and the contents of both flasks were mixed until completely dissolved. If measurements were made using a 1cm cuvette, the BQ and X^- solutions as well as pure acetonitrile could be added directly and precisely to the cell using appropriate glass syringes. They were then quickly mixed and the spectra were measured immediately after mixing. If measurements were made using a 1 mm cuvette, the solutions and any necessary acetonitrile were added using appropriate glass syringes to a 1mL volumetric flask first and quickly mixed before transferring the solution to the cell and running the spectral measurements immediately.

ii. Experiments under argon atmosphere

BQ and X^- were weighed accurately to four decimal places using an analytical balance before each was transferred to separate Schlenck tubes. Each tube was then sealed with a rubber stopper and connected to an argon/vacuum line, and was subjected to a vacuum for at least 30 seconds before being placed under argon. This process was repeated three times to ensure complete elimination of any oxygen. Solvent (acetonitrile or dichloromethane) was distilled under argon to remove the presence of both water and oxygen from the solvent, and appropriate amount of solvent was added to each tube. Next, the vacuum cuvette (Figure 2-1) was partially sealed with a plug valve, ensuring that no oxygen could get in while also allowing the cuvette to be placed under argon. After hooking it to an argon/vacuum line, cuvette was evacuated and placed under argon in the same manner as the samples. To ensure the spectrum was captured as soon as possible after mixing the analytes, the following process was used for each collected spectrum:

1) The correct volume of BQ solution was added precisely to the well of the cell using the appropriate glass syringe, taking care not to expose the solution to the atmosphere.
2) The cell was sealed, and the BQ solution was transferred from the well to the cuvette as quantitatively as possible.
3) The correct volume of solvent (if applicable) was added precisely to the well of the cell using the appropriate glass syringe, taking care not to expose the solvent to the atmosphere.
4) The cell was sealed, and the solvent was transferred from the well to the cuvette, acting as an additional "wash" to remove trace BQ still in the well.
5) The correct volume of X^- solution was added precisely to the well of the cell using the appropriate glass syringe, taking care not expose the solution to the atmosphere.
6) The cell was sealed completely and unhooked from the argon/vacuum line.
7) The cell was brought to the spectrophotometer and the contents were quickly mixed before running the spectrum immediately.

Figure 2-1. Cuvettes for UV-Vis measurements under argon atmosphere. Cell on the left is used for room temperature experiments, and cell on the right is used for low temperature experiments.

iii. Low temperature experiments

The spectrophotometer was outfitted with a special Dewar equipped with a quartz window (Figure 2-2) which allowed the cuvette to be kept at low temperature while the spectrum was collected. The Dewar was filled partially with either methanol or ethanol that had been cooled with liquid nitrogen. The process for conducting experiments under argon atmosphere listed in the previous section was used, with the following exceptions:

1) The cell was cooled down during the addition of solutions by being placed in a Dewar filled with either methanol or ethanol that had been cooled using liquid nitrogen.
2) The cells used for these measurements had no well, so all solutions or solvent were added directly into the cuvette at low temperature.

Figure 2-2. Dewar with quartz windows used for low temperature UV-Vis measurements. Dewar was filled with methanol or ethanol cooled with liquid nitrogen, then cuvette was inserted.

After being sealed and unhooked from the argon/vacuum line, the cold cuvette was mixed thoroughly and was quickly transferred into the special Dewar with quartz windows. The temperature of the Dewar was recorded, and then the spectrum was collected. Any additional spectra collected of the same mixture at a different temperature was achieved either by allowing the cuvette to warm in the air, heating the cuvette with a heat gun while under argon atmosphere, or by the heating or cooling of the cold solvent bath in the Dewar.

IV. Calculation of equilibrium constant (K_{eq}) and extinction coefficient (ε)

For calculations of equilibrium constant and extinction coefficient (molar absorptivity) data of the [BQ, X^-] complex, room temperature experiments were designed to keep benzoquinone concentration constant while varying the concentration of halide. Stock BQ concentrations were usually no larger than 10mM, while stock X^- concentrations were considerably higher, usually at least 100 times the BQ concentration. In each of these experiments, first a baseline and background spectrum of the solvent was acquired, followed by the spectrum of each separate analyte. Then, keeping the total volume and benzoquinone concentration constant, between 10 and 12 spectra are taken starting with a 1:1 volumetric ratio of BQ to X^- and ranging down to a 1:0.001 volumetric ratio.

During data analysis, first all spectra obtained have their baseline corrected by selecting a wavelength on all spectra where no absorption is taken place and setting it to zero (somewhere between 650 and 800 nm). For subtraction of the separate analyte spectrum, all halides used were either tetrapropylammonium or tetrabutylammonium salts that did not absorb above 300nm, so subtraction is unnecessary. The separate benzoquinone spectrum is subtracted from the spectra of every mixture, yielding the spectrum of anion-π complex. From these corrected spectra, the wavelength of peak absorbance for the complex formation in Equation 2-1 can be determined:

$$BQ + X^- \underset{}{\overset{K_{eff}}{\rightleftharpoons}} [BQ, X^-] \qquad \text{(Equation 2-1)}$$

A Benesi-Hildebrand graph can be used to ascertain the interaction's equilibrium constant and extinction coefficient by combining Beer's Law (Equation 2-2) and the equilibrium constant equation (Equation 2-3) into a new formula that resembles the linear equation (Equation 2-4).

$$A = \varepsilon l[BQ, X^-] \quad \text{(Equation 2-2)}$$

where A is absorbance, ε is the extinction coefficient ($M^{-1}cm^{-1}$), l is the cuvette length (cm), and [BQ, X^-] is the complex concentration (M).

$$[BQ, X^-] = K_{eq}\,[BQ]\,[X^-] \quad \text{(Equation 2-3)}$$

where K_{eq} is the equilibrium constant (M^{-1}), and [BQ] and [X^-] are the benzoquinone and halide concentrations respectively (M).

$$\frac{BQ}{Abs.} = \frac{1}{\varepsilon l(K_{eq})[X^-]} + \frac{1}{\varepsilon l} \quad \text{(Equation 2-4)}$$

By plotting $\frac{1}{[X^-]}$ as x vs. $\frac{[BQ]}{Abs.}$ as y, the y-intercept $\left(\frac{1}{\varepsilon l}\right)$ from the best fit line can be used to determine the extinction coefficient. Using that information plus the line slope $(\varepsilon l K_{eq})$, the equilibrium constant can be found. This treatment of the data assumes a 1:1 complex is formed, which was found to be the correct stoichiometry in every BQ/X^- interaction treated with a Job's plot.

Another more precise method for determining K_{eq} and ε was applying regression analysis using Origin software to fit a non-linear curve equation (Equation 2-5) to data obtained when the X^- concentration (M) was plotted against the anion-π complex absorbance at peak wavelength (λ_{max}). Origin software also has the added benefit of calculating the standard error of measurements to determine how well the curve fits the data.

$$y = \varepsilon l\left(\frac{A+x+\frac{1}{K_{eq}}}{2} - \frac{\sqrt{\left(A+x+\frac{1}{K_{eq}}\right)^2 - 4Ax}}{2}\right) \quad \text{(Equation 2-5)}$$

where y is the complex absorbance after baseline correction and subtraction of the BQ spectrum, A is the BQ concentration (M), and x is the X^- concentration (M). This equation assumes a 1:1 complex stoichiometry.

V. Stopped-flow experiments

Stopped-flow experiments were carried out using a TgK KinetAsyst Stopped-Flow System equipped with the TgK Cryo System. Solvent and analyte solutions were prepared as previously stated in the "Experiments under argon atmosphere" section. Two sample holder lines and additionally the system line were flushed with at least 1mL of solvent, followed by taking a baseline and background spectrum to ensure the system was clear of contaminants. BQ and X^- solutions were each loaded into a 5 mL glass syringe, and each syringe was immediately hooked into a sample holder line. Any room temperature measurements were taken. Liquid nitrogen was hooked into the cryo system and the temperature of the cell was lowered to at least -80°C before low temperature measurements were made.

VI. Electrochemical measurements

All electrochemistry experiments were carried out using a BASi EC Epsilon potentiostat equipped with a C-3 Cell Stand. Experiments were carried out in either a H-type 2-chambered electrochemical cell or using a 3-neck round bottom flask fitted with a Por. E fritted tube to create a 2-chambered cell for argon atmosphere experiments. All measurements used a platinum counter electrode and a silver reference electrode. Cyclic voltammetry (CV) scans used a 3mm glassy carbon working electrode, and bulk electrolysis used a platinum plate working electrode. Electrolyte solution was 0.1M tetrabutylammonium hexafluorophosphate (Bu_4NPF_6) in acetonitrile solvent, and all cyclic voltammetry experiments started with a three-point background scan of the electrolyte solution (0V – 0.7V – 0V).

i. Open air experiments

$(Bu_4N)PF_6$ was weighed accurately to 4 decimal places using an analytical balance and added quantitatively into the large chamber of the H-type cell. Electrolyte was dissolved in 10mL acetonitrile and 4mL of solution was quickly transferred to the small chamber of the cell, making the solution height in both chambers equal. Reference and working electrodes were placed in the large chamber, and the counter electrode was placed in the small chamber, and background CV measurement was collected. BQ was weighed out similarly and added quantitatively directly into the large chamber with stirring until completely dissolved, and all analyte measurements were made. For electrolysis, the solution was stirred during collection, and samples were taken at intervals for UV-Vis measurements. After electrolysis, a small mass of ferrocene was added to solution and a final CV was collected to reference all voltammetry scans vs. ferrocene, a compound with well-studied and stable electrochemical properties.

ii. Experiments under argon atmosphere

$(Bu_4N)PF_6$ was weighed out similarly as before and transferred to a 3-neck round bottom flask. The flask was outfitted with a fritted tube as a second chamber, a vacuum/gas adaptor with stopcock, and a stirbar. Then the openings were sealed with rubber stoppers and an argon/vacuum line was hooked to the flask (Figure 2-3). It was placed under argon as outlined in the UV-Vis section, then 10 mL distilled acetonitrile was added to the center to dissolve the electrolyte. Quickly, 1 mL of electrolyte solution was transferred to the fritted tube, making the level of solution equal in both chambers. The tube was sealed, the stopcock was closed, and the argon/vacuum line was disconnected so that the tube could be transferred and hooked up to the potentiostat for CV background measurement. The tube was reattached to the argon vacuum line and placed under argon. BQ was weighed out similarly to $(Bu_4N)PF_6$ and added directly to the main chamber with stirring until completely dissolved. The tube was then sealed and unhooked from the argon/vacuum line to be transferred and hooked up to the potentiostat for CV measurements and electrolysis. For UV-Vis

measurements during electrolysis, a sample was taken with a glass syringe through the rubber septum to preserve the inert atmosphere inside. After electrolysis, the tube was hooked back up to the argon/vacuum line and placed under argon, and a small mass of ferrocene was added with stirring until dissolved. The tube was sealed and unhooked from the argon/vacuum line to be transferred and hooked up to the potentiostat for a final CV measurement with ferrocene to reference all voltammetry scans vs. ferrocene.

Figure 2-3. Electrochemical cell setup for CV measurements and electrolysis under argon. Middle neck is fitted with a rubber stopper that allows the working and reference electrodes to pass through its septum into the main chamber, and side neck is fitted with a fritted tube sealed with a rubber stopper that allows the counter electrode to pass through its septum.

VII. Crystallization procedures

All crystals for the X-ray structural measurements were obtained either by hexane diffusion into a dichloromethane solution containing BQ and X^- salt at low temperature or by slow evaporation of similar solutions at room temperature.

i. Diffusion crystallizations

The appropriate BQ and X^- amounts were weighed out accurately, and each was added quantitatively to its own Schlenck tube. The tubes were sealed with a rubber stopper and partially with a plug valve, and each was then hooked up to its own argon/vacuum line. Each tube was placed under argon as outlined in the UV-Vis section. Dichloromethane was distilled under argon to eliminate any oxygen or water, and then a minimum volume was added to each tube to dissolve each analyte. The BQ tube was then cooled to between -60 and -70°C using a dry-ice/acetone bath, making sure the BQ stays in solution by adding dichloromethane if needed. Using a glass syringe, the X^- solution was added slowly down the side of the tube into the cold BQ solution, making sure to mix the BQ/X^- solution thoroughly. A small layer of 3:1 dichloromethane/hexane was slowly added down the walls of the tube on top of the solution, followed by a small layer of 1:1 dichloromethane/hexane and a small layer of 1:3 dichloromethane/hexane slowly on top. A large layer of hexane was added slowly up to the neck of the tube, and then the tube was sealed and detached from the argon/vacuum line. The tube was quickly placed in a cold ethanol bath at 75°C to allow for slow diffusion of hexane into the solution over the course of several days to a few weeks.

ii. Slow evaporation crystallizations

For slow evaporation crystallizations, the appropriate BQ and either X^- or neutral donor was weighed out similarly as before each into its own flask. The appropriate amount of solvent was added to create the stock solution for each analyte (some experiments used acetonitrile, some used acetone). Small 10 mL vials were used as crystallization tubes. Volumes of BQ and the X^-/neutral donor were

added to a vial to obtain a 1:1 molar ratio of analytes for each crystallization. For crystallizations in acetone, 500 uL of hexane was added to make sure evaporation did not happen too quickly. Each vial was sealed with a plastic cap, and several holes were poked through the lid to allow for evaporation over several days.

VIII. X-ray crystallography structural analysis

X-ray structural measurements were done at Purdue University in their x-ray diffraction laboratory by Dr. Matthias Zeller using a Bruker AXS D8 Quest CMOS diffractometer. Intensity data for X-ray crystallographic analysis were collected at 173 K with a Bruker SMART Apex or Bruker AXS D8 Quest CMOS diffractometer using Mo Kα radiation (λ= 0.71073 Å). The structures were solved by direct methods and refined by full matrix least-squares treatment. Intermolecular contacts were analysed using the OLEX2 structure solution, refinement and analysis program. Crystallographic, data collection, and structure refinement details are presented in Table 2-1. Complete crystallographic data, in CIF format, have been deposited with the Cambridge Crystallographic Data Centre. CCDC 1901034 - 1901038 contain the supplementary crystallographic data for this paper. These data can be obtained free of charge via www.ccdc.cam.ac.uk/data_request/cif.

	$(Pr_4N)I \cdot FA$	$(Pr_4N)Br \cdot FA$	$2((Pr_4N)Br) \cdot FA$	$2((Pr_4N)Cl) \cdot DDQ$	$(Pr_4N)_2 \cdot (DDQ)_3$
Chemical formula	$C_6F_4O_2 \cdot C_{12}H_{28}N \cdot I$	$C_6F_4O_2 \cdot C_{12}H_{28}N \cdot Br \cdot (C_2H_2O_4)_{0.5}$	$C_6F_4O_2 \cdot (C_{12}H_{28}N \cdot Br)_2 \cdot (CH_2Cl_2)_2$	$(C_8Cl_2N_2O_2)_2 \cdot C_{12}H_{28}N \cdot Cl$	$(C_8Cl_2N_2O_2)_3 \cdot (C_{12}H_{28}N)_2$
M_r	493.31	491.34	882.44	675.80	1053.70
Crystal system	Triclinic	Triclinic	Triclinic	Monoclinic	Monoclinic
Space group	$P\bar{1}$	$P\bar{1}$	$P\bar{1}$	$P2_1/n$	$P2_1/c$
a(Å)	9.4008 (14)	9.4100 (4)	8.6884 (8)	15.2745 (13)	10.2282 (6)
b(Å)	10.9112 (16)	9.4831 (4)	9.4552 (8)	10.2019 (9)	12.5758 (7)
c(Å)	11.8382 (18)	12.9042 (5)	14.6981 (12)	20.6506 (18)	19.9561 (9)
α(°)	105.366 (5)	97.931 (2)	92.465 (3)	90	90
β (°)	97.509 (6)	90.411 (2)	104.135 (3)	96.098 (6)	97.358 (2)
δ (°)	110.255 (5)	97.764 (2)	112.842 (3)	90	90
V (Å^3)	1064.8 (3)	1129.66 (8)	1066.17 (16)	3199.8 (5)	2545.8 (2)
Z	2	2	1	4	2
Radiation type	Mo $K\alpha$	Cu $K\alpha$	Mo $K\alpha$	Mo $K\alpha$	Mo $K\alpha$
μ(mm^{-1})	1.55	2.99	2.20	0.50	0.39
Crystal size (mm)	0.23 × 0.13 × 0.03	0.22 × 0.06 × 0.04	0.20 × 0.19 × 0.05	0.22 × 0.1 × 0.06	0.32 × 0.07 × 0.06
Abs. corr.	Multi-scan[a]	Multi-scan[a]	Multi-scan[a]	Multi-scan[a]	Multi-scan[a]
T_{min}, T_{max}	0.218, 0.269	0.490, 0.754	0.406, 0.563	0.624, 0.746	0.643, 0.746
# Meas. refl.	18865	16556	12876	38981	24704
# Ind. refl.	5800	14692	4883	9320	5717
# Obs. refl. [$I > 2\sigma(I)$]	4598	3912	2907	4835	3995
R_{int}	0.066	0.105	0.065	0.098	0.065
R [$F^2>2\sigma(F^2)$]	0.036	0.053	0.058	0.071	0.044
wR(F^2)	0.075	0.151	0.153	0.167	0.103
S	1.06	1.11	1.00	1.01	1.02

Table 2-1. Crystallographic, data collection, and structure refinement details of x-ray measurements. Measurements made using a Bruker AXS D8 Quest CMOS diffractometer. [a]*SADABS* 2016/2: Krause, L.; Herbst-Irmer, R.; Sheldrick G.M.; Stalke D. *J. Appl. Cryst.* **2015.** *48*. 3-10.

CHAPTER 3: RESULTS

I. UV-Vis spectral and X-ray structural study of interaction of halide anions with DDQ acceptor

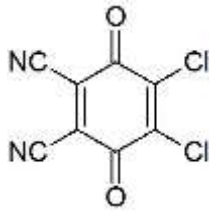

Figure 3-1. Structure of 2,3-dichloro-5,6-dicyanobenzoquinone (DDQ)

2,3-Dichloro-5,6-dicyanobenzoquinone (DDQ) is a well-known strong one-electron oxidizing agent that undergoes reduction to its radical anion ($DDQ^{\bullet-}$) at 0.52V vs. SCE in acetonitrile.[13] The UV-Vis spectrum of neutral DDQ is characterized by a Gaussian (bell-shaped) absorption band with a peak absorbance (λ_{max}) at 360 nm. Chloride (Cl^-) anions in the form of a Bu_4N^+ or Pr_4N^+ salt did not show an absorption above 300 nm. Upon their addition to a solution of DDQ, however, a new band appeared in the UV-Vis spectrum without the disappearance of the DDQ peak (Figure 3-2A). After the DDQ spectrum is subtracted out, this new band appears as a broad Gaussian peak with λ_{max} at 437 nm (Figure 3-2B).

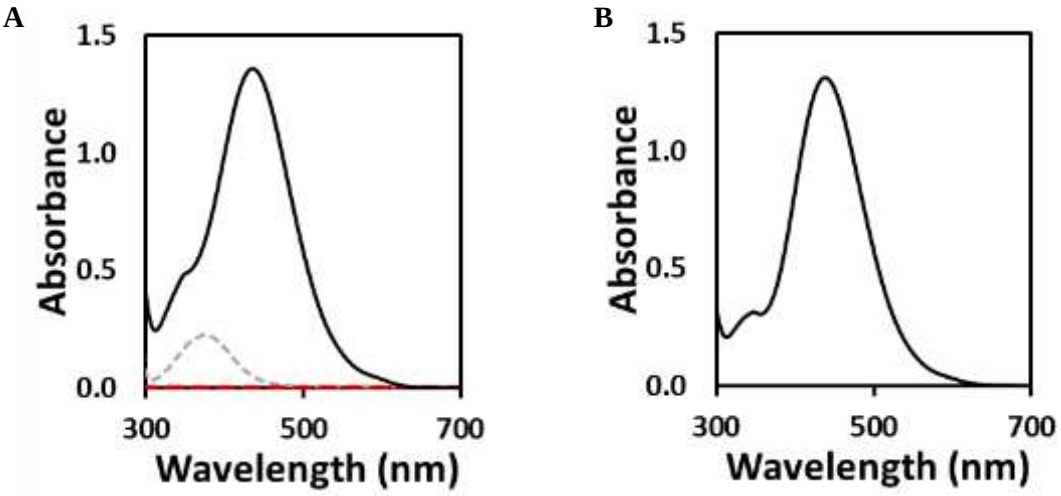

Figure 3-2. A) Absorption spectrum of a solution of 2.64mM DDQ with 125mM $(Pr_4N)Cl$ in acetonitrile. Dashed grey line is the separate DDQ spectrum, and dashed red line is the separate $(Pr_4N)Cl$ spectrum. **B)** Spectrum obtained by subtraction of the separate DDQ spectrum from the mixture spectrum.

When the DDQ concentration was held constant and the Cl^- concentration was varied, changes in the intensity of the new band were observed (Figure 3-3).

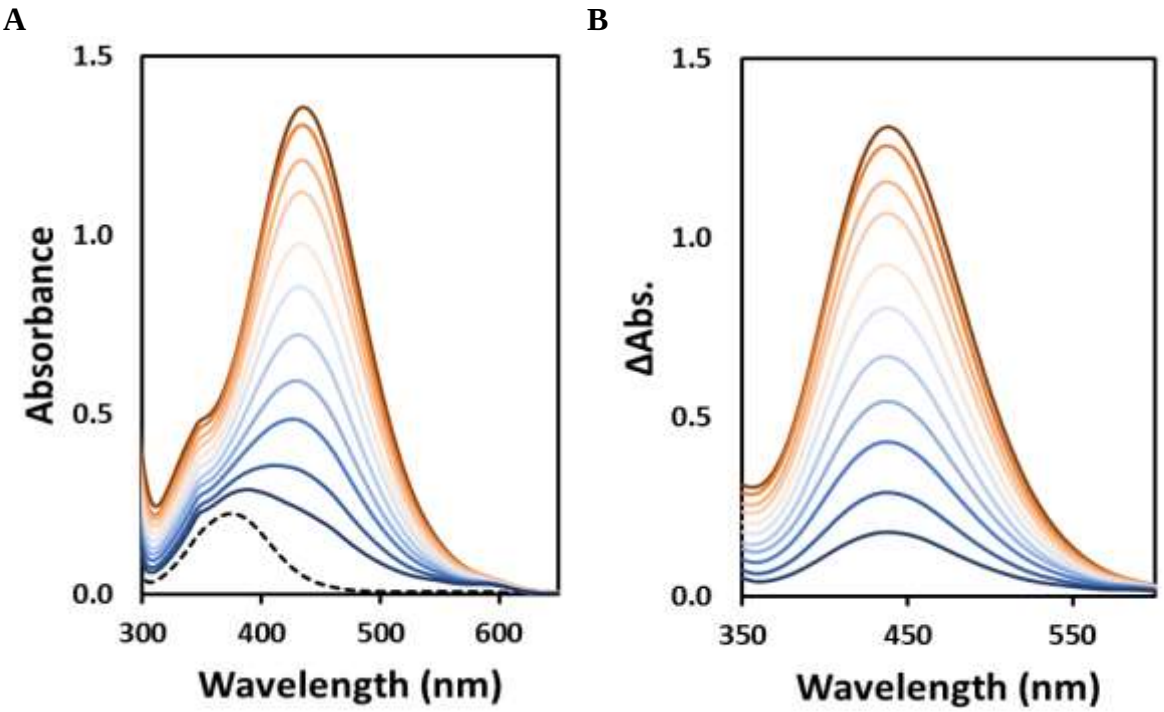

Figure 3-3. Spectral changes in DDQ/Cl^- solution upon increasing Cl^- concentration at constant DDQ concentration **A)** Spectral changes resulting from the addition of $(Pr_4N)Cl$ to 2.64mM solution of DDQ in acetonitrile. Dashed line shows the spectrum of DDQ itself. Concentration of $(Pr_4N)Cl$ added (in mM, solid lines, from bottom to top): 2.5, 3.8, 6.3, 8.8, 12.5, 17.5, 22.5, 32.6, 45.1, 62.6, 125.2. **B)** Spectra obtained by subtraction of the individual DDQ spectrum from the mixture spectra.

The intensity of this band not only increased with the rise in Cl^- concentration, but also with the lowering of the solution temperature at constant reagent concentrations (Figure 3-4). In this temperature-dependence experiment, the solution was first cooled to -80°C. As the solution was warmed, the absorption strength of the band at 437 nm diminished, showing that the interaction is reversible in nature. This reversibility and the stronger interaction at lower temperatures coupled with spectral changes upon increasing Cl^- concentration points to the formation of a DDQ/Cl^- anion-π complex ([DDQ, Cl^-]).

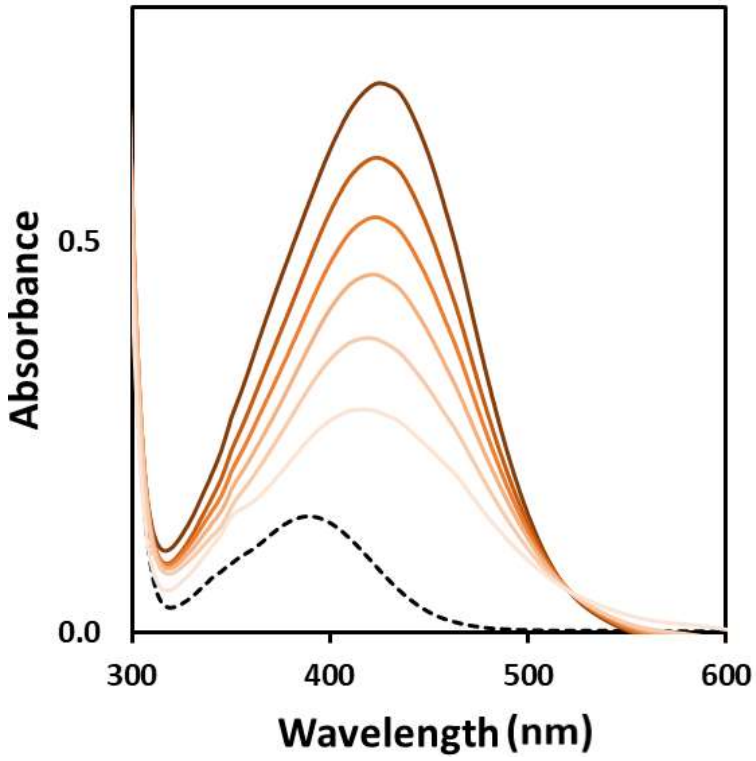

Figure 3-4. Temperature dependence of solution with constant concentration of 2mM DDQ and 2mM (Bu_4N)Cl solution in dichloromethane. Dotted line shows the spectrum of DDQ itself. Temperatures (solid lines, from bottom to top in °C): 18, -10, -30, -48, -62, -80.

To verify this new band represented the formation of an anion-π complex between DDQ and Cl^- and not the spectrum of the DDQ radical anion ($DDQ^{\bullet-}$) caused by the one-electron reduction of DDQ by Cl^-, the DDQ radical anion spectrum was obtained. Bulk electrolysis was performed on a solution of neutral DDQ to reduce it to $DDQ^{\bullet-}$, and samples were taken for UV-Vis analysis at regular intervals during electrolysis. The color of the solution changed substantially, from the yellow hue of the neutral DDQ solution at the beginning to a deep maroon at the end of electrolysis. The resulting spectra (Figure 3-5) were very different from the spectra obtained from the interaction of DDQ with Cl^-.

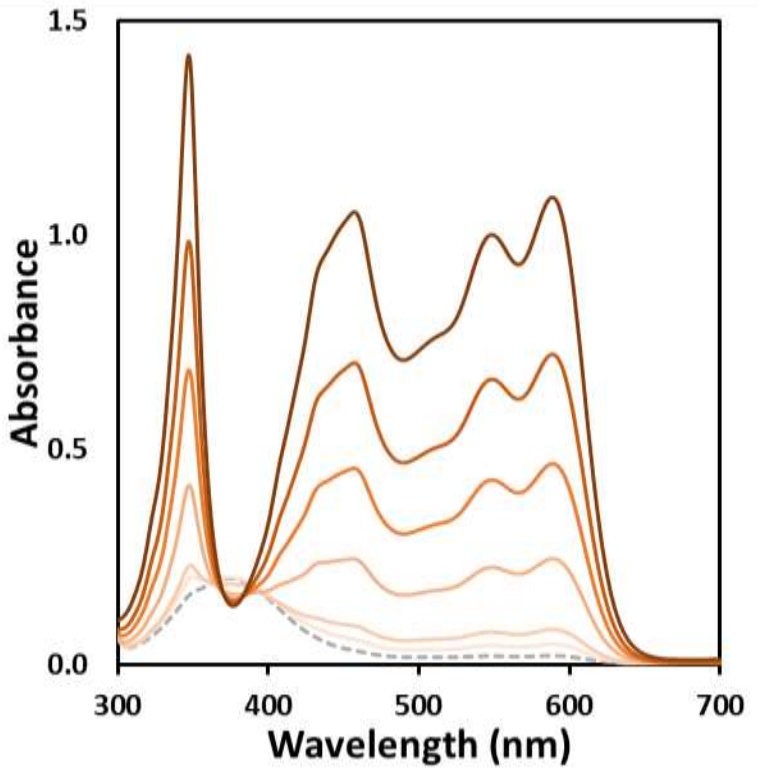

Figure 3-5. Spectra obtained by the bulk electrolysis at -0.1V of 2.49mM DDQ with 0.1M $(Bu_4N)PF_6$ as supporting electrolyte in acetonitrile. Dotted line shows the spectrum of DDQ itself. From bottom to top, solid lines show the progress of electrolysis.

Comparison of the spectral changes in Figure 3-3 to those in Figure 3-5 ruled out the possibility of a one-electron reduction of DDQ to $DDQ^{\bullet-}$ by Cl^- and suggested that instead an anion-π complex between DDQ and Cl^- is formed. To determine the stoichiometry of [DDQ, Cl^-], a Job plot experiment was performed, where the concentrations of DDQ and Cl^- were varied while keeping the sum of these concentrations constant, and the intensities of the resulting new band absorption were plotted against the corresponding fraction of Cl^- used. This plot exhibited a maximum absorbance for the complex at a 1:1 molar ratio (Figure 3-6), which means the chemical equation for complex formation can be written as follows:

$$DDQ + Cl^- \rightleftharpoons [DDQ, Cl^-] \qquad \text{(Equation 3-1)}$$

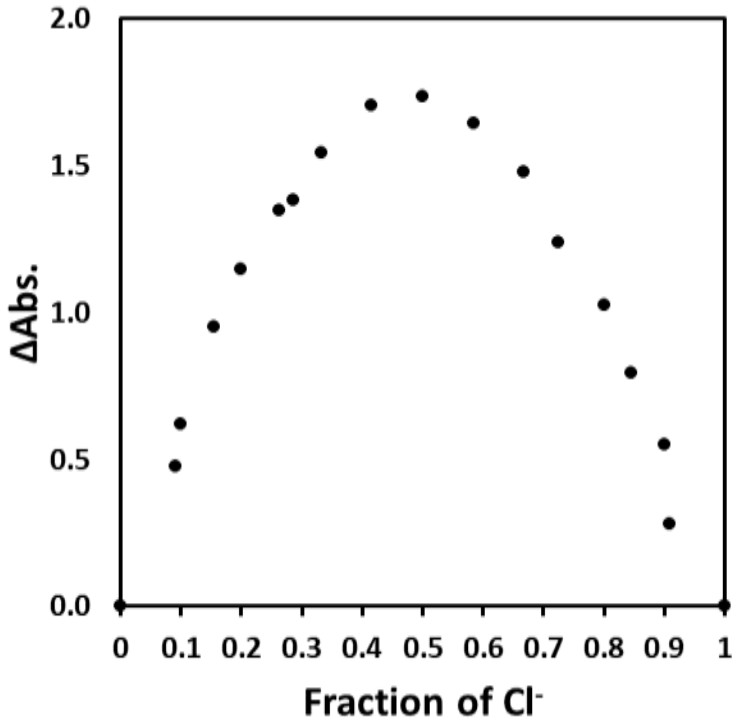

Figure 3-6. Dependence of the complex absorption on the molar fraction of chloride present in a solution of DDQ with $(Pr_4N)Cl$ in acetonitrile (Job plot). The sum of the concentration of components was held constant (20mM).

With the knowledge that a 1:1 complex is formed for [DDQ, Cl^-], quantitative treatment of the absorption data in Figure 3-3B was used to calculate the equilibrium constant (also called formation constant, K_{eq}) and extinction coefficient (also called molar absorptivity, ε). A Benesi-Hildebrand plot (Figure 3-7A) and non-linear regression analysis fitted by Origin (Figure 3-7B) were both used to compute these thermodynamic values. Since Benesi-Hildebrand computations apply certain approximations and the non-linear regression analysis does not, Origin treatment gives more accurate data and thus was preferred for reporting calculated thermodynamic data. Regression analysis treatment for the DDQ/Cl^- solution resulted in the evaluation of K_{eq} = 77 M^{-1} and ε = 5400 $M^{-1}cm^{-1}$ for [DDQ, Cl^-].

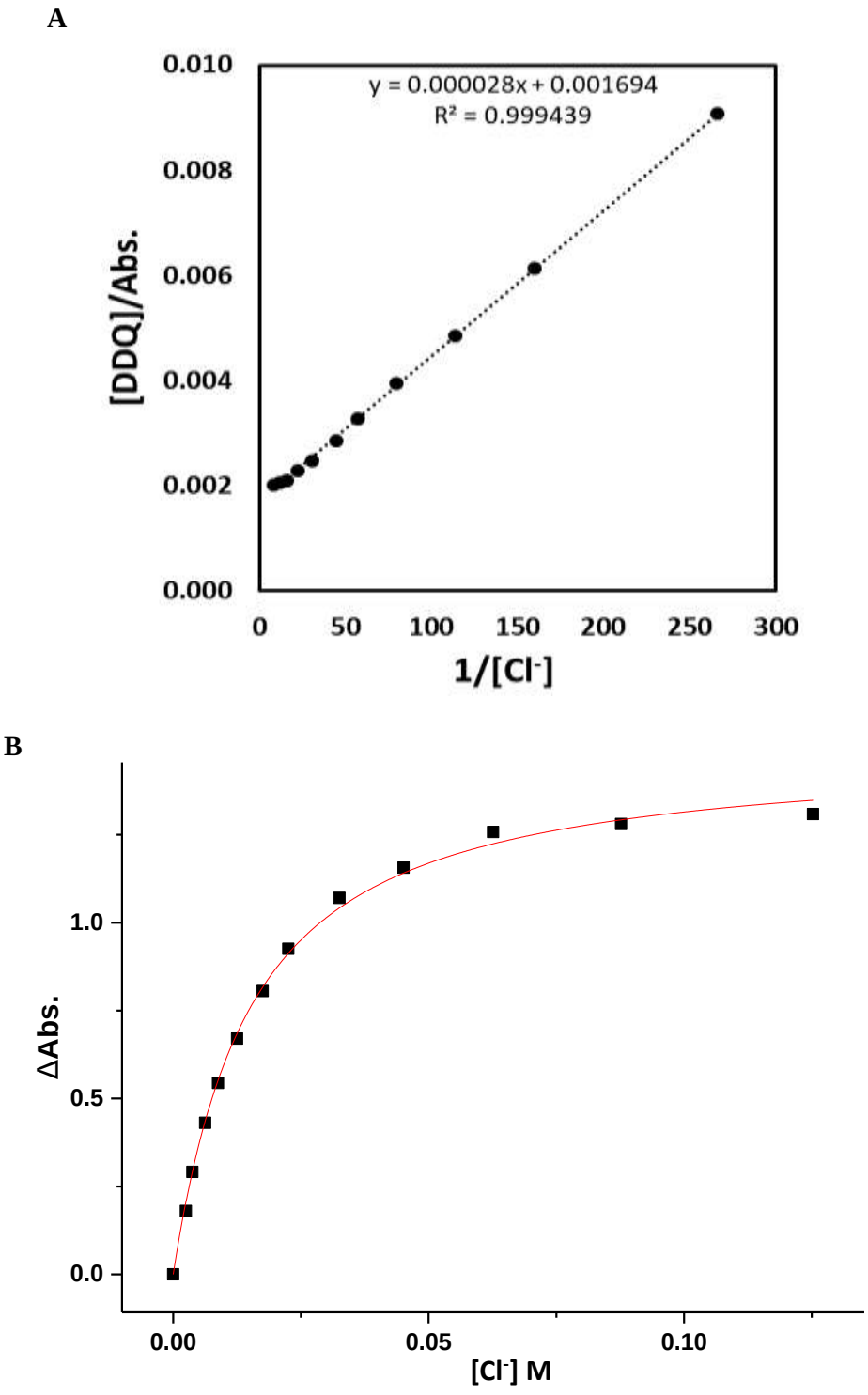

Figure 3-7. Treatment of the DDQ/Cl^- spectral data from Figure 3-2B. **A)** Benesi-Hildebrand treatment of absorption data. **B)** Fitting of non-linear curve to absorption data using regression analysis through Origin.

The UV-Vis data from acetonitrile solutions of DDQ/(Pr_4N)Cl experiment indicated the existence of [DDQ, Cl^-] and quantified the strength of the interaction in solution. When dichloromethane was used as a solvent for UV-Vis analysis of DDQ/Cl^- solutions, an analogous band to that observed in Figure 3-2 appeared. This indicated formation of a similar complex to that seen in acetonitrile solutions, and since dichloromethane has a much lower melting point than acetonitrile, it was used as solvent for low temperature crystallizations. The structure of this complex was obtained from solid-state X-ray measurements of [DDQ, Cl^-] crystals, prepared as outlined in Chapter 2. It revealed that they were comprised of DDQ and Cl^- in a 2:1 ratio, with the anions nested between the moieties of two π-acceptors (Figure 3-8).

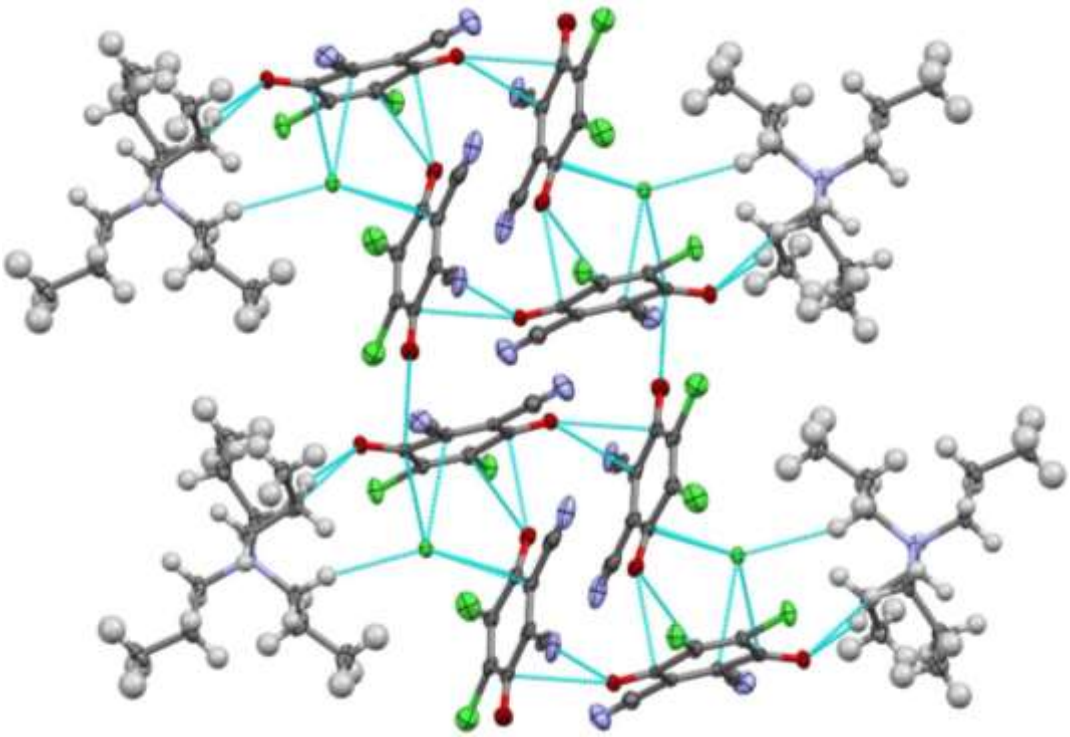

Figure 3-8. Crystal structure fragment showing anion-π complex between DDQ and Cl^- with Pr_4N^+ cations helping stabilize the interaction. Blue lines indicate non-covalent contacts shorter than the sums of the van der Waals radii.

Instead of being situated over the ring centroid, Cl^- anions were located almost directly over the carbonyl group carbons of DDQ in the crystals. Separation between Cl^- and the carbonyl carbons of 2.816 – 3.039 Å were much shorter (12-18%) than the sum of the van der Waals radii of Cl^- and carbon. Along with the close proximity of Cl^- to DDQ, indicating a strong interaction, there was also substantial deviation (~0.31 Å) of the oxygen atoms of these carbonyl groups out of the plane of the ring, which could indicate that the anion-π bond is strong enough to begin changing the hybridization of the interacting carbon from sp^2 to sp^3 (Figure 3-9).

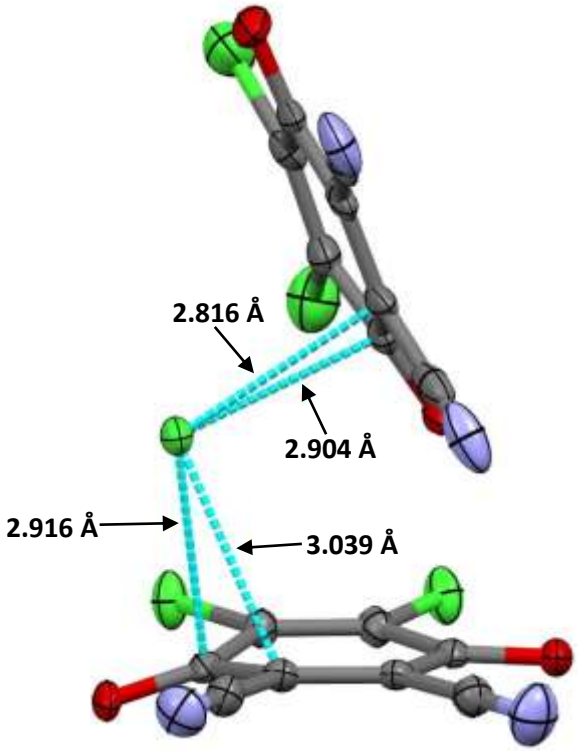

Figure 3-9. Fragment of DDQ/(Pr_4N)Cl crystal structure showing donor/acceptor contacts. Blue lines indicate contacts between Cl^- and carbons on DDQ molecule that are shorter than the sum of their van der Waals radii.

After the nature of [DDQ, Cl^-] was established, DDQ's interaction with iodide (I^-) was also explored. I^- is a much more powerful electron donor, and its complexation with the strong oxidant DDQ had the potential to create a stronger anion-π complex. Instead, I^- immediately reduced DDQ to $DDQ^{\bullet-}$. When an iodide salt was introduced to a DDQ solution, the instantaneous change of the solution's color to the deep maroon associated with $DDQ^{\bullet-}$ occurred. The resulting UV-Vis spectrum of the solution resembled the $DDQ^{\bullet-}$ spectrum from Figure 3-4, with the addition of a side-peak around 365nm. It is known that oxidation of I^- results (when iodide is in a large excess) in the formation of triiodide (I_3^-), and the I_3^- spectrum has a strong absorption around 360 nm.[22] When the spectra of $DDQ^{\bullet-}$ and I_3^- were combined, the result was the spectrum observed for the DDQ/I^- interaction (Figure 3-10). This indicated that the following interaction took place in solution:

$$2DDQ + 3I^- \longrightarrow 2DDQ^{\bullet-} + I_3^- \qquad \text{(Equation 3-2)}$$

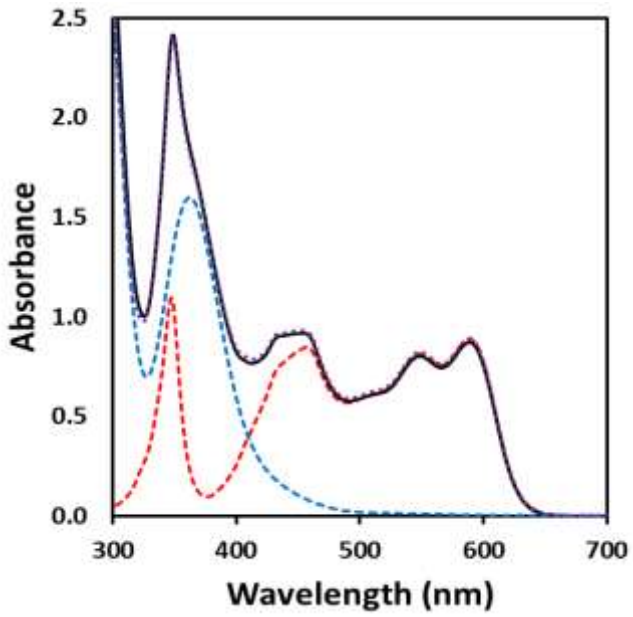

Figure 3-10. Spectrum formed immediately upon mixing of 2.5mM DDQ and 2.5mM (Pr_4N)I in acetonitrile (solid black line). Dashed red line represents the $DDQ^{\bullet-}$ spectrum, and dashed blue line is the separate I_3^- spectrum. When the $DDQ^{\bullet-}$ and I_3^- spectra are summed, they create the dotted purple spectrum, which is the same as the spectrum of the DDQ/I^- solution.

The unit cell parameters of the crystals precipitated from DDQ/(Pr_4N)I solutions in dichloromethane at low temperature were identical to that of the (Pr_4N)DDQ salt reported earlier (Figure 3-11).[26] The UV-Vis spectra of their solution were consistent with the data reported here for the $DDQ^{\bullet-}$ radical.

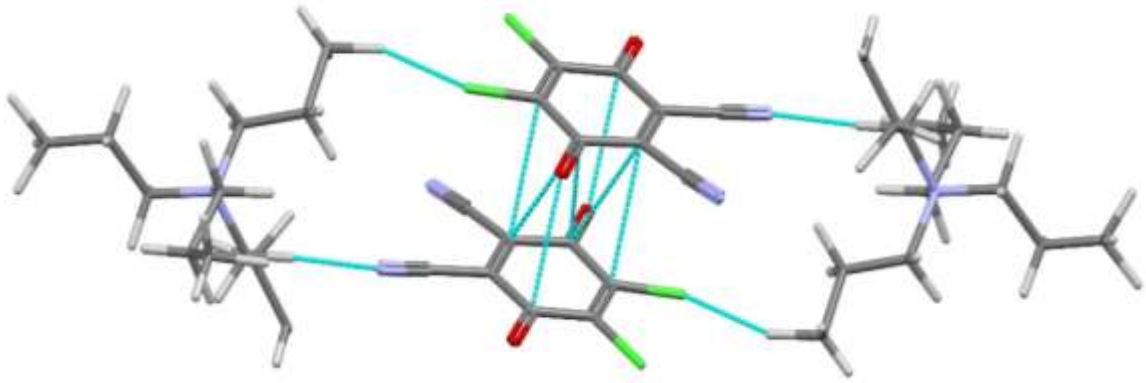

Figure 3-11. Fragment of the X-ray structure of crystals precipitated from a DDQ/(Pr_4N)I solution showing π-π stacking of $DDQ^{\bullet-}$ to create the DDQ_2^{-} dimer, with Pr_4N^+ cations helping stabilize the interaction (from reference 26). Blue lines indicate non-covalent contacts shorter than the sums of the van der Waals radii.

With the formation of an anion-π complex observed with DDQ and Cl^-, and a redox reaction occurring between DDQ and I^-, the outcome of the interaction of DDQ with bromide (Br^-) came into question. Due to its midpoint of electron acceptor strength between Cl^- and I^-, either result was possible. When Br^- anions were added in the form of a Bu_4N^+ or Pr_4N^+ salt to a DDQ solution in acetonitrile, the resulting spectrum resembled that of the radical anion ($DDQ^{\bullet-}$) (Figure 3-12A). When compared to the reaction with the same concentration of I^- anions and DDQ, however, the electron transfer reaction was slower and yielded less radical anion (Figure 3-12B).

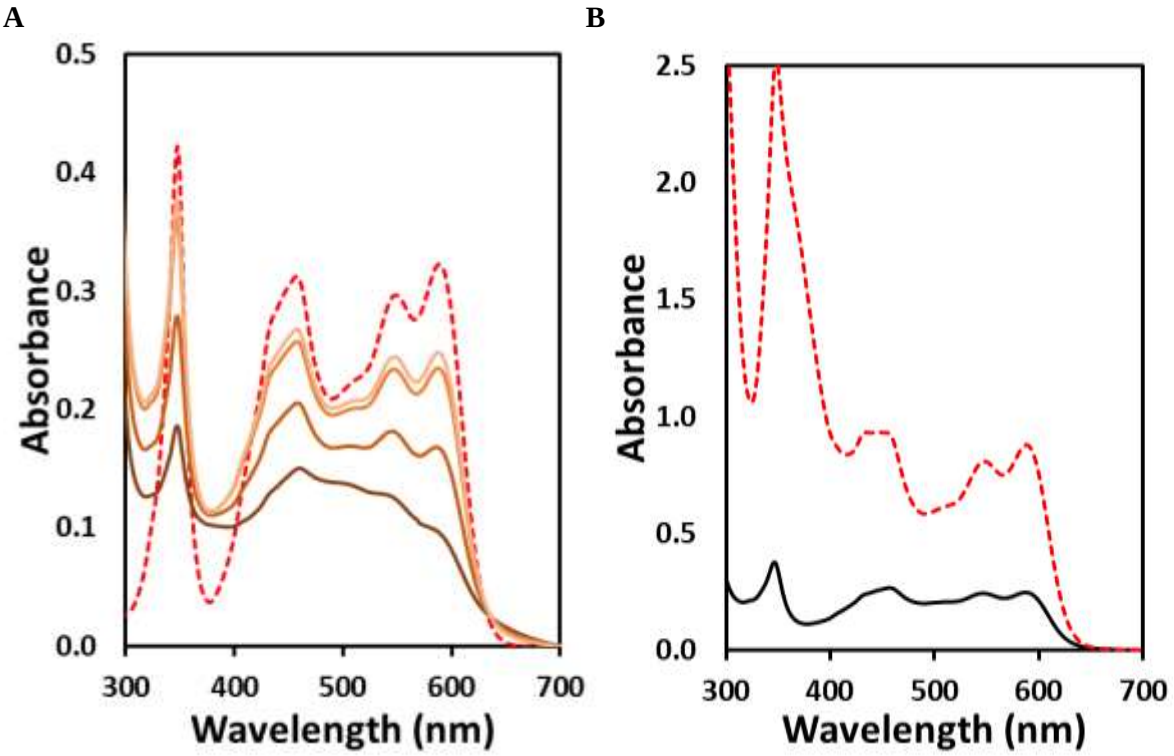

Figure 3-12. Spectral changes in DDQ/Br^- solution showing formation of radical anion. **A)** Solid lines show time-dependence of the reaction of 2.5mM DDQ with 2.5mM (Pr_4N)Br in acetonitrile. From bottom to top: Immediate, after 1 min, after 5 min, and after 15 min. Dashed red line shows the $DDQ^{\bullet-}$ spectrum. **B)** Comparison of the reactions of 2.5mM DDQ with 2.5mM Br^- (solid line) and with 2.5mM I^- (dashed line).

Since the initial UV-Vis spectrum of the DDQ/Br^- solution was somewhat different from the $DDQ^{\bullet-}$ spectrum, stopped-flow spectra of this solution were obtained to observe the spectrum immediately upon mixing. These measurements showed that at first a broad absorption band with a λ_{max} at 490 nm appeared. During a few seconds, this band disappeared and the spectrum of the DDQ radical anion was formed (Figure 3-13A). When dichloromethane was used as a solvent instead of acetonitrile and temperature was decreased to -90°C, the formation of the $DDQ^{\bullet-}$ was much slower, and the broad band that appeared upon mixing of DDQ with Br^- was persistent for a few hours (Figure 3-13B).

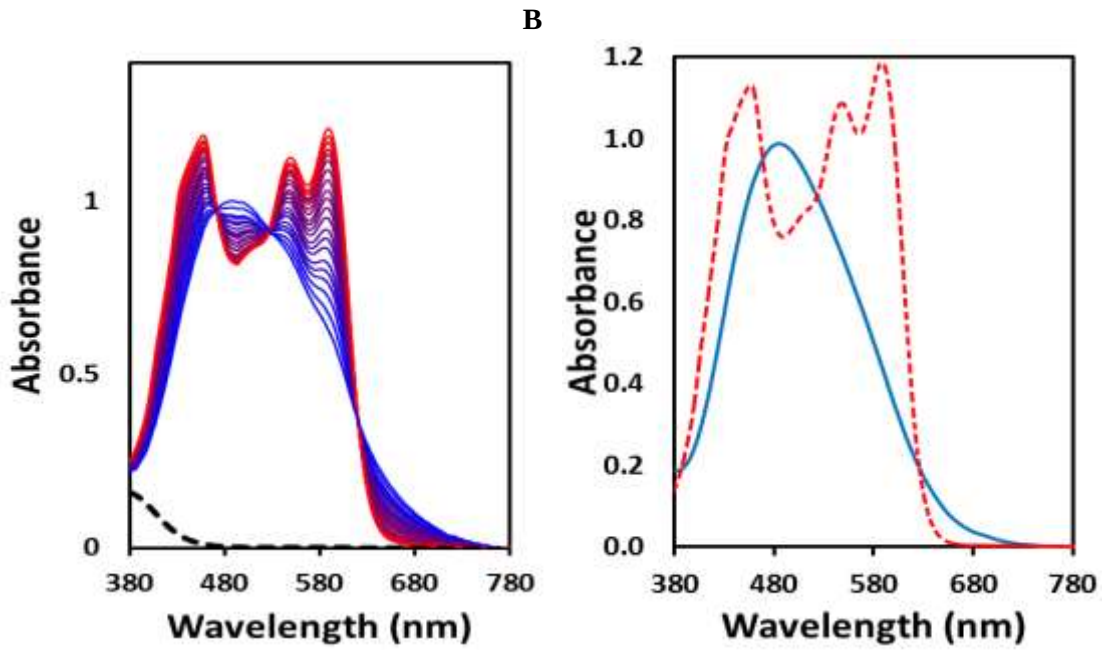

Figure 3-13. Stopped-flow measurements of spectral changes in a DDQ/Br^- solution. **A)** Spectra of a solution of 0.2mM DDQ and 20mM $(Bu_4N)Br$ in acetonitrile over time. Time (s), from blue to red lines: 0.04, 0.09, 0.14, 0.19, 0.24, 0.29, 0.39, 0.49, 0.59, 0.74, 0.94, 1.19, 1.49, 1.79, 2.49, 3.24, 3.99, 5.24, 6.49, 9.99 and 14.99. Separate DDQ spectrum shown as dashed black line. **B)** Spectra of the persistent [DDQ, Br^-] complex measured upon mixing of DDQ and $(Bu_4N)Br$ at -80°C in dichloromethane (blue line) and of $DDQ^{\bullet-}$ obtained by dissolution of crystalline $(Pr_4N)DDQ$ salt in dichloromethane at room temperature (dashed red line).

Comparing the low-temperature spectrum of the DDQ/Br^- solution in Figure 3-13B with spectra from the mixture of other π-acceptors with Br^- (vide infra) allowed for assignation of this new absorption band to the anion-π complex [DDQ, Br^-]. This complex was not observed in the solid state, however, because crystallizations using the method outlined in Chapter 2 resulted in the formation of a mixed-valence $(Pr_4N)_2(DDQ)_3$ salt (Figure 3-14), where π-π stacking of a neutral DDQ molecule between two $DDQ^{\bullet-}$ molecules occurred forming the DDQ_3^{2-} trimer. This is similar to that reported earlier for a DDQ salt with Et_4N^+ cations or a CA salt with 4-dimethylamino-*N*-methylpyridinium cations.[27]

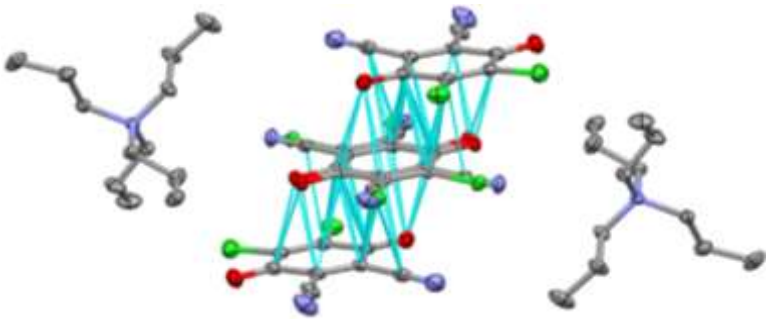

Figure 3-14. X-ray structure of $(Pr_4N)_2(DDQ)_3$ salt showing the π-bonded DDQ_3^{2-} trimer from reference 27. Blue lines are contacts shorter than the sum of the van der Waals radii of the atoms. For clarity, hydrogen atoms not shown.

Adding fluoride (F^-) to a DDQ solution resulted in the appearance of some absorption bands characteristic of $DDQ^{\bullet-}$, which vanished at higher F^- concentrations (Figure 3-15).

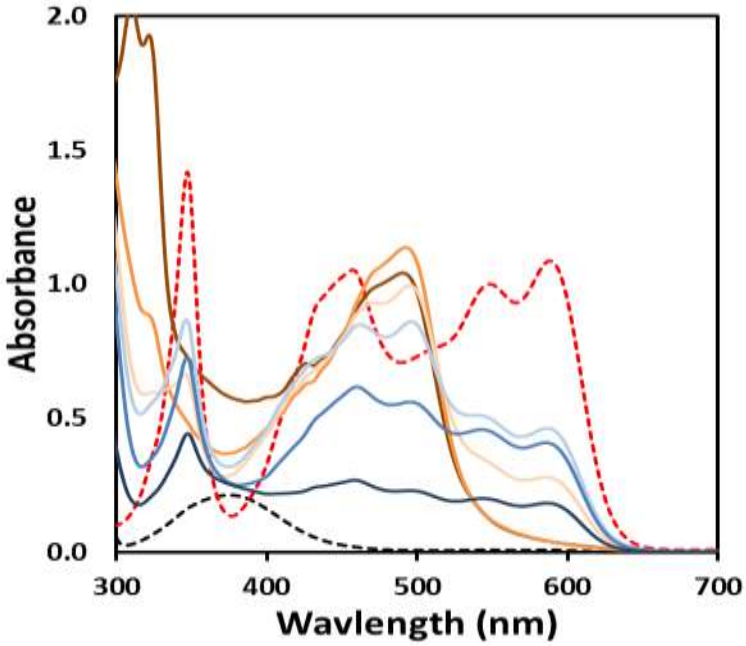

Figure 3-15. Spectral changes resulting from the addition of $(Bu_4N)F$ to 2.64mM solution of DDQ in acetonitrile. Dashed black line shows the spectrum of DDQ itself. Concentration of $(Bu_4N)F$ added (in mM, solid lines, from blue to brown): 2.5, 6.3, 12.7, 17.8, 45.7, 127. Red dashed line is the $DDQ^{\bullet-}$ spectrum.

The reduction of DDQ by F^- is not allowed thermodynamically (recall from Chapter 1 that DDQ has a E_{red} of 0.52V vs. SCE in acetonitrile while F^- has a E_{ox} of 3.06V), yet characteristic peaks of the $DDQ^{\bullet-}$ spectrum were observed at equimolar concentrations of DDQ and F^- in solution (Figure 3-16A). This suggests that some alternative pathway to redox reactions exists.

Even though $DDQ^{\bullet-}$ is seen in the DDQ/F^- spectra, its yield was less than that obtained from reactions of DDQ with either I^- or Br^- (Figure 3-16B). For example, the DDQ/I^- reaction at equimolar (2.5mM) reactant concentrations led to formation of 1.4mM $DDQ^{\bullet-}$, while an equivalent experiment with Br^- and F^- yielded only 0.43mM and 0.29mM $DDQ^{\bullet-}$, respectively. As such, the yield of $DDQ^{\bullet-}$ in the DDQ/I^- solution of 56% is approaching that implied by the reaction stoichiometry laid out in Equation 3-2 (67%). In comparison, yields of $DDQ^{\bullet-}$ in solutions of equivalent concentrations with DDQ/Br^- and DDQ/F^- (17% and 12%, respectively) are far lower.

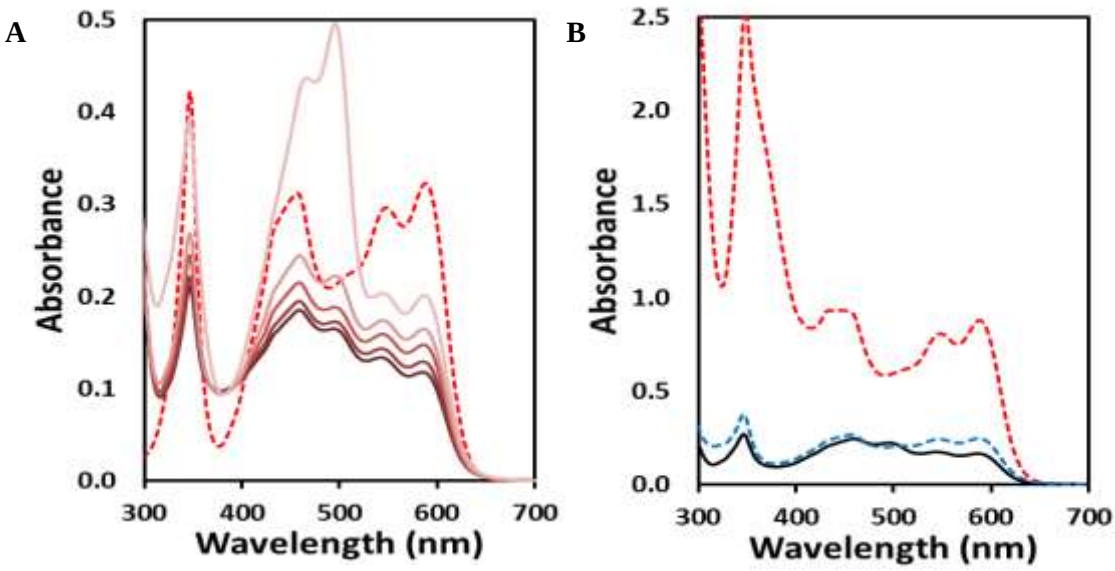

Figure 3-16. Spectral changes in DDQ/F^- solution showing formation of radical anion. **A)** Solid lines show reaction of 2.5mM DDQ with 2.5mM $(Pr_4N)F$ in acetonitrile over time. From bottom to top: Immediate, after 1 min, after 5 min, after 15 min, and after 24 hours. Dashed red line shows the $DDQ^{\bullet-}$ spectrum. **B)** Comparison of the reactions of 2.5mM DDQ with 2.5mM F^- (solid line), 2.5mM I^- (dashed red line), and 2.5mM Br^- (dashed blue line).

Attempts at crystallization of the products of the DDQ/F^- reaction via the method outlined in Chapter 2 resulted in the formation of crystals of $DDQ^{\bullet-}$ seen previously (Figure 3-11) together with oil by-products.

After studying the interactions between DDQ and halides, the resulting products follow the trend in halide oxidation potentials for Cl^-, Br^-, and I^-. $DDQ^{\bullet-}$ was generated fastest and in a largest yield from reactions of DDQ with I^-, which has the lowest oxidation potential. Reduction of DDQ with Br^- was both slower and less efficient. In fact, at low temperature the formation of the persistent [DDQ, Br^-] complex was observed. In solutions of DDQ with Cl^-, anion-π complexes formed instead of electron-transfer products. Therefore, the interaction of DDQ with F^- was expected to be anion-π bonding since F^- has an oxidation potential higher than Cl^-. Instead, at low F^- concentrations $DDQ^{\bullet-}$ bands were observed, along with other large peaks. The concentration of $DDQ^{\bullet-}$ produced from this solution was less than the amount produced from reduction with Br^-, and at higher F^- concentrations, the bands corresponding to $DDQ^{\bullet-}$ disappeared entirely while the other unidentified peaks became more pronounced. The product(s) of these reactions at higher F^- concentrations was not identified. To verify these observed trends and establish causation for any variations, the interactions of halide anions with the other p-benzoquinone (BQ) acceptors from Figure 1-11 were examined.

II. **Shift from complex formation to redox-reactions in solutions of halides with different p-benzoquinones**

i. Interactions of tetrahalo-substituted p-benzoquinones with halides

As with DDQ, the other studied p-benzoquinones (BQs) underwent reduction to their respective radical anion upon mixing with iodide (I^-). All three tetrahalo-substituted BQs (p-bromanil (BA), p-chloranil (CA), and p-fluoranil (FA)) have lower reduction potentials (0.02V, -0.02V, and -0.01V vs. SCE in acetonitrile, respectively) than DDQ (0.52V vs. SCE in acetonitrile), making them weaker π-acceptors. Still, addition of $(Pr_4N)I$ to a CA solution in acetonitrile led to fast appearance of sharp absorption bands similar to what was reported earlier for the chloranil radical anion ($CA^{\bullet-}$) (Figure 3-17B).[28] To confirm these sharp peaks indeed represented $CA^{\bullet-}$, the spectrum of $CA^{\bullet-}$ was obtained via bulk electrolysis (Figure 3-17A).

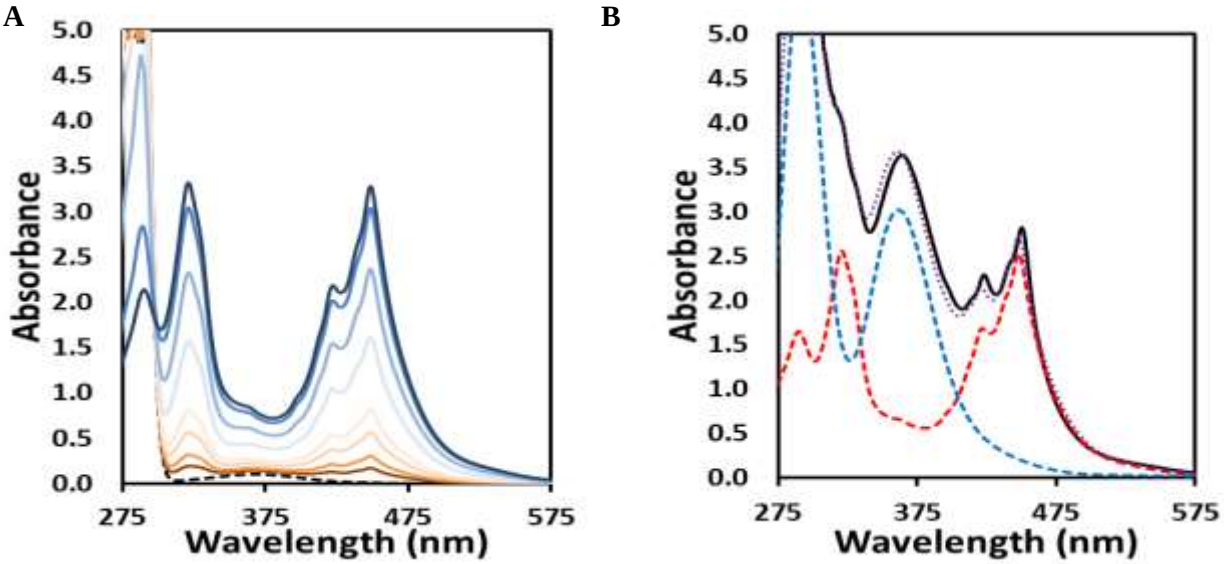

Figure 3-17. A) $CA^{\bullet-}$ spectra obtained by electrolysis at -0.3V of 5.29mM CA with 0.1M $(Bu_4N)PF_6$ as electrolyte. Dashed line is the spectrum of CA itself. **B)** Spectrum formed immediately upon mixing of 0.65mM CA and 100mM $(Bu_4N)I$ in dichloromethane. Dashed red line represents the separate $CA^{\bullet-}$ spectrum. Dashed blue line is the separate I_3^- spectrum. Dotted purple line is the combined $CA^{\bullet-}$ and I_3^- spectra.

The $CA^{\bullet-}$ spectrum closely resembled that seen for the CA/I^- solution, and overlaying the I_3^- spectrum, analogous to the data treatment performed for DDQ/I^-, resulted in an almost perfect match, as seen in Figure 3-17B. Reactions of I^- with BA or FA led to similar appearances of a spectra corresponding to their radical anions plus I_3^- (Figure 3-18).

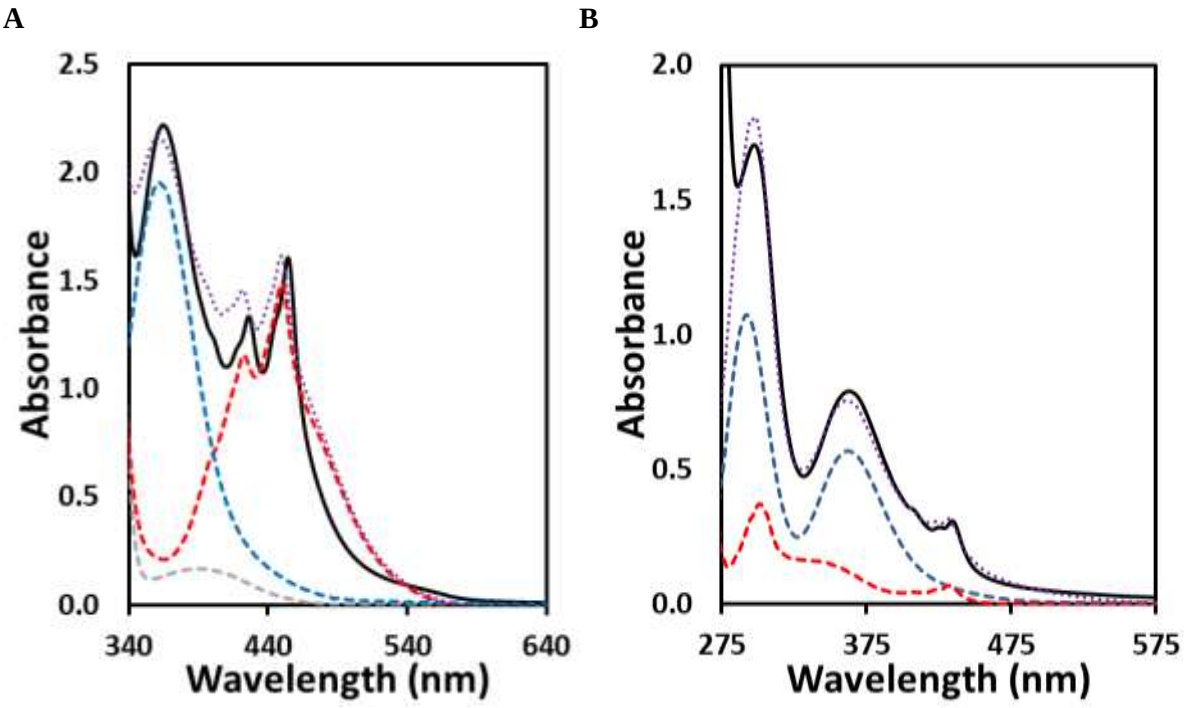

Figure 3-18. A) Spectrum obtained upon mixing of 0.59mM BA with 71.3mM $(Bu_4N)I$. Dashed red line is the $BA^{\bullet-}$ spectrum obtained by bulk electrolysis at -0.4V of 3mM BA with 0.1M $(Bu_4N)PF_6$ as electrolyte, and dashed blue line is the separate I_3^- spectrum. Dotted purple line is the combined $BA^{\bullet-}$ and I_3^- spectra, similar to the BA/I^- spectrum. **B)** Spectrum obtained upon mixing of 0.5mM FA and 75mM $(Bu_4N)I$. Dashed red line is the $FA^{\bullet-}$ spectrum obtained by reduction of FA with the strong reducing agent tetrakis(dimethylamino)ethylene (TDMAE, E_{ox} = -0.78V vs. SCE in acetonitrile)[29] and dashed blue line is the separate I_3^- spectrum. Dotted purple line is the overlaid $FA^{\bullet-}$ and I_3^- spectra, similar to the FA/I^- spectrum.

When the aforementioned BQ/I^- experiments were ran at low temperature (-80°C) using dichloromethane as a solvent, the radical anion spectrum was not observed. Instead, the result was a weak broad absorption band with a peak (λ_{max}) between 500 and 650 nm (Figure 3-19). This band is similar to that seen with the interaction of DDQ with Br^- at low temperature seen in Figure 3-13.

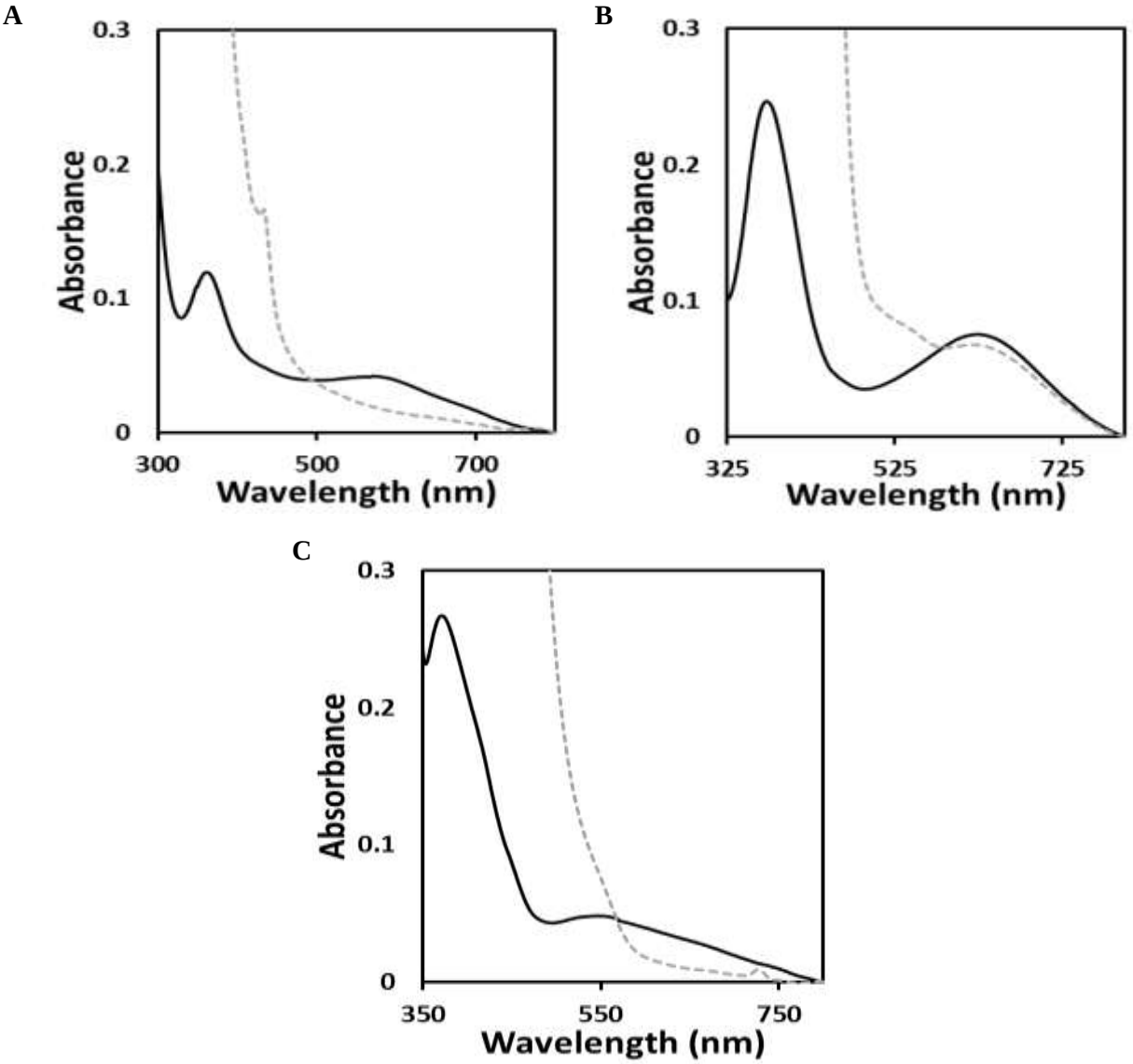

Figure 3-19. BQ/I^- solutions at -80°C vs. room temp. in dichloromethane. **A)** Spectra of 0.6mM BA with 71.3mM $(Bu_4N)I$ at -80°C (solid line) and room temp. (dashed line) **B)** Spectra of 0.65mM CA with 100mM $(Bu_4N)I$. at -80°C (solid line) and room temp. (dashed line) **C)** Spectra of 0.25mM FA and 87.5mM $(Bu_4N)I$ at -80°C (solid line) and room temp. (dashed line).

In order to establish what the low energy band observed at low temperature corresponded to, attempts were made to crystallize products of the BQ/I^- interactions. The product of a solution containing equimolar concentrations of FA and I^- was crystallized via the method described in Chapter 2. X-ray analysis of these crystals revealed that they were comprised of chains formed by the 1:1 association of I^- with FA (Figure 3-20).

A)

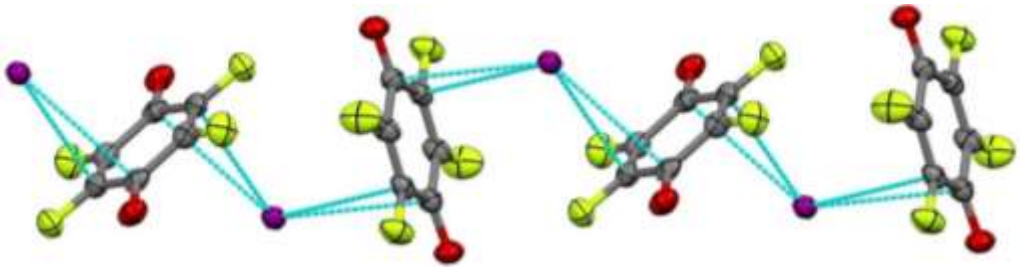

B)

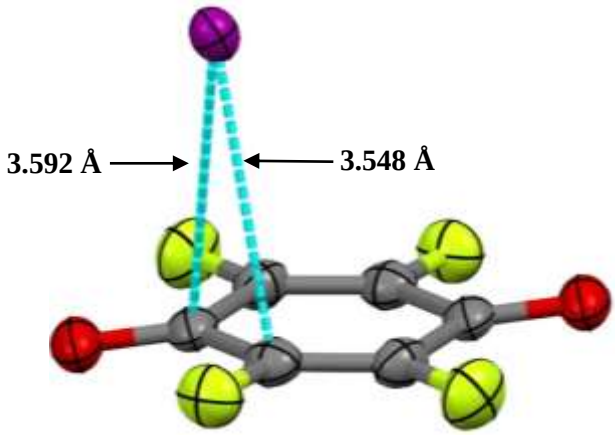

Figure 3-20. A) Crystal lattice structure showing the 1:1 anion-π complex between FA and $(Pr_4N)I$. Blue lines indicate non-covalent contacts between I^- and FA shorter than the sum of the van der Waals radii. **B)** Fragment of FA/$(Pr_4N)I$ crystal structure highlighting interaction of an I^- anion with FA. Blue lines indicate contacts between I^- and carbons on FA molecule that are shorter than the sum of the van der Waals radii of I^- and carbon.

The I^- anions in the crystal structure were located in a similar position over FA as was seen with Cl^- in [DDQ, Cl^-] in Figure 3-9: over the atoms of the BQ's ring, specifically over the bonds between oxygen- and fluoro-substituted carbons. The closest $I^-\cdots C$ distances in these complexes were 3-4% shorter than the sum of the van der Waals radii, indicating a much weaker interaction than seen between DDQ and Cl^-, which were 12-18% shorter.

UV-Vis spectra of solutions of Cl^- anions with BA, CA, or FA displayed new broad bands in the 380 – 400 nm range (Figures 3-21 – 3-23) similar to those observed with DDQ and Cl^-. Concentration dependence studies confirmed that they were associated to the formation of 1:1 complexes equivalent to that in Equation 3-1 (See Figures S-1 – S-3 in Supporting Information for data treatment).

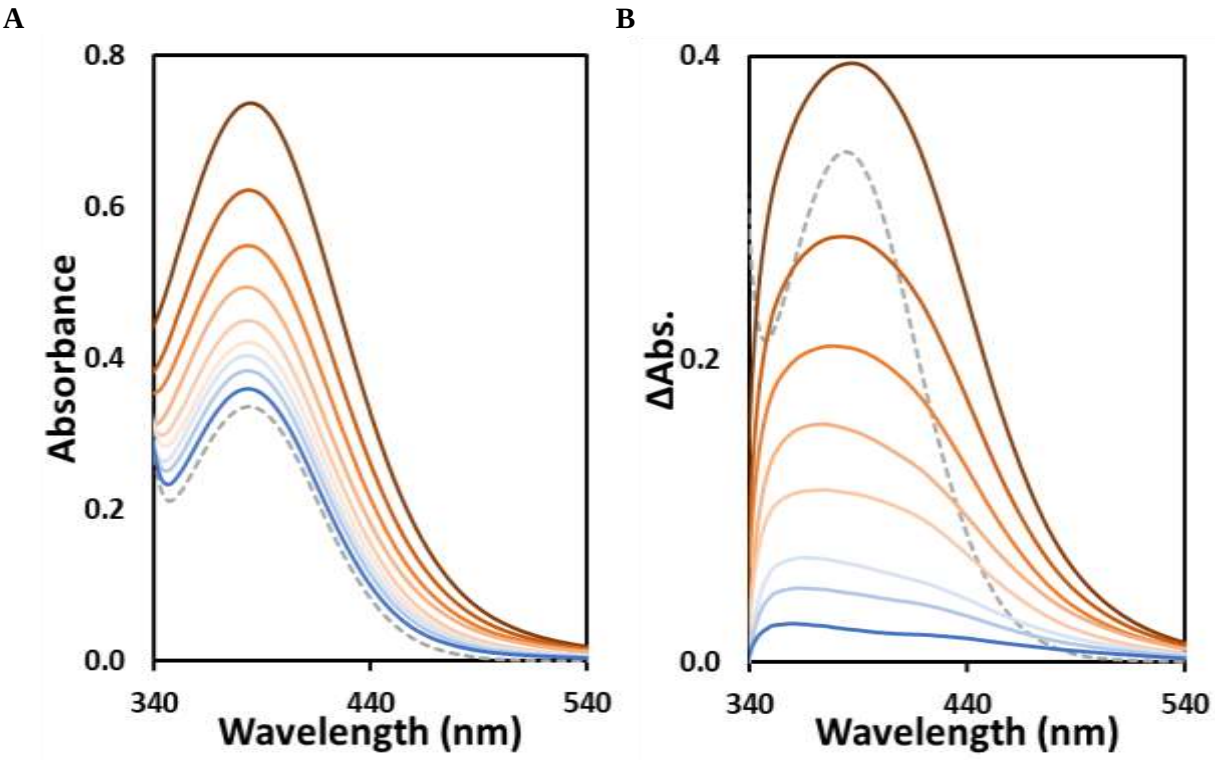

Figure 3-21. Spectral changes in a BA/Cl^- solution upon increasing Cl^- concentrations at constant BA concentration in acetonitrile. **A)** Spectra of 6mM BA with various Cl^- concentrations. Dashed grey line represents the separate BA spectrum. Cl^- conc. from top to bottom (mM): 250.8, 175.6, 125.4, 90.3, 65.2, 45.1, 35.1, 25.1, 12.5. **B)** Spectra after subtraction of separate BA spectrum (dashed grey line).

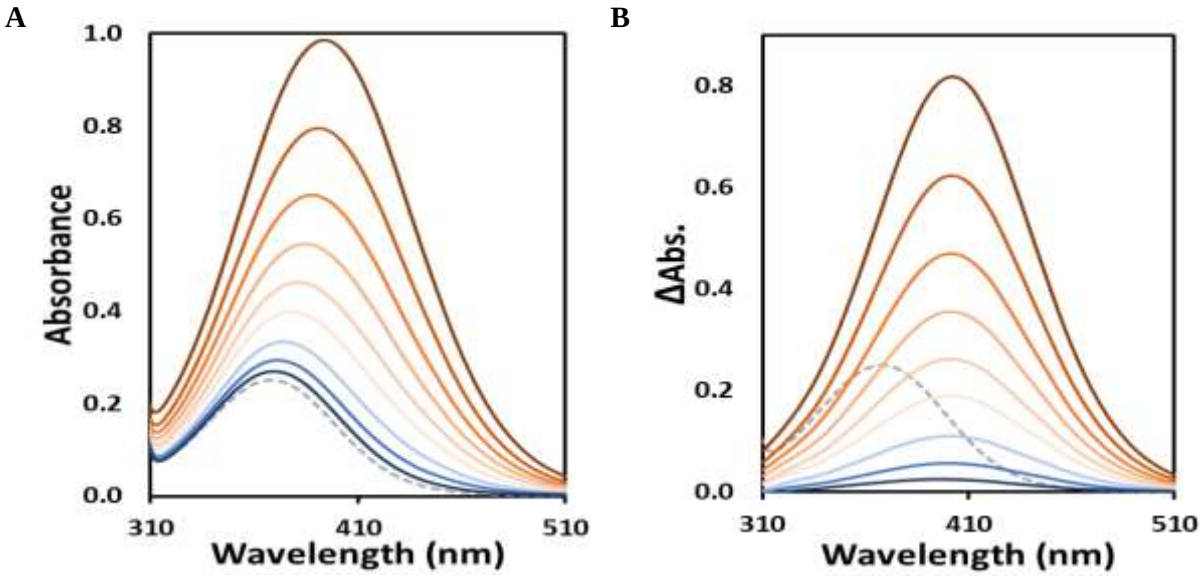

Figure 3-22. A) Spectral changes upon increasing Cl^- concentrations at constant 5mM CA concentration in acetonitrile. Dashed grey line represents the separate CA spectrum. Cl^- conc. from top to bottom (mM): 374.8, 262.4, 187.4, 134.9, 97.5, 67.5, 37.5, 18.7, 7.5. **B)** Spectra after subtraction of separate CA spectrum (dashed grey line).

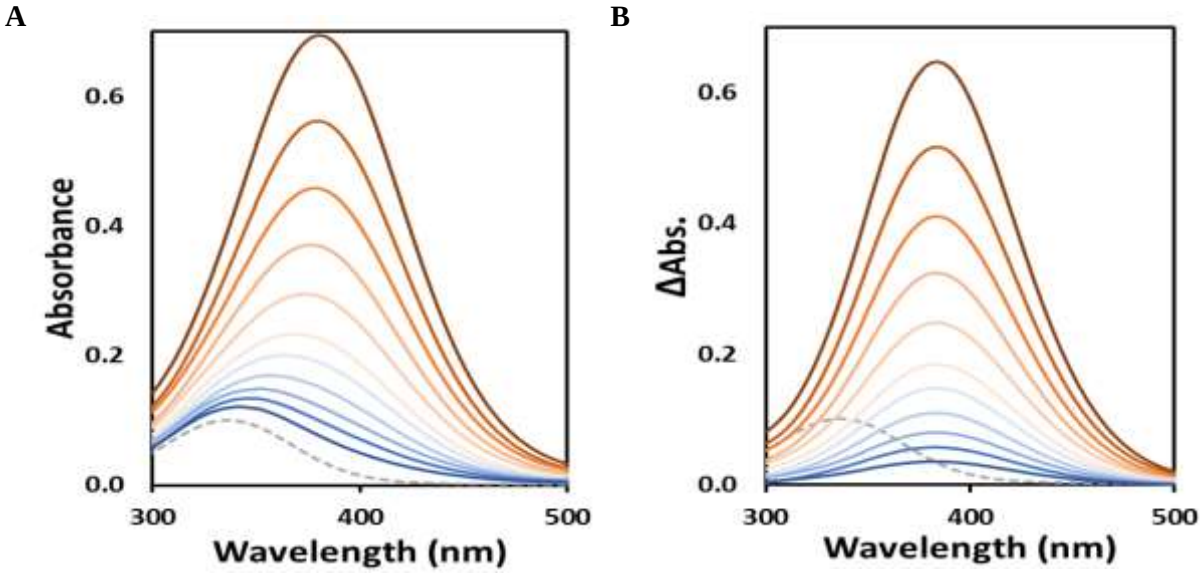

Figure 3-23. A) Spectral changes upon increasing Cl^- concentrations at constant 2.4mM FA concentration in acetonitrile. Dashed grey line represents the separate FA spectrum. Cl^- conc. from top to bottom (mM): 250.1, 175.1, 125.1, 90, 65, 45, 35, 25, 17.5, 12.5, 7.5. **B)** Spectra after subtraction of separate FA spectrum (dashed grey line).

Similarly, UV-Vis spectra of solutions of Br^- anions with BA, CA, or FA displayed new broad bands, but they were shifted bathochromically in the range of 440 – 460 nm (Figures 3-24 – 3-26). Concentration dependence studies and a Job plot for FA and $(Pr_4N)Br$ (Figure 3-27) once again confirmed this new peak is the formation of 1:1 complexes equivalent to that in Eq. 3-1 (See Figures S-6 – S-8 in Supporting Information for data treatment).

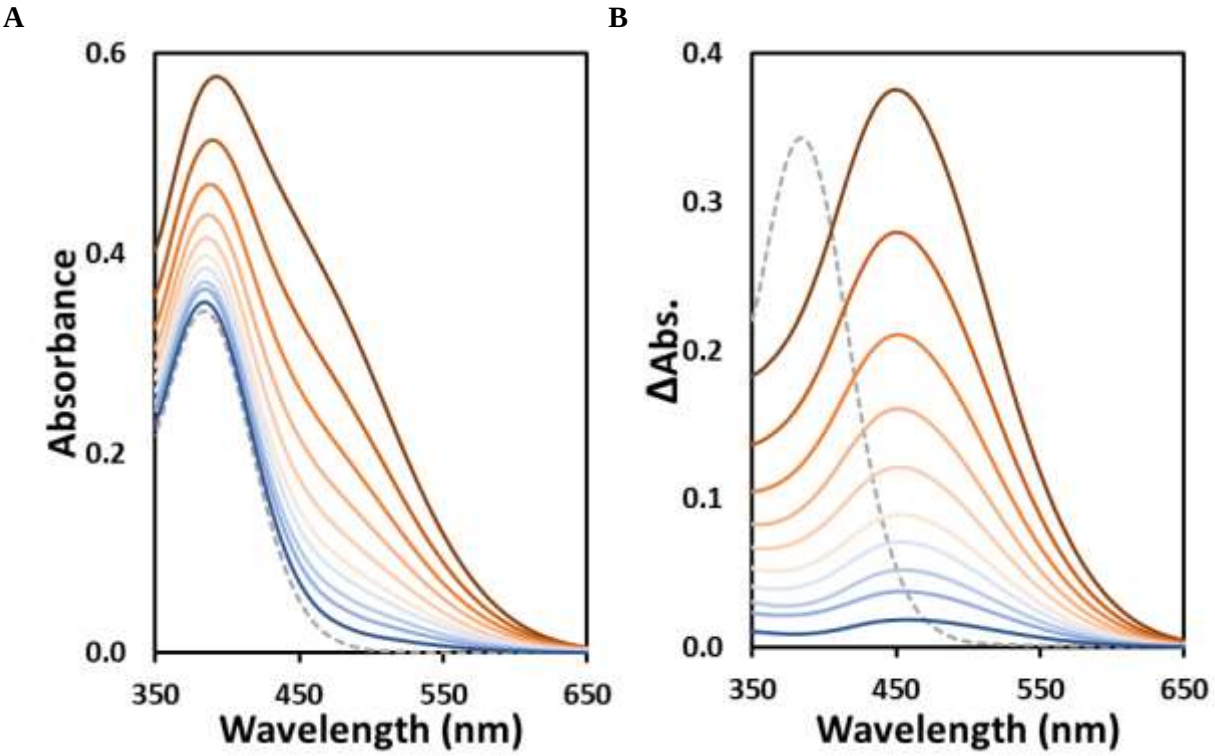

Figure 3-24. Spectral changes in BA/Br^- solution upon increasing Br^- concentrations at constant BA concentration in acetonitrile. **A)** Spectra of 6mM BA with varying Br^- concentrations. Dashed grey line represents the separate BA spectrum. Br^- conc. from top to bottom (mM): 250, 175, 125, 90, 65, 45, 35, 25, 17.5, 7.5. **B)** Spectra after subtraction of the separate BA spectrum (dashed grey line).

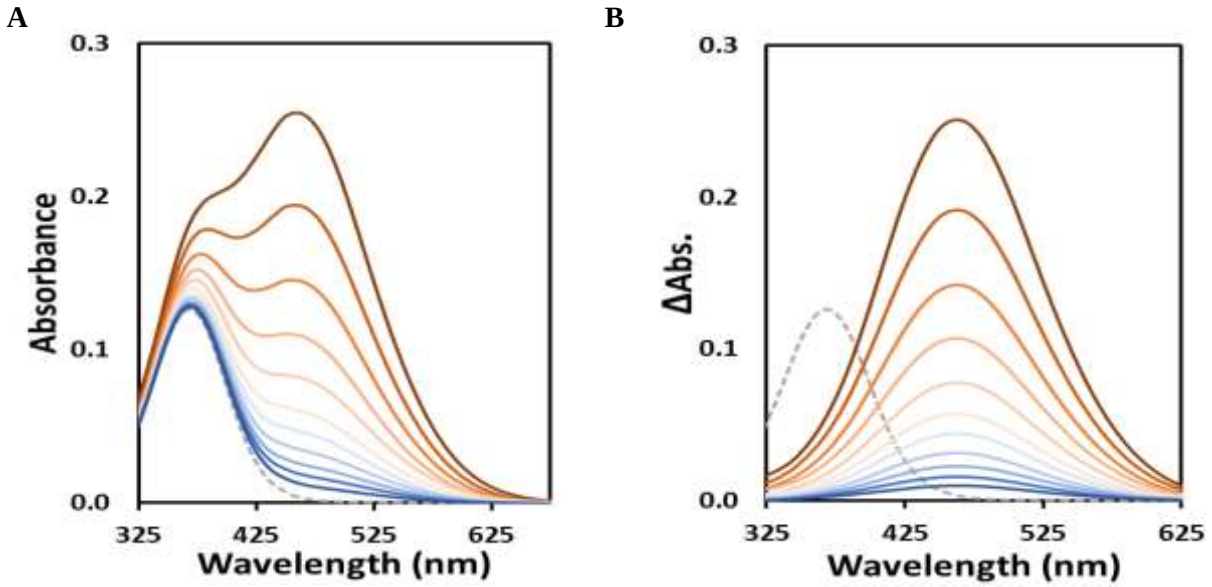

Figure 3-25. A) Spectral changes in CA/Br^- solution upon increasing Br^- concentrations at constant 2.4mM CA concentration in acetonitrile. Dashed grey line represents the separate CA spectrum. Br^- conc. from top to bottom (mM): 250.2, 175.1, 125.1, 90.1, 65, 45, 35, 25, 17.5, 12.5, 7.5. **B)** Spectra after subtraction of the separate CA spectrum (dashed grey line).

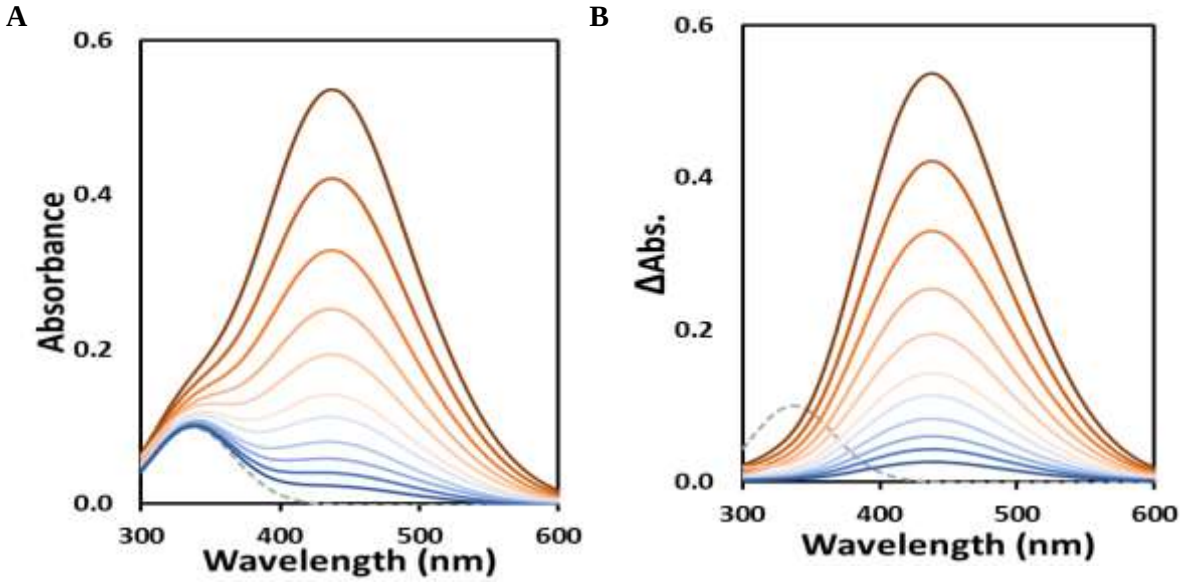

Figure 3-26. A) Spectral changes in FA/Br^- solution upon increasing Br^- concentrations at constant 2.5mM FA concentration in acetonitrile. Dashed grey line represents the separate FA spectrum. Br^- conc. from top to bottom (mM): 249.7, 174.8, 124.9, 89.9, 64.9, 44.9, 35, 25, 17.5, 12.5, 7.5. **B)** Spectra after subtraction of the separate FA spectrum (dashed grey line).

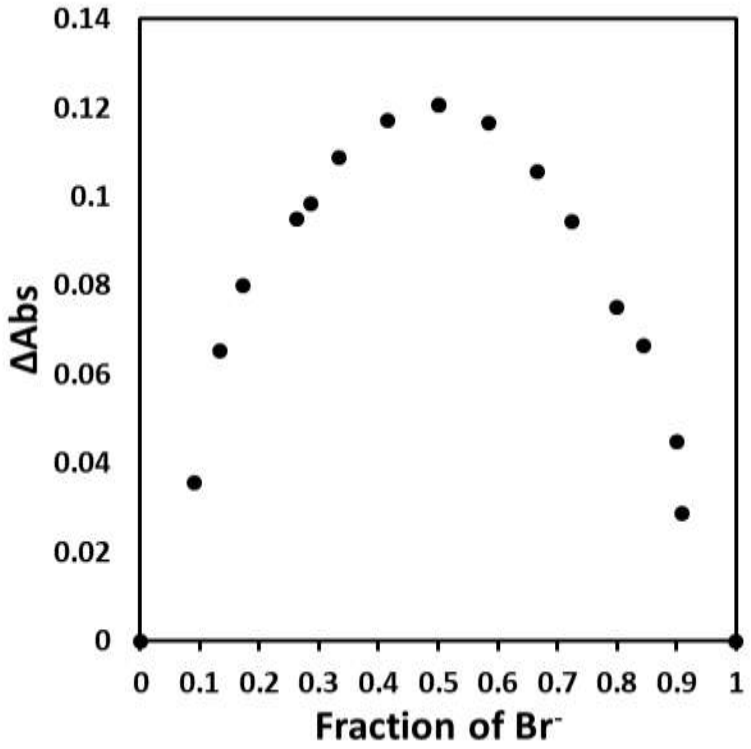

Figure 3-27. Dependence of the complex absorption on the molar fraction of bromide present in a solution of FA with $(Pr_4N)Br$ in acetonitrile (Job plot). The sum of the concentration of components was held constant (3mM).

The X-ray crystal structure of [FA, Br^-] was obtained via low-temperature crystallization from dichloromethane solutions in two different configurations. The first was attained by mixing FA and $(Pr_4N)Br$ at equimolar concentrations. The resulting crystals were formed at a 1:1 ratio of FA to Br^- with contacts 5-6% shorter than the sum of their van der Waals radii (Figure 3-28A). The second structure was obtained by adding $(Pr_4N)Br$ in large excess to a FA solution. These crystals were comprised of 2:1 complexes with one Br^- anion interacting on each side of the FA molecule (Figure 3-28B). In this "sandwich" complex, the interatomic distance between Br^- and FA is greater, only faintly shorter than the van der Waals radii (~0.5%). Br^- anions in this conformation were located closer to ring centroid rather than over the bonds of the ring.

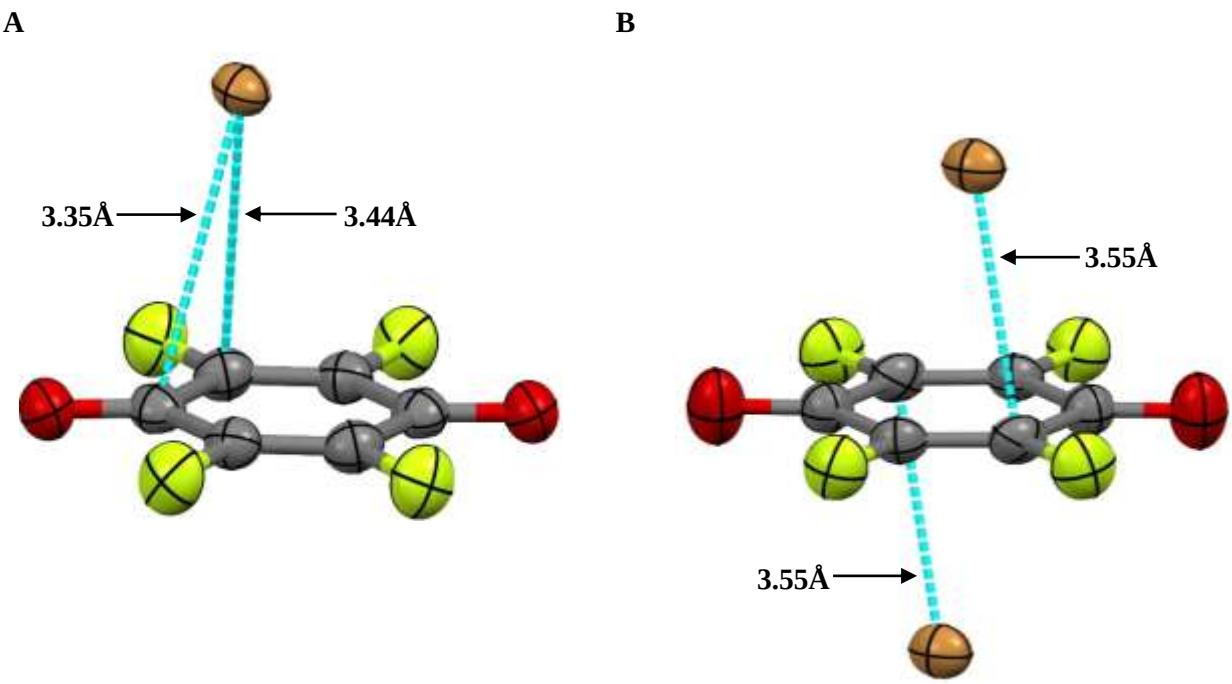

Figure 3-28. Two different versions of [FA, Br^-] crystal structure created via low temperature crystallization outlined in Chapter 2. **A)** Crystal structure fragment of [FA, Br^-] achieved when a 1:1 ratio of analytes is used. Blue lines indicate contacts between Br^- and carbons on FA molecule that are shorter than the sum of their van der Waals radii**. B)** Crystal structure fragment of [FA, Br^-] achieved when Br^- is added in large excess. Blue lines indicate contacts between Br^- and carbons on FA molecule that are shorter than the sum of their van der Waals radii.

The spectra resulting from the interaction of BA, CA, and FA with F^- resulted initially in the formation of broad bands with maximum around 550 nm similar to those seen for the 1:1 anion-π complexes (Figure 3-29). However, after a short time the intensities of these bands decreased and new higher-energy bands appeared. This signifies that complexes are formed initially as a precursor to an additional reaction. Yet minimal, if any, radical anion formation was found in these solutions.

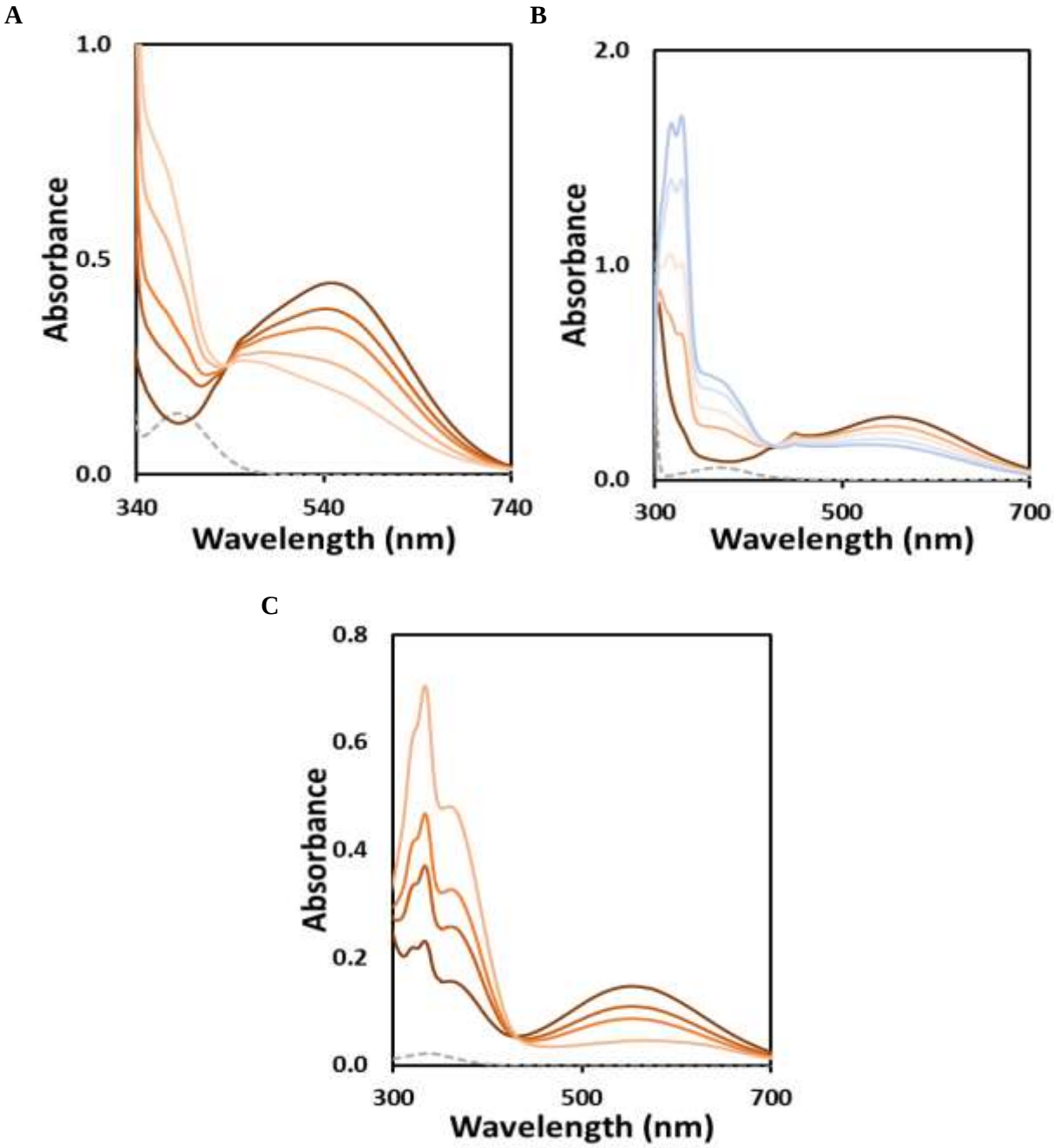

Figure 3-29. A) Spectra of 5.2mM BA with 247.2mM F^- after subtraction of BA spectrum (dashed line). From top to bottom: immediately, after 1 min, after 2 min, after 5 min, after 15 min. **B)** Spectra of 2.2mM CA with 90mM F^- after subtraction of CA spectrum (dashed line). From top to bottom: immediately, after 3 min, after 5 min, after 10 min, after 15 min. **C)** Spectra of 1.5mM FA with 300.1mM F^- after subtraction of FA spectrum (dashed line). From top to bottom: immediately, after 1 min, after 2 min, after 10 min.

ii. Interactions of dichloro-substituted p-benzoquinones with halides

After completing experiments involving BA, CA, and FA, reactions of 2,6-dichloro-p-benzoquinone (2,6-Cl_2BQ) and 2,5-dichloro-p-benzoquinone (2,5-Cl_2BQ) with halides were studied. These two BQs are only dihalo-substituted, therefore, 2,6-Cl_2BQ and 2,5-Cl_2BQ have the most negative reduction potentials of the π-acceptors included in this work (-0.18V and -0.2V vs. SCE in acetonitrile, respectively), making them the weakest π-acceptors studied.

UV-Vis spectra of solutions of 2,6-Cl_2BQ with Cl^- or Br^- yielded a new broad band with λ_{max} at 375 or 430 nm respectively, similar to the spectra observed in solutions of tetrahalo-substituted BQs with these halides (Figures 3-30 – 3-31). Band intensities for these complexes, however, were much smaller when compared to the other BQs interacting with these X^- at the same concentrations (see Figures S-4 and S-9 in Supporting Information for data treatment).

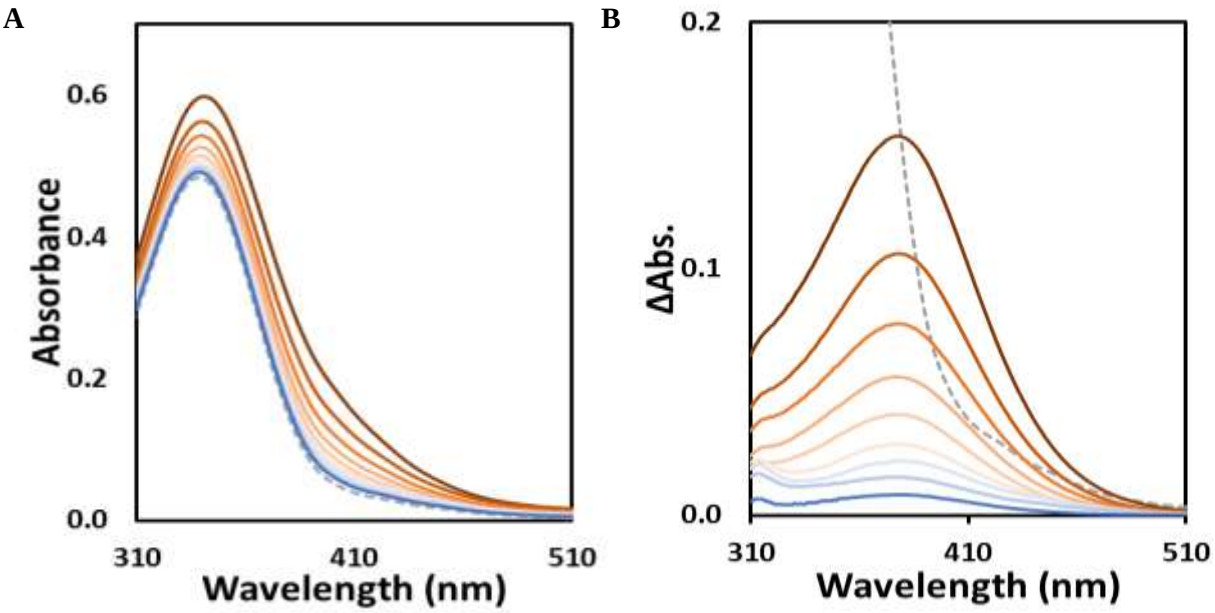

Figure 3-30. Spectral changes in 2,6-Cl_2BQ/Cl^- solution upon increasing Cl^- concentrations at constant 2,6-Cl_2BQ concentration in acetonitrile. **A)** Spectra of 5.1mM 2,6-Cl_2BQ with varying Cl^- concentrations. Dashed grey line represents the separate 2,6-Cl_2BQ spectrum. Cl^- conc. from top to bottom (mM): 374.8, 262.3, 187.4, 134.9, 97.4, 67.5, 52.5, 37.5, 18.7. **B)** Spectra after subtraction of the separate 2,6-Cl_2BQ spectrum (dashed grey line).

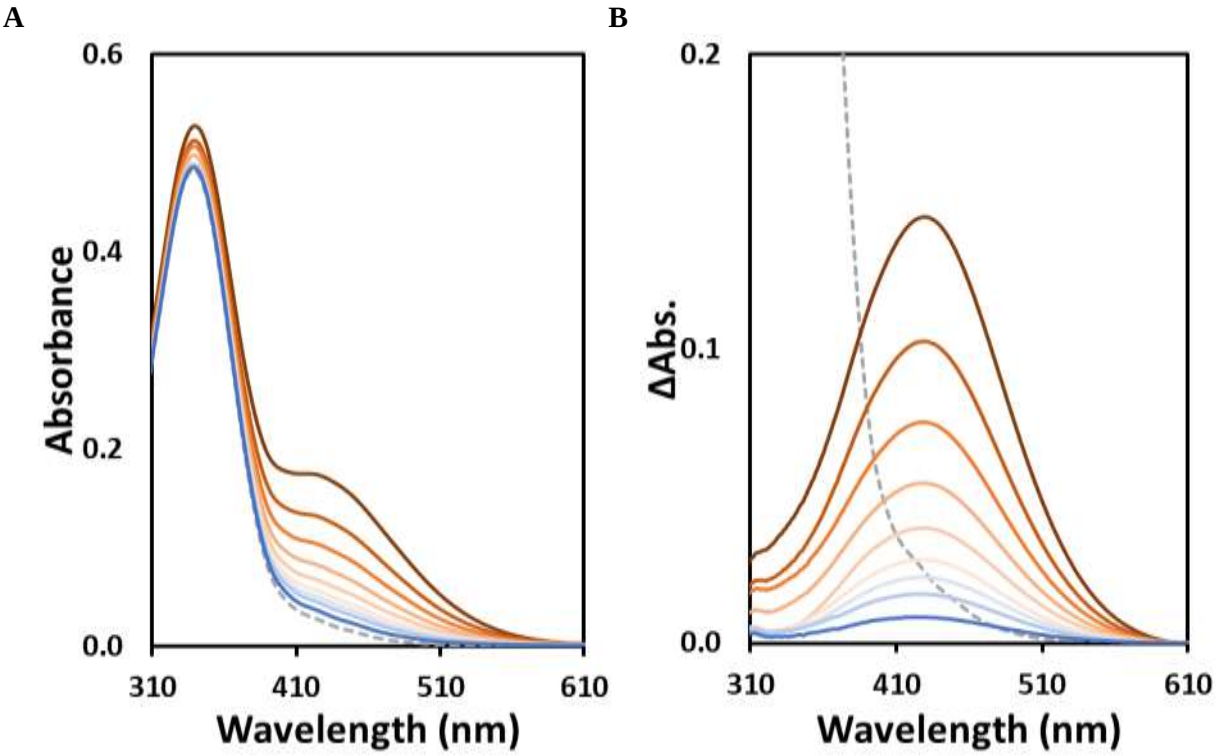

Figure 3-31. Spectral changes in a 2,6-Cl_2BQ/Br^- solution upon increasing Br^- concentrations at constant 2,6-Cl_2BQ concentration in acetonitrile. **A)** Spectra of 5.1mM 2,6-Cl_2BQ with varying Br^- concentrations. Dashed grey line represents the separate 2,6-Cl_2BQ spectrum. Br^- conc. from top to bottom (mM): 375.1, 262.6, 187.5, 135, 97.5, 67.5, 52.5, 37.5, 18.8. **B)** Spectra after subtraction of the separate 2,6-Cl_2BQ spectrum (dashed grey line).

UV-Vis spectra of solutions of 2,5-Cl_2BQ with Cl^- or Br^- gave almost identical band data (Figures 3-32 – 3-33), resulting in the formation of a new broad peak with λ_{max} at 374 or 430 nm respectively. Like before, these band intensities were much less than seen previously in equivalent interactions of these halides with other BQs (see Figures S-5 and S-10 in Supporting Information for data treatment).

A

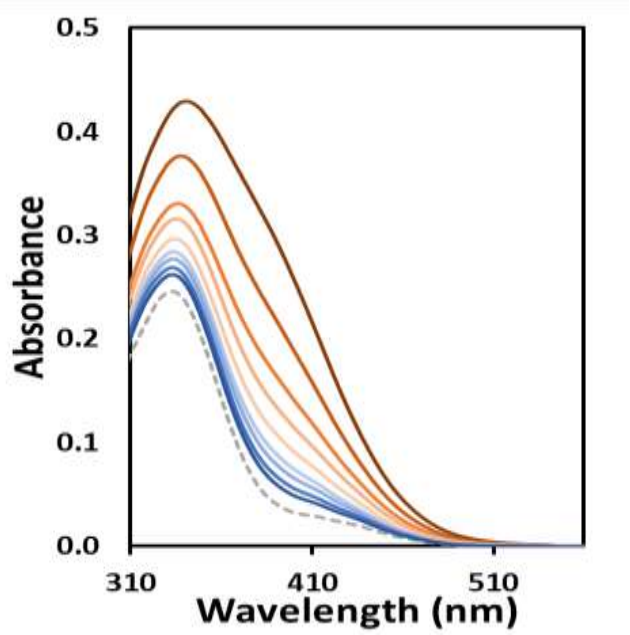

B

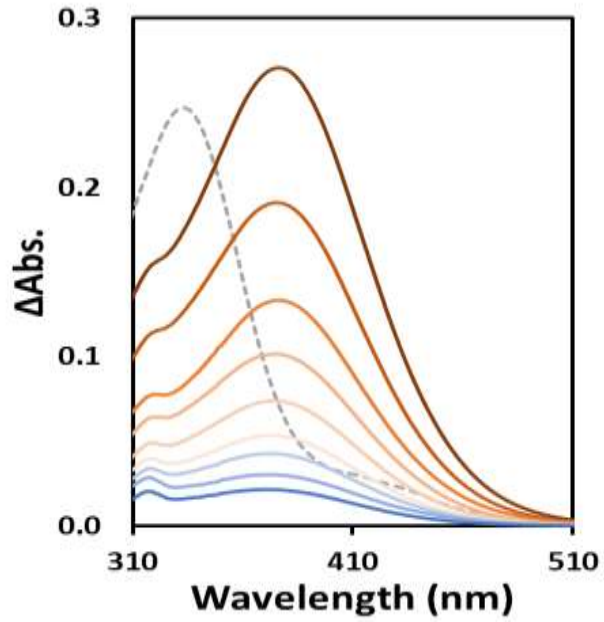

Figure 3-32. Spectral changes in 2,5-Cl_2BQ/Cl^- solution upon increasing Cl^- concentrations at constant 2,5-Cl_2BQ concentration in acetonitrile. **A)** Spectra of 5mM 2,5-Cl_2BQ with varying Cl^- concentrations. Dashed grey line represents the separate 2,5-Cl_2BQ spectrum. Cl^- conc. from top to bottom (mM): 745.7, 522, 372.8, 268.4, 193.9, 134.2, 104.4, 74.6, 52.2. **B)** Spectra after subtraction of the separate 2,5-Cl_2BQ spectrum (dashed grey line).

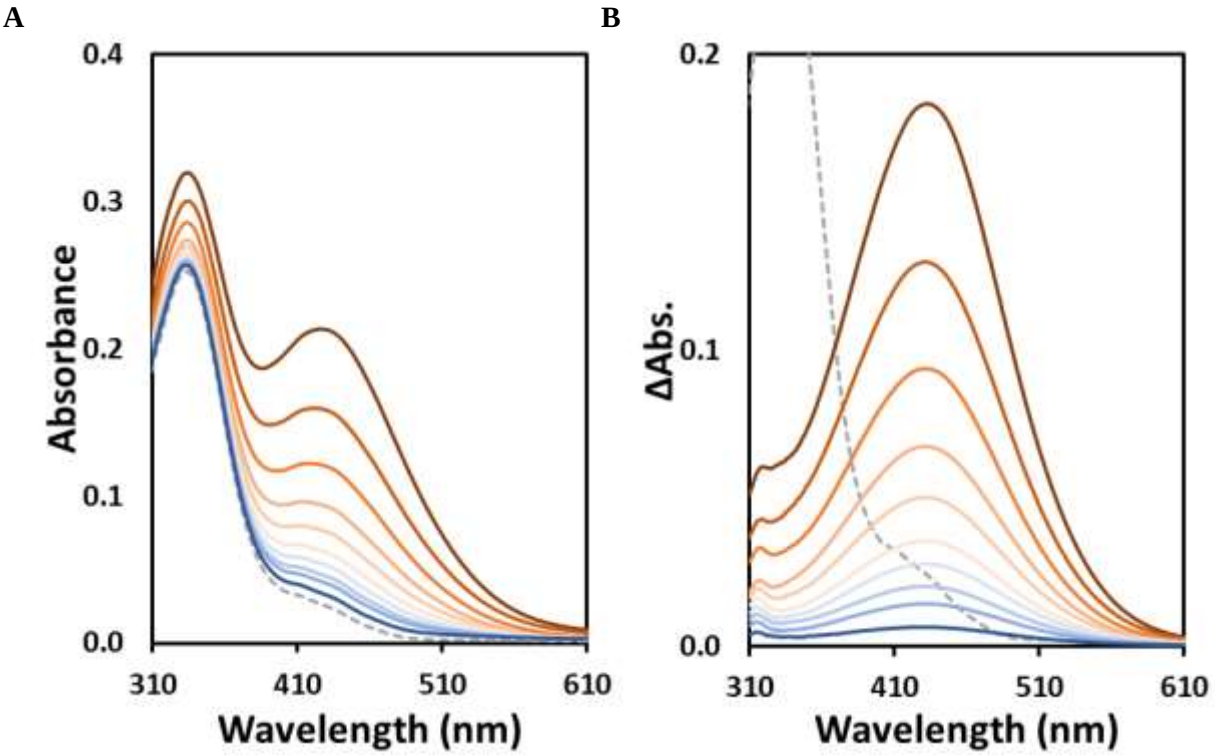

Figure 3-33. Spectral changes in 2,5-Cl_2BQ/Br^- solution upon increasing Br^- concentrations at constant 2,5-Cl_2BQ concentration in acetonitrile. **A)** Spectra of 5.1mM 2,5-Cl_2BQ with varying Br^- concentrations. Dashed grey line represents the separate 2,5-Cl_2BQ spectrum. Br^- conc. from top to bottom (mM): 454.2, 318, 227.1, 163.5, 118.1, 81.8, 63.6, 45.4, 31.8, 13.6. **B)** Spectra after subtraction of the separate 2,5-Cl_2BQ spectrum (dashed grey line).

UV-Vis spectra of solutions of both dichloro-substituted BQs with I^- yielded different results than were seen for the other BQs studied (Figures 3-34 – Figure 3-35). Hardly any trace of the radical anion spectra usually observed after I^- addition to a BQ solution was present, and instead a new broad low-energy band emerged. This band showed an increase in intensity with an increase in I^- concentration, and the largest band intensity was observed at a 1:1 ratio of reactants (when the sum of reactant concentrations was held constant, Job plot in Figure 3-36), both of which signify anion-π complex formation (see Figures S-11 and S-12 in Supporting Information for data treatment).

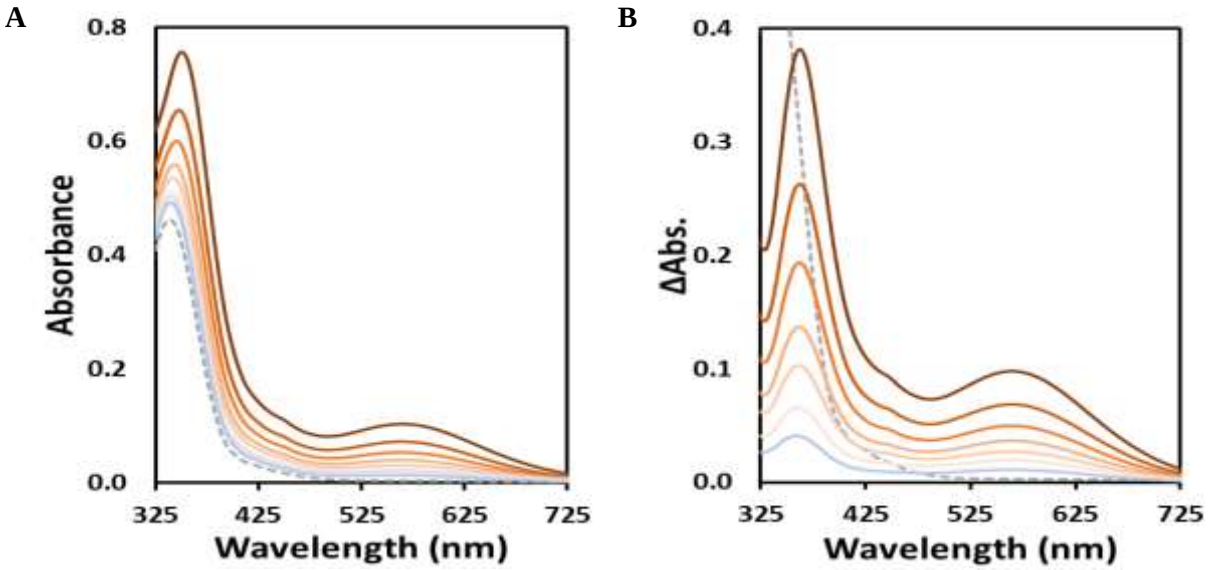

Figure 3-34. A) Spectral changes in 2,6-Cl_2BQ/I^- solution upon increasing I^- conc. at constant 5mM 2,6-Cl_2BQ conc. in acetonitrile. Dashed grey line represents the separate 2,6-Cl_2BQ spectrum. I^- conc. from top to bottom (mM): 249, 174.3, 124.5, 89.6, 64.7, 44.8, 24.9. **B)** Spectra after subtraction of separate 2,6-Cl_2BQ spectrum (dashed grey line).

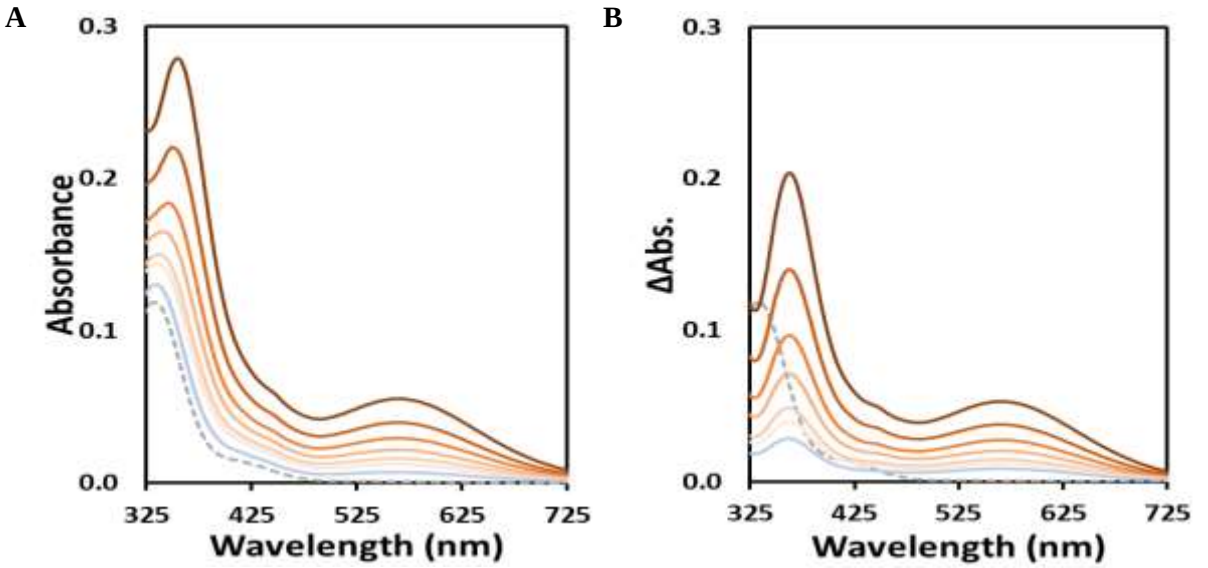

Figure 3-35. A) Spectral changes in 2,5-Cl_2BQ/I^- solution upon increasing I^- conc. at constant 5mM 2,5-Cl_2BQ conc. in acetonitrile. Dashed grey line represents the separate 2,5-Cl_2BQ spectrum. I^- conc. from top to bottom (mM): 249, 174.3, 124.5, 89.6, 64.7, 44.8, 24.9. **B)** Spectra after subtraction of separate 2,5-Cl_2BQ spectrum (dashed grey line).

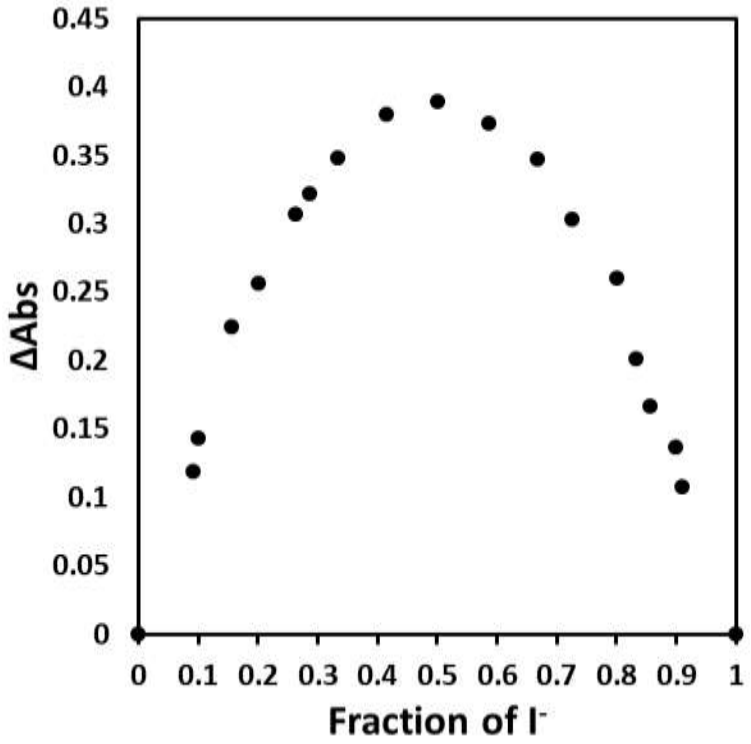

Figure 3-36. Dependence of the complex absorption on the molar fraction of iodide present in a solution of 2,6-Cl_2BQ with (Bu_4N)I in acetonitrile (Job plot). The sum of the concentration of components was held constant (0.2M).

Interestingly, interactions of these dichloro-substituted BQs with F^- resulted in the formation of intense peaks similar to those observed for the radical anions. Radical anion spectra consistent with the literature data were obtained in the same method used to reduce FA: by reduction of these acceptors using the strong reducing agent tetrakis(dimethylamino)ethylene (TDMAE, E_{ox} = -0.78V vs. SCE in acetonitrile)[29] at a 2:1 ratio of BQ to TDMAE. When comparing this spectrum to those from interactions with F^-, the BQ/F^- spectra show a broad absorption band that appears as a side peak with a λ_{max} around 550 nm (Figure 3-37).

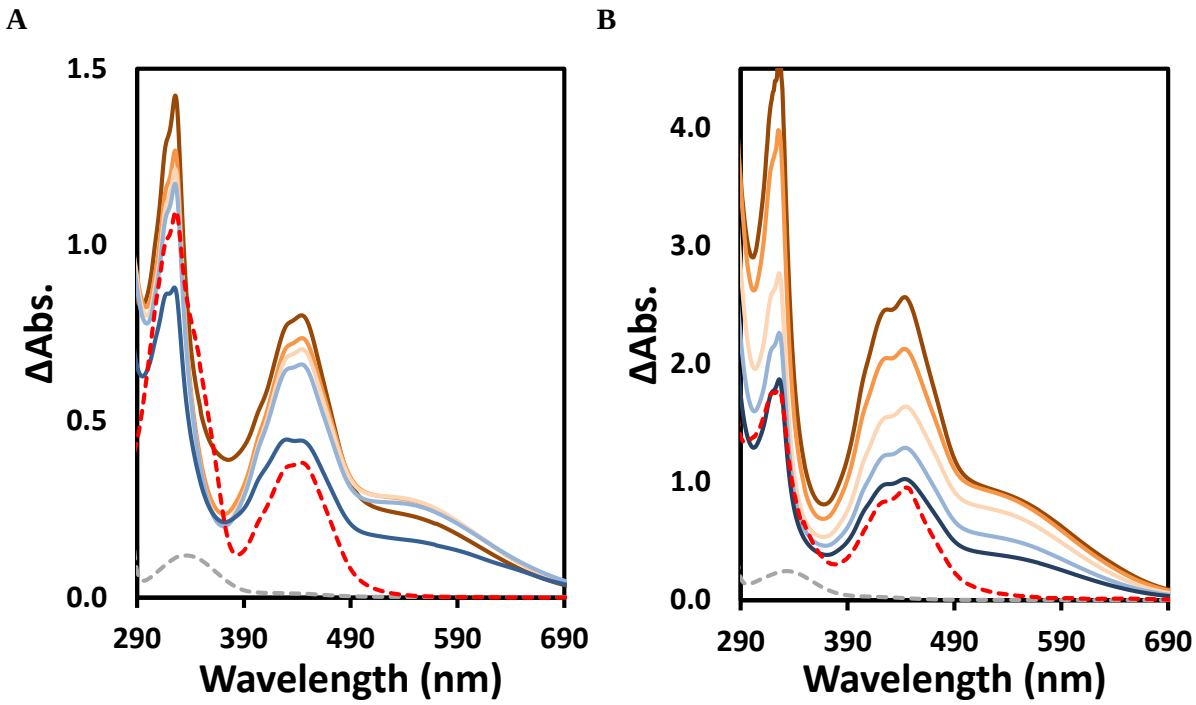

Figure 3-37. A) Spectral changes in 2,6-Cl_2BQ/F^- solution in acetonitrile upon increasing F^- conc. at constant 2.5mM 2,6-Cl_2BQ conc. after subtraction of the separate 2,6-Cl_2BQ spectrum (dashed grey line). Dashed red line shows the 2,6-$Cl_2BQ^{\bullet-}$ spectrum obtained from reduction with TDMAE. F^- conc. from top to bottom (mM): 71.2, 26.5, 18.3, 10.2, 5.1. **B)** Spectral changes in 2,5-Cl_2BQ/F^- solution in acetonitrile upon increasing F^- conc. at constant 10.2mM 2,5-Cl_2BQ conc. after subtraction of the separate 2,5-Cl_2BQ spectrum (dashed grey line). Dashed red line shows the 2,5-$Cl_2BQ^{\bullet-}$ spectrum obtained from reduction with TDMAE. F^- conc. from top to bottom (mM): 44.6, 32.2, 22.3, 17.4, 12.4.

All spectral and thermodynamic characteristics for the BQ/X^- interactions that yielded anion-π complexes were compiled and are listed in Table 3-1 (see Chapter 2 for calculation details). The greatest strength of interaction can be seen for the π-acceptor with the largest oxidation potential, DDQ, while the tetrahalo-substituted BQs have equilibrium constants significantly less, and the dichloro-substituted BQs show the weakest interactions.

	Cl^-			Br^-			I^-		
BQs	**λ_{max} (nm)**	**ε ($M^{-1}cm^{-1}$)**	**K_{eq} (M^{-1})**	**λ_{max} (nm)**	**ε ($M^{-1}cm^{-1}$)**	**K_{eq} (M^{-1})**	**λ_{max} (nm)**	**ε ($M^{-1}cm^{-1}$)**	**K_{eq} (M^{-1})**
DDQ	437	5425	76.67	**REDOX REACTIONS**					
BA	382	2472	0.64	451	1166	1.57			
FA	383	2836	2.93	438	2184	3.07			
CA	402	2116	1.02	460	2240	1.12			
2,6-Cl_2BQ	375	1215	0.39	430	1511	0.41	565	1291	0.29
2,5-Cl_2BQ	375	1937	0.25	430	989	0.48	558	712	0.54

Table 3-1. Spectral (λ_{max} in nm) and thermodynamic (ε in $M^{-1}cm^{-1}$, K_{eq} in M^{-1}) characteristics of [BQ, X^-] complexes.

The anion-π complex absorption bands peak wavelengths (λ_{max}) listed in Table 3-1 were converted into energies for all aforementioned interactions of BQs with Cl^-, Br^-, and I^-. Comparing this energy to the difference between the oxidation potential (E_{ox}) of the halide and the reduction potential (E_{red}) of the BQ revealed a clear Mulliken correlation. With the exception of F^-, all BQ interactions with halides had Mulliken correlations that fit well enough to one best fit line (Figure 3-38). This trendline even applied to earlier reported complexes of different π-acceptors with the same halides, including tetracyanopyrazine (TCNE), trinitrobenzene, and o-chloranil. This consistent dependence suggests a uniform charge-transfer character for the [BQ, X^-] complex band, implying the complex is the result of an interaction between the HOMO of X^- and the LUMO of BQ. In contrast, the energies of the absorption bands which appeared upon interactions of BQs with F^- deviate substantially from this pattern.

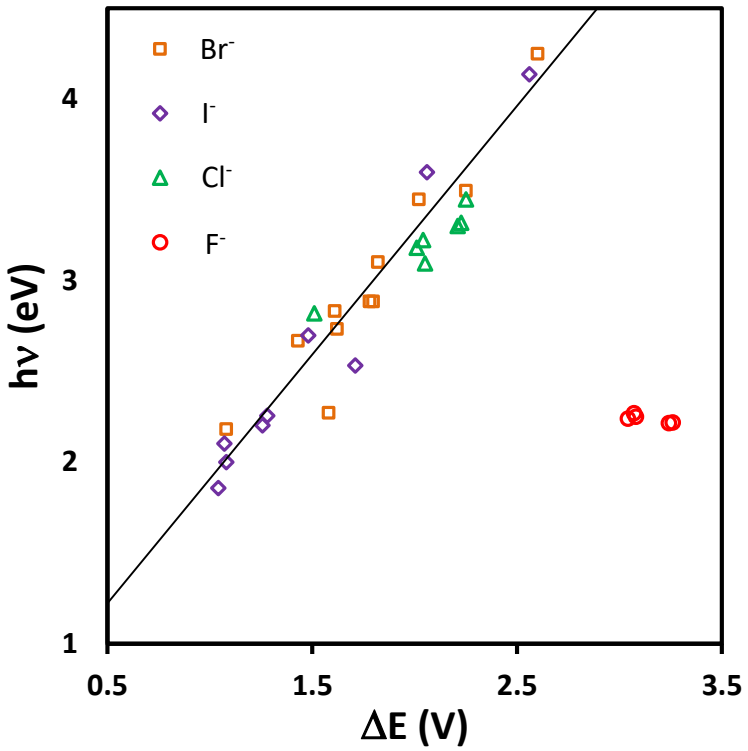

Figure 3-38. Mulliken correlation between the energy of absorption bands of [BQ, X^-] complexes and the difference between the redox potentials of interacting species ($\Delta E = E_{X\text{-}/X\bullet} - E_{A\text{-}\bullet/A}$). Red circle markers represent F^- interactions with different π-acceptors, which do not follow the same trend as their interaction with the other X^-s.

Quantum mechanical computations carried out by Dr. Rosokha confirmed that the nature of the F^- interaction with BQs was different from the other halides studied. While Cl^-, Br^-, and I^- form anion-π complexes with BQs, F^- forms σ-complexes (Meisenheimer complexes) with BQs. These σ-complexes are adducts, with fluorine covalently bonded to the BQ, and DFT calculations produced three different viable configurations for the structure of these complexes (Figure 3-39).

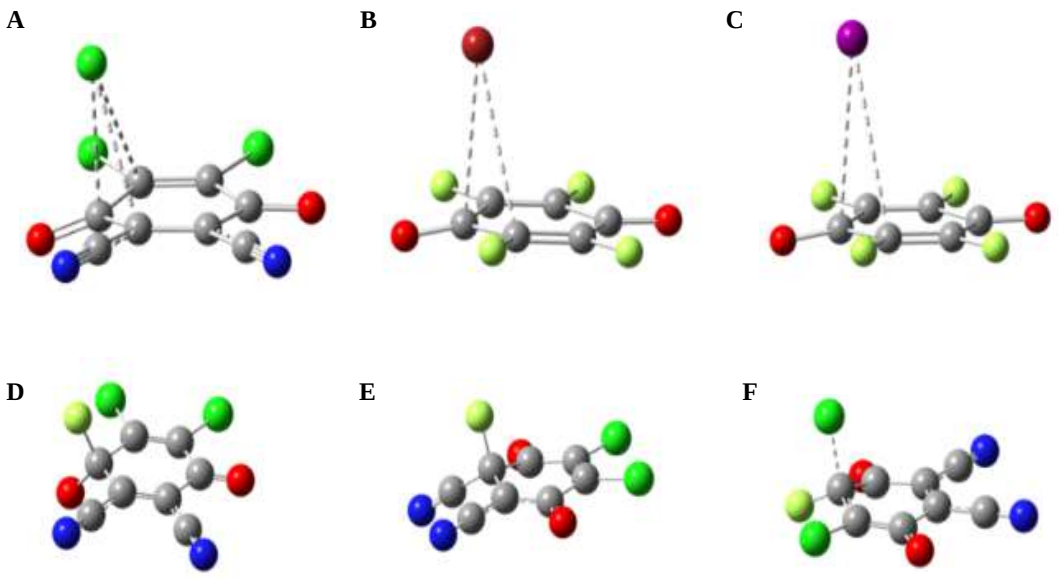

Figure 3-39. Different complexes of DDQ with halide anions obtained from DFT calculations. Anion-π complexes between DDQ and Cl^- (A), Br^- (B) and I^- (C) and σ-complexes resulting from solutions of DDQ and F^-, with fluorine bonded to different carbons of p-benzoquinone ring (D-F).

III. Thermodynamics of charge-transfer to electron-transfer transition

The discovery of the anion-π complexes following a Mulliken correlation raised the question about their role in electron-transfer reactions, where the result of BQ/X^- interactions was the formation of the respective radical anion. As can be seen from Figure 3-38, when ΔE, the difference between the oxidation potential of X^- and the reduction potential of BQ, is less than or equal to 1V, redox reactions are observed. Differences of that magnitude suggest that electron transfer from X^- to BQ is endergonic with a ΔG of about 96 kJ/mol, calculated using Equation 3-3:

$$\Delta G = -nF(E_{red} - E_{ox}) \qquad \text{(Equation 3-3)}$$

where n is the number of electrons transferred per mole of reagent, F is Faraday's constant (kJ/V), E_{red} is the reduction potential of the BQ (V), and E_{ox} is the oxidation potential of the of the X^- (V). This ΔG corresponds to a negligibly small equilibrium constant (K_{eq} = ~10^{-17} M) according to Equation 3-4:

$$K_{eq} = e^{\frac{-\Delta G}{RT}} \quad \text{(Equation 3-4)}$$

where R is the gas constant (J/K•mol) and T is the temperature (K). Therefore, only a very small concentration of $BQ^{\bullet-}$ could be formed following Equation 3-5:

$$BQ + X^- \rightleftharpoons BQ^{\bullet-} + X^{\bullet} \quad \text{(Equation 3-5)}$$

However, oxidation potentials for processes resulting in dihalogens (X^-/X_2) and trimer anions (X^-/X_3^-) are much lower than that the corresponding transition to radical species ($X^-/X^{\bullet}$). For example, the $I^-/I^{\bullet}$ oxidation potential is 1.06V vs. SCE in acetonitrile, while the I^-/I_2 and I^-/I_3^- oxidation potentials in the same solvent are 0.27V and 0.06V vs. SCE respectively. This suggests that the thermodynamics of the reactions of BQs with X^- favors the formation of X_2 (Equation 3-6) or X_3^- (Equation 3-7).

$$BQ + X^- \rightleftharpoons BQ^{\bullet-} + \frac{1}{2}X_2 \quad \text{(Equation 3-6)}$$

$$BQ + X^- \text{(excess)} \rightleftharpoons BQ^{\bullet-} + X_3^- \quad \text{(Equation 3-7)}$$

Since the oxidation potentials of both I_2 and I_3^- are lower than the reduction potential of DDQ (0.52V vs. SCE in acetonitrile), almost quantitative formation of $DDQ^{\bullet-}$ occurs. Meanwhile, reduction potentials for BA, FA, and CA (0.02V, -0.01V, and -0.02V vs. SCE in acetonitrile, respectively) are slightly less than the oxidation potential of I^-/I_3^-, attributing to the lower yields of their radical anions. The dichloro-substituted BQs (2,6-Cl_2BQ and 2,5-Cl_2BQ) have the most negative reduction potentials (-0.18V and -0.2V vs. SCE in acetonitrile respectively), which are more negative than even the I^-/I_3^- couple (0.02V vs. SCE in acetonitrile), so hardly any radical anion is formed.

The Br^-/Br_3^- and Br^-/Br_3^- transitions are 0.3V – 0.4V more positive than their corresponding iodide couples. Consequently, only DDQ can interact to form a significant amount of radical anion through Equation 3-7, but the yield of these reactions will be noticeably lower than a reaction with I^- at the same concentrations.

All F^- transitions are much more positive than either I^- or Br^-, so direct reduction of any BQ through the mechanisms outlined in Equations 3-5 through 3-7 are thermodynamically prohibited. The fact that the BQ/F^- interaction resulted in formation of radical anions for many of the BQs studied signifies there must be other pathways to electron transfer. F^- is the strongest base and best nucleophile of all halides in the solvents used for these studies (all aprotic organic solvents). In a study discussed in Chapter 1, it was shown to have similar properties to hydroxide anions where both were confirmed to reduce BQs to their radical anion.[23] An earlier study demonstrated that addition of hydroxide or alkoxide anions to solutions of p-benzoquinone resulted in formation of anion-radicals of these acceptors by first forming a strong covalent bond to BQ and forming an adduct.[30] The detailed product and kinetic analysis which was done in their thorough work unequivocally proved that the "RO-adduct anion of p-benzoquinone is a real electron donor, and that RO^- is acting as a very strong base or nucleophile rather than a one-electron reductant in an aprotic solvent, such as MeCN". Apparently, the F^- anions react with p-benzoquinones in a similar way.

The proposal that F^- is working as a nucleophile is supported by analysis of the HOMO energies of the halides. HOMO energies decrease in order ($I^- > Br^- > Cl^- > F^-$), which correlates very well with the changes of oxidation potentials. HOMO energies of anion-π complexes are slightly lower than that of the separated anions (which is expected based on the Mulliken theory of charge-transfer complexes), but the order is the same. The HOMO energy of σ-complexes where F^- acts to replace a bonded halogen on a carbon in the BQ are higher not only than the HOMO energy of separate F^-, but also the HOMO energy of separate I^-, making these σ-bonded complexes stronger reducing agents than any X^-, allowing it to easily reduce available BQs. Moreover, the higher yield of radical anions observed in the interaction of the dichloro-substituted BQs with F^- than in solutions with the stronger BQ acceptors is also consistent with the relative yields of radical anions obtained in systems with alkoxide anions.[30] So, appearance of radical anions in BQ/F^- interactions is due to fluoride's strong nucleophilic character, resulting in the formation of σ-complexes.

CONCLUSIONS

1. UV-Vis studies demonstrated that interaction of p-benzoquinone acceptors with Cl^-, Br^-, and sometimes with I^- in solution results in the formation of complexes via anion-π bonding. X-ray structural analysis showed that halides involved in these complexes were located over the p-benzoquinone ring.
2. Formation constants of the anion-π complexes increased and interatomic separations decreased as the p-benzoquinone reduction potential increased. This indicated that the strength of the anion-π bonding is related primarily to the π-acceptor strength.
3. The anion-π complexes between p-benzoquinone acceptors and I^-, Br^-, or Cl^- anions showed intense absorption bands in the visible and near-UV range. Energies of these absorption bands exhibited a Mulliken correlation with the difference in redox potentials of the interacting donors and acceptors. This points to a charge-transfer character of the anion-π complexes.
4. Besides increased formation constants and ground-state charge transfer in anion-π complexes, the interaction of stronger acceptors with I^- or Br^- in solution led to the appearance of the radical anions ($BQ^{\bullet-}$). Analysis of the redox potentials of $BQ/BQ^{\bullet-}$, $X^-/X^\bullet$, X^-/X_2, and X^-/X_3^- couples established the favorable thermodynamics for electron-transfer processes leading to formation of X_3^- and $BQ^{\bullet-}$ in solutions of strong donors and acceptors and made it possible to account for the transition from reversible formation of anion-π complexes to redox reactions. Kinetics of the reactions suggested that anion-π complexes play a critical role as intermediates in these redox processes.
5. UV-Vis spectral studies also demonstrated that p-benzoquinones form different types of complexes with F^- anions (similar to associates of fluoride with the other π-acceptors). Quantum-mechanical computations showed that they are σ-bonded (Meisenheimer) complexes. Follow-up reactions of these complexes led to the appearance of the radical anions in BQ/F^- solutions.

REFERENCES

1) Frontera, A.; Gamez, P.; Mascal, M.; Mooibroek, T. J.; Reedijk, J. Putting anion-π interactions into perspective. *Angew. Chem., Int. Ed.* **2011**, *50*, 9564-9583.
2) Schalley, C. A. Analytical Methods in Supramolecular Chemistry. **2007**, 1-16.
3) Quinonero, D.; Garau, C.; Rotger, C.; Frontera, A.; Ballester, P.; Costa, A.; Deya, P. M. Anion-Pi Interactions: Do They Exist? *Angew. Chem., Int. Edit.* **2002**, *41*, 3389–3392.
4) Schottel, B. L.; Chifotides, H. T.; Dunbar, K. R. Anion-π Interactions. *Chem. Soc. Rev.* **2008**, *37*, 68–83.
5) Grounds, O.; Zeller, M., Rosokha, S. V. Structural preferences in strong anion–π and halogen-bonded complexes: π- and σ-holes vs. frontier orbitals interaction. *New Journal of Chemistry* **2018**, *42*, 10572-10583.
6) Rosokha, Y. S.; Lindeman, S. V.; Rosokha, S. V.; Kochi, J. K. Halide recognition through diagnostic "anion-π" interactions: molecular complexes of Cl-, Br-, and I- with olefinic and aromatic π-receptors. *Angew. Chem., Int. Ed.* **2004**, *43*, 4650-4652.
7) Berryman, O. B.; Hof, F.; Hynes, M. J.; Johnson, D. W. Anion–π interaction augments halide binding in solution. *Chem. Commun.* **2006**, *5*, 506-508.
8) Gorteau, V.; Bollot, G.; Mareda, J.; Perez-Velasco, A.; Matile, S. Rigid Oligonaphthalenediimide Rods as Transmembrane Anion−π Slides. *J. Am. Chem. Soc.* **2006**, *128*, 14788-14789.
9) Aragay, J.; Frontera, A.; Lloveral V.; Vidal-Cancedo, J.; Ballester, P. Different Nature of the Interactions between Anions and $HAT(CN)_6$: From Reversible Anion−π Complexes to Irreversible Electron-Transfer Processes ($HAT(CN)_6$ = 1,4,5,8,9,12-Hexaazatriphenylene). *J. Am. Chem. Soc.* **2013**, *135*, 2620-2627.
10) Giese, M.; Albrecht, M.; Rissanen, K. Experimental Investigation of Anion-Pi Interactions - Applications and Biochemical Relevance. *Chem. Commun.* **2016**, *52*, 1778–1795.
11) Berryman, O. B.; Sather, A. C.; Hay, B. P.; Meisner, J. S.; Johnson, D. W. Solution Phase Measurement of Both Weak σ and C−H···X− Hydrogen Bonding Interactions in Synthetic Anion Receptors. *J. Am. Chem. Soc.* **2008**, *130*, 10895–10897.
12) Chifotides, H. T.; Schottel, B. L.; Dunbar, K. R. The π-Accepting Arene $HAT(CN)_6$ as a Halide Receptor through Charge Transfer: Multisite Anion Interactions and Self-Assembly in Solution and the Solid State. *Angew. Chem., Int. Ed.* **2010**,*49*, 7202–7207.
13) Huynh, M. T.; Anson, C. W.; Cavell, A. C.; Stahl, S. S.; Hammes-Schiffer, S. Quinone 1 e^- and 2 e^-/2 H^+ Reduction Potentials: Identification and Analysis of Deviations from Systematic Scaling Relationships. *J. Am. Chem. Soc.* **2016**, *138*, 15903–15910.
14) Søballe, B.; Poole, R. K. Microbial ubiquinones: multiple roles in respiration, gene regulation and oxidative stress management. *Microbiology* **1999**, *145*, 1817 -1830.
15) Liu, T.; Frith, J. T.; Kim, G.; Kerber, R. N.; Dubouis, N.; Shao, Y.; Grey, C. P. The Effect of Water on Quinone Redox Mediators in Nonaqueous Li-O2 Batteries. *J. Am. Chem. Soc.* **2018**, *140*, 1428-1437.
16) Cheng, M.; Yang, X.; Zhang, F.; Zhao, J.; Sun, L. Efficient Dye-Sensitized Solar Cells Based on Hydroquinone/Benzoquinone as a Bioinspired Redox Couple. *Angew. Chem., Int. Ed.* **2012**, *51*, 9896-9899.
17) Zhu, X-Q.; Wang, C-H.; Accurate estimation of the one-electron reduction potentials of various substituted quinones in DMSO and CH_3CN. *J. Org. Chem.* **2010**, *75*, 5037 – 5047.
18) Lü, J.-M.; Rosokha, S. V.; Kochi, J. K. Stable (long-bonded) dimers via the quantitative self-association of different cationic, anionic, and uncharged π-radicals: structures, energetics, and optical transitions. *J. Am. Chem. Soc.*, **2003**, *125*, 12161-12171.

19) Lü, J.-M.; Rosokha, S. V.; Neretin I. S.; Kochi J. K. Quinones as electron acceptors. X-ray structures, spectral (EPR, UV-Vis) characteristics and electron-transfer reactivities of their reduced anion-radicals as separated versus contact ion pairs. *J. Am. Chem. Soc.*, **2006**, *128*, 16708-16719.
20) Molčanov, K.; Mali, G.; Grdadolnik, J.; Stare, J.; Stilinović, V.; Kojić-Prodić, B. Iodide···π Interactions of Perhalogenated Quinoid Rings in Co-Crystals with Organic Bases. *Crystal Growth & Design* **2018**, *18*, 5182–5193.
21) Torray, H.A.; Hunter, W.H. The action of iodides on bromanil, iodanil and some of its derivatives. *J. Am. Chem. Soc.* **1912**, *34*, 702-716.
22) a) Isse, A.A.; Lin, C. Y.; Coote, M. L.; Gennaro, A. Estimation of standard reduction potentials of haloen atoms and alkyl halides. *J. Phys. Chem.* **2011**, *115*, 678-684. b) Eberson, L. Electron Transfer Reactions in Organic Chemistry; Springer-Verlag: New-York, **1987**, 47. c) Moore, G. F.; Konezny, S. J.; Song, H.; Milot, R. L.; Blakemore, J. D.; Lee, M. L.; Batista, V. S.; Schmuttenmaer, C. A.; Crabtree, R. H.; Brudvig, G. W. Bioinspired High-Potential Porphyrin Photoanodes. *J. Phys. Chem.* **2012**, *116*, 4892–4902. d) Saveant, J.M. Dynamics of Cleavage and Formation of Anion-Radicals into and from Radical and Nucleophiles. Structure-Reactivity Relationships in SRN1 Reactions. *J. Phys. Chem.* **1994**, *98*, 3716 – 3724.
23) Saha, S.; Guha, F.S.; Goodson, L.J.; Corson, L. J. Boundaries of Anion/Naphthalenediimide Interactions: From Anion–π Interactions to Anion-Induced Charge-Transfer and Electron-Transfer Phenomena. *J. Am. Chem. Soc* **2012**, *134*, 13679–13691.
24) Li, J.; Ping, X.; Wang, Y.; Che, Y.; Zhao, J. A new insight into fluoride anion in electron transfer reactions. *Catalysis Today* **2014**, *224*, 258-262.
25) Harmon, K. M.; Gennick, I.; Madeira, S. L.; Duffy, D. L. Hydrogen bonding. III. Tetrapropylammonium hydrogen difluoride and the thermal elimination reaction of tetrapropylammonium fluoride hydrates. *J. Org. Chem*, **1974,** *39*, 2809-2810.
26) Marzotto, A.; Clemente, D. A.; Pasimeni, L. Molecular structure of tetrapropylammonium-2,3-dichloro-5,6-dicyano-p-benzoquinone compared to M^+ $TCNQ^-$ (M^+=Rb^+,K^+,Cs^+, or organic cations; $TCNQ^-$=tetracyanoquinomethane) charge-transfer complexes. *J. Crystallogr. Spectrosc. Res.* **1988**, *18*, 545-554.
27) Molčanov, K.; Mou, Z.; Kertesz, M.; Kojić-Prodić, B.; Stalke, D.; Demeshko, S.; Šantić, A.; Stilinović, V. Pancake Bonding in π-Stacked Trimers in a Salt of Tetrachloro-quinone Anion. *Chem. Eur. J.* **2018**, *24*, 8292–8297.
28) Esaka, Y.; Okumura, N.; Uno, B.; Goto, M. Non-aqueous Capillary Electrophoresis of p-Quinone Anion Radicals. *Analytical Sciences*, **2001**, *17*, 99-102.
29) Burkholder, C.; Dolbier, W. R.; Médebielle, M. Tetrakis(dimethylamino)ethylene as a Useful Reductant of Some Bromodifluoromethyl Heterocycles. Application to the Synthesis of New gem-Difluorinated Heteroarylated Compounds. *J. Org. Chem.*, **1998**. *63*, 5385–5394.
30) Fukuzumi, S.; Nakanishi, I.; Maruta, J.; Yorisue, T.; Suenobu, T.; Itoh, S.; Arakawa, R.; Kadish, K. M. Formation of Radical Anions in the Reaction of P-Benzoquinone and C60 with Alkoxide Ions. *J. Am. Chem. Soc.* **1998**, *120*, 6673–6680.

A

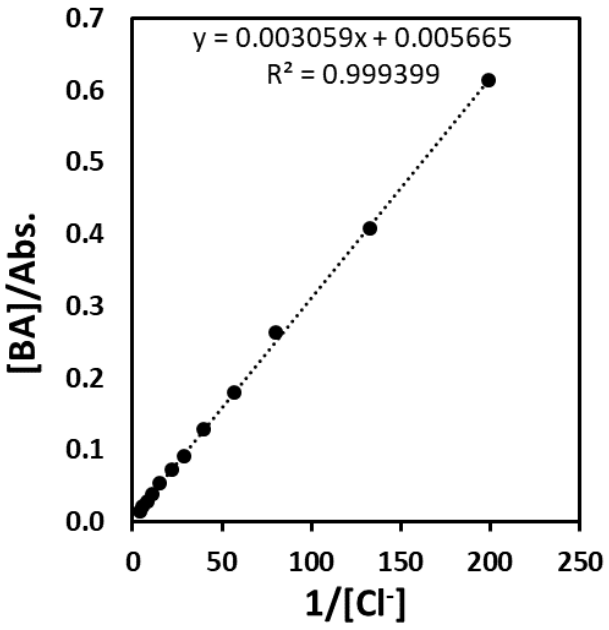

B

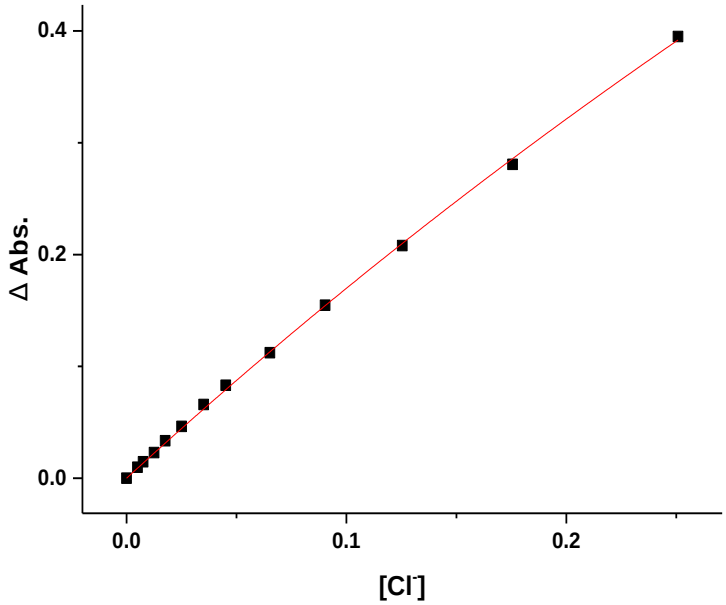

Figure S-1. Graphs using data points obtained from spectral analysis of the BA/Cl^- interaction shown in Figure 3-20A to determine values for k_{eq} and ε. **A)** Benessi-Hildebrand treatment of the BA/Cl^- spectral data along with the equation for the linear best-fit line. **B)** Regression analysis treatment of the BA/Cl^- spectral data.

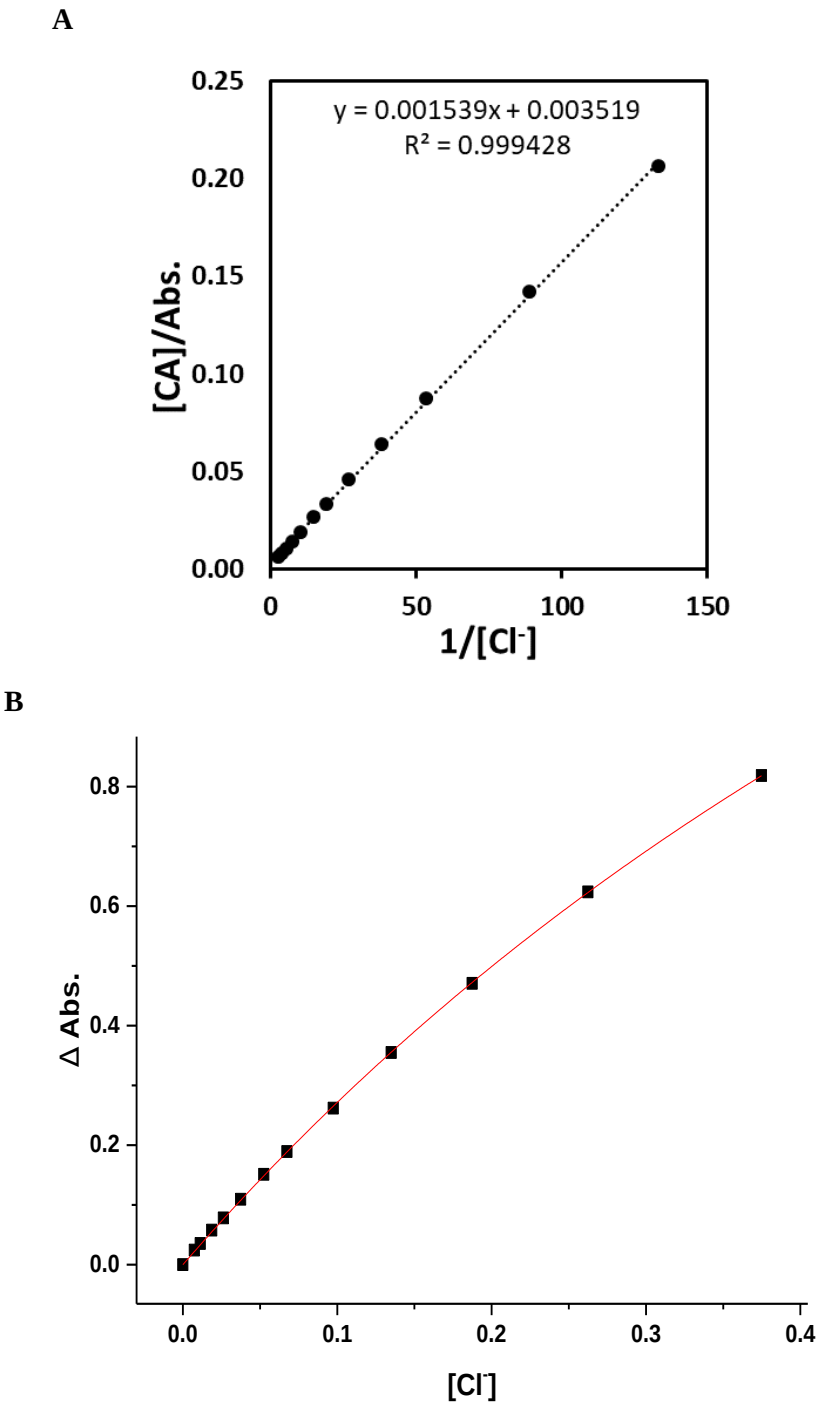

Figure S-2. Graphs using data points obtained from spectral analysis of the CA/Cl^- interaction shown in Figure 3-20B to determine values for k_{eq} and ε. **A)** Benessi-Hildebrand treatment of the CA/Cl^- spectral data along with the equation for the linear best-fit line. **B)** Regression analysis treatment of the CA/Cl^- spectral data.

A

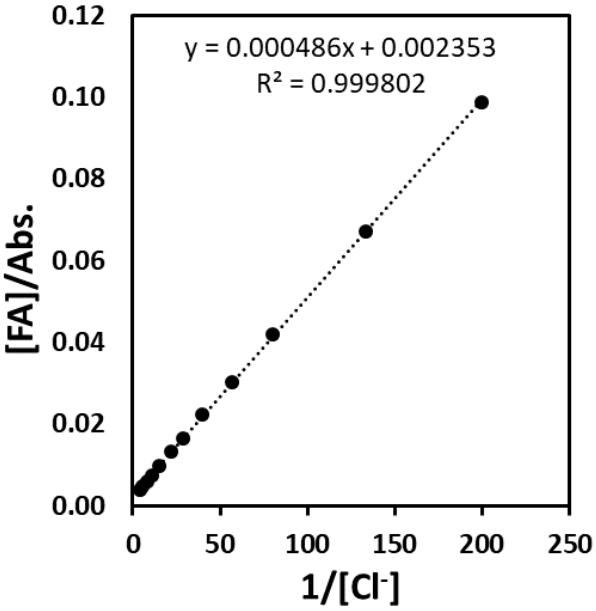

B

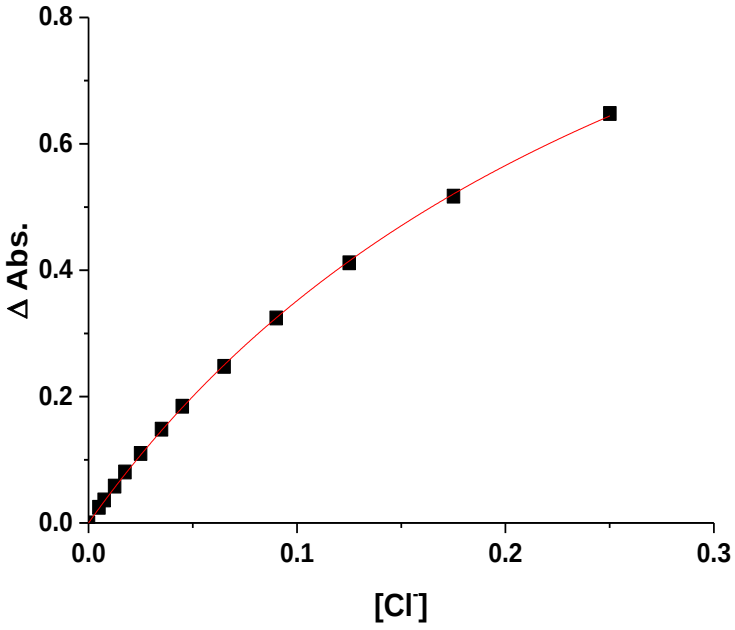

Figure S-3. Graphs using data points obtained from spectral analysis of the FA/Cl^- interaction shown in Figure 3-20C to determine values for k_{eq} and ε. **A)** Benessi-Hildebrand treatment of the FA/Cl^- spectral data along with the equation for the linear best-fit line. **B)** Regression analysis treatment of the FA/Cl^- spectral data.

A

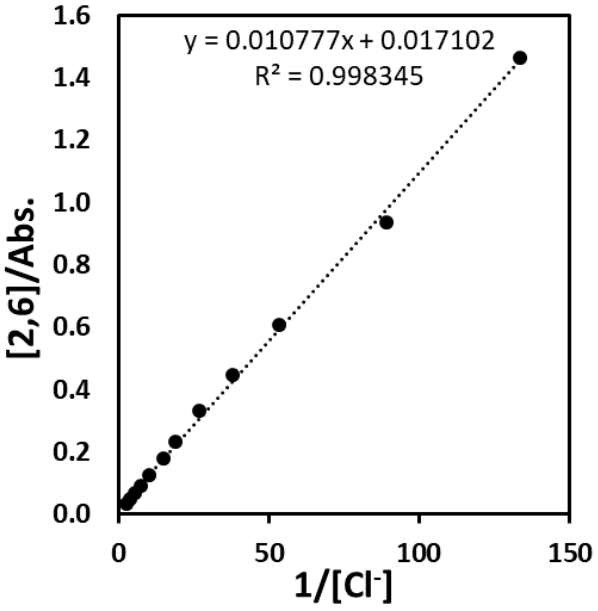

B

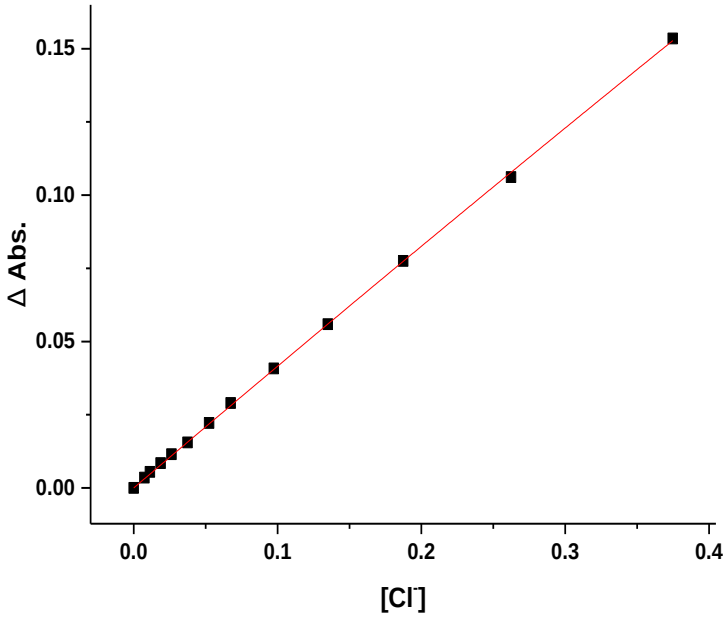

Figure S-4. Graphs using data points obtained from spectral analysis of the 2,6/Cl^- interaction shown in Figure 3-25A to determine values for k_{eq} and ε. **A)** Benessi-Hildebrand treatment of the 2,6/Cl^- spectral data along with the equation for the linear best-fit line. **B)** Regression analysis treatment of the 2,6/Cl^- spectral data.

A

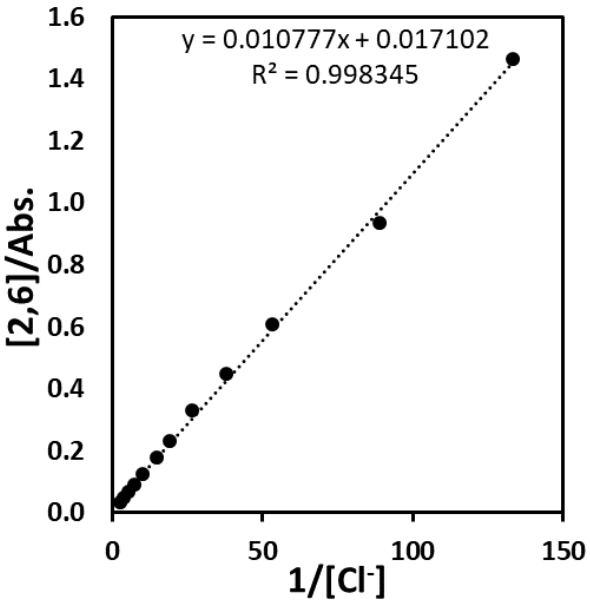

B

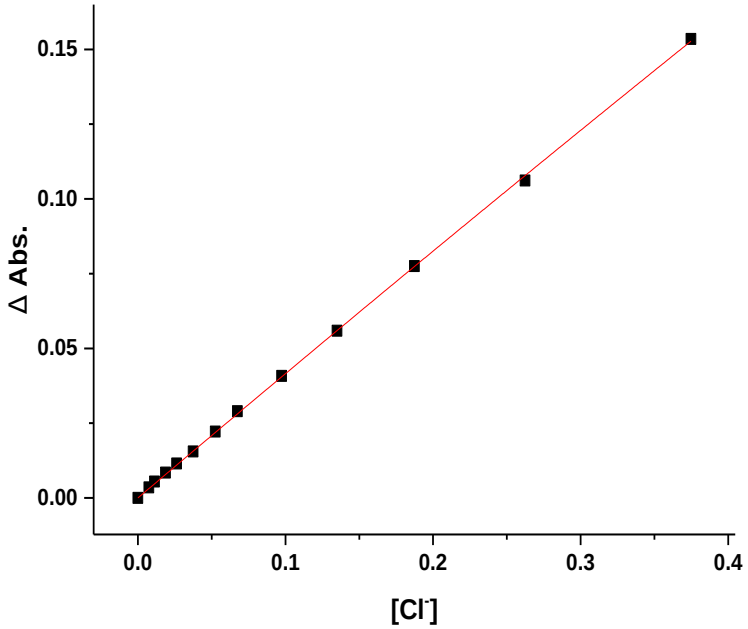

Figure S-5. Graphs using data points obtained from spectral analysis of the 2,5/Cl^- interaction shown in Figure 3-26A to determine values for k_{eq} and ε. **A)** Benessi-Hildebrand treatment of the 2,5/Cl^- spectral data along with the equation for the linear best-fit line. **B)** Regression analysis treatment of the 2,5/Cl^- spectral data.

A

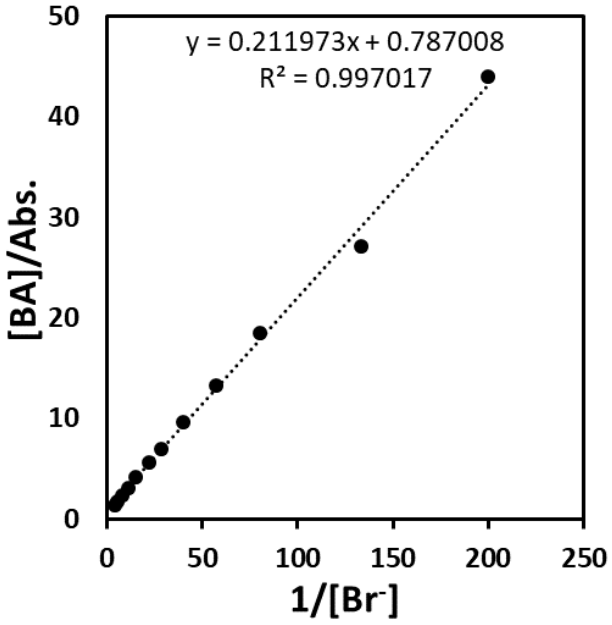

B

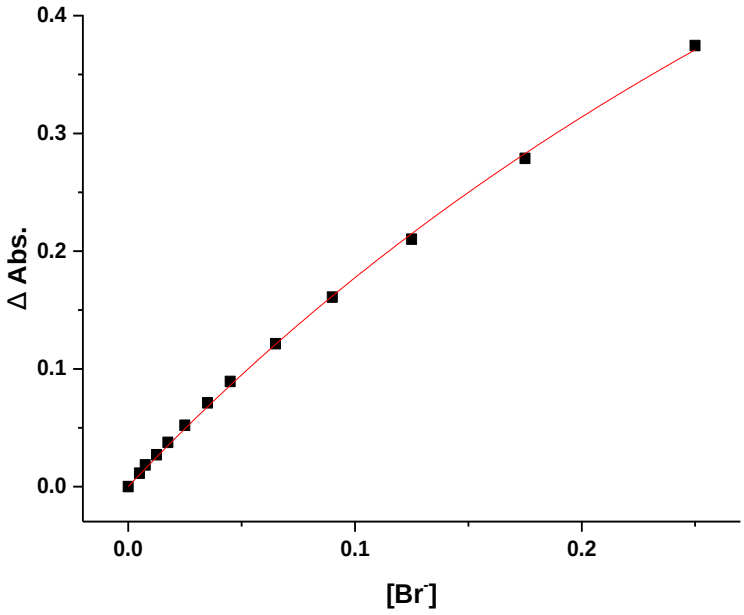

Figure S-6. Graphs using data points obtained from spectral analysis of the BA/Br^- interaction shown in Figure 3-21A to determine values for k_{eq} and ε. **A)** Benessi-Hildebrand treatment of the BA/Br^- spectral data along with the equation for the linear best-fit line. **B)** Regression analysis treatment of the BA/Br^- spectral data.

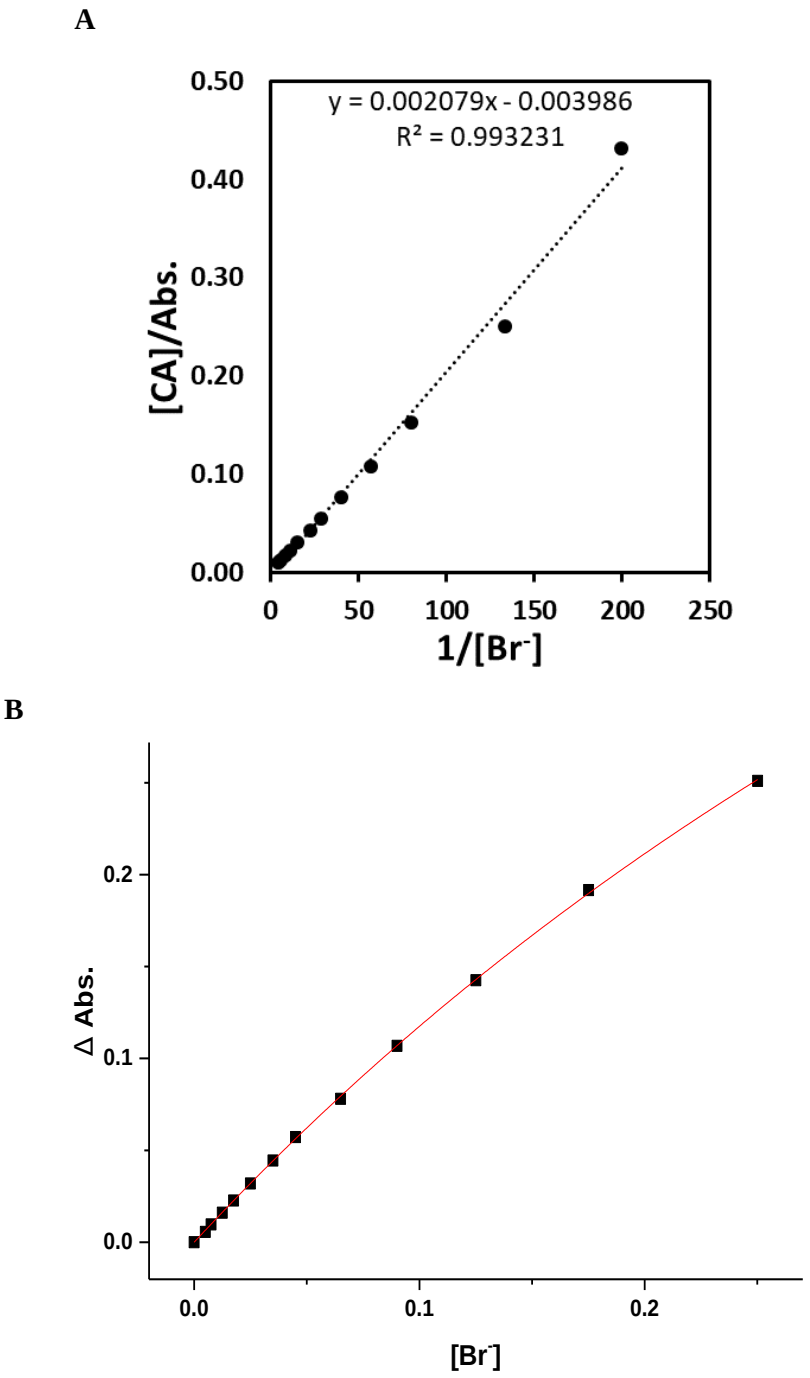

Figure S-7. Graphs using data points obtained from spectral analysis of the CA/Br^- interaction shown in Figure 3-21B to determine values for k_{eq} and ε. **A)** Benessi-Hildebrand treatment of the CA/Br^- spectral data along with the equation for the linear best-fit line. **B)** Regression analysis treatment of the CA/Br^- spectral data.

A

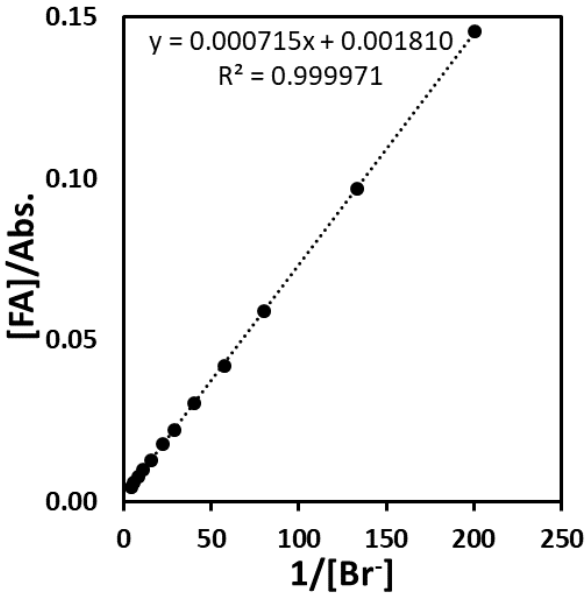

B

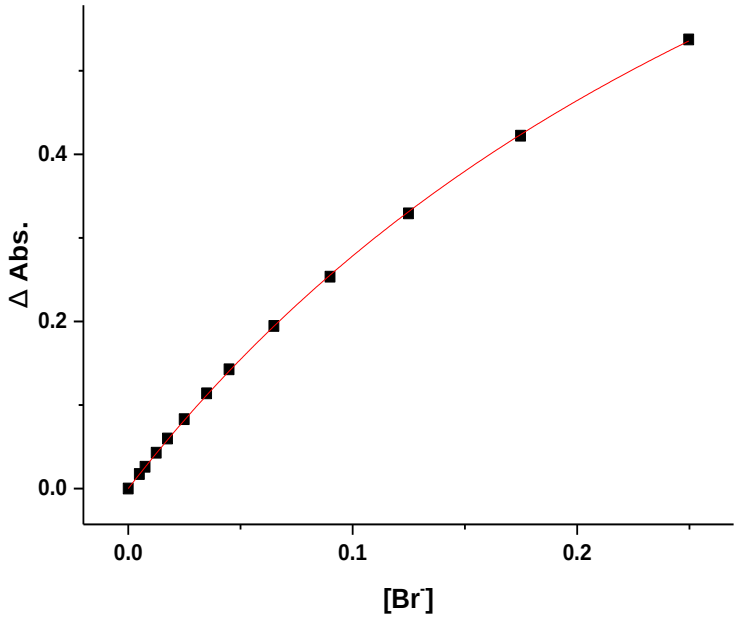

Figure S-8. Graphs using data points obtained from spectral analysis of the FA/Br^- interaction shown in Figure 3-21C to determine values for k_{eq} and ε. **A)** Benessi-Hildebrand treatment of the FA/Br^- spectral data along with the equation for the linear best-fit line. **B)** Regression analysis treatment of the FA/Br^- spectral data.

A

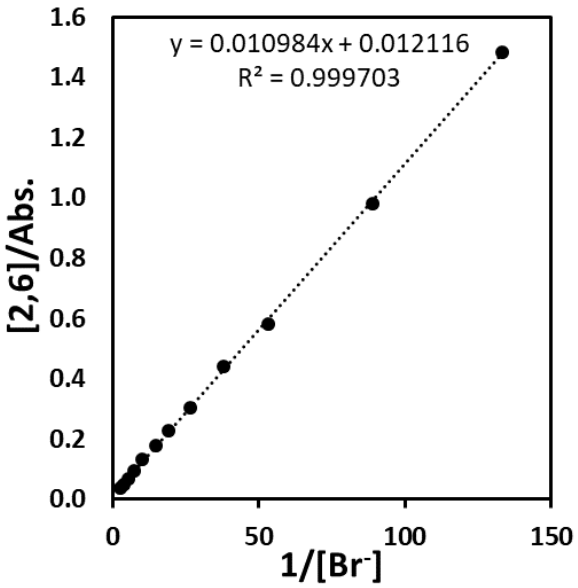

B

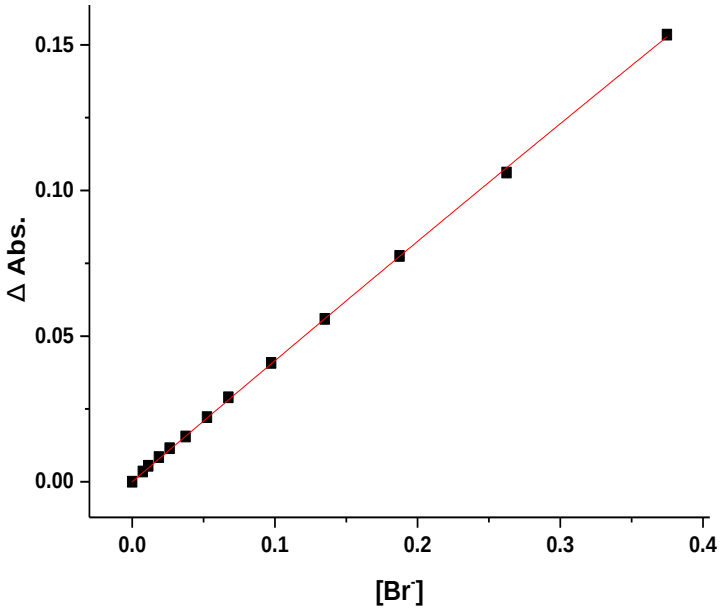

Figure S-9. Graphs using data points obtained from spectral analysis of the 2,6/Br^- interaction shown in Figure 3-25B to determine values for k_{eq} and ε. **A)** Benessi-Hildebrand treatment of the 2,6/Br^- spectral data along with the equation for the linear best-fit line. **B)** Regression analysis treatment of the 2,6/Br^- spectral data.

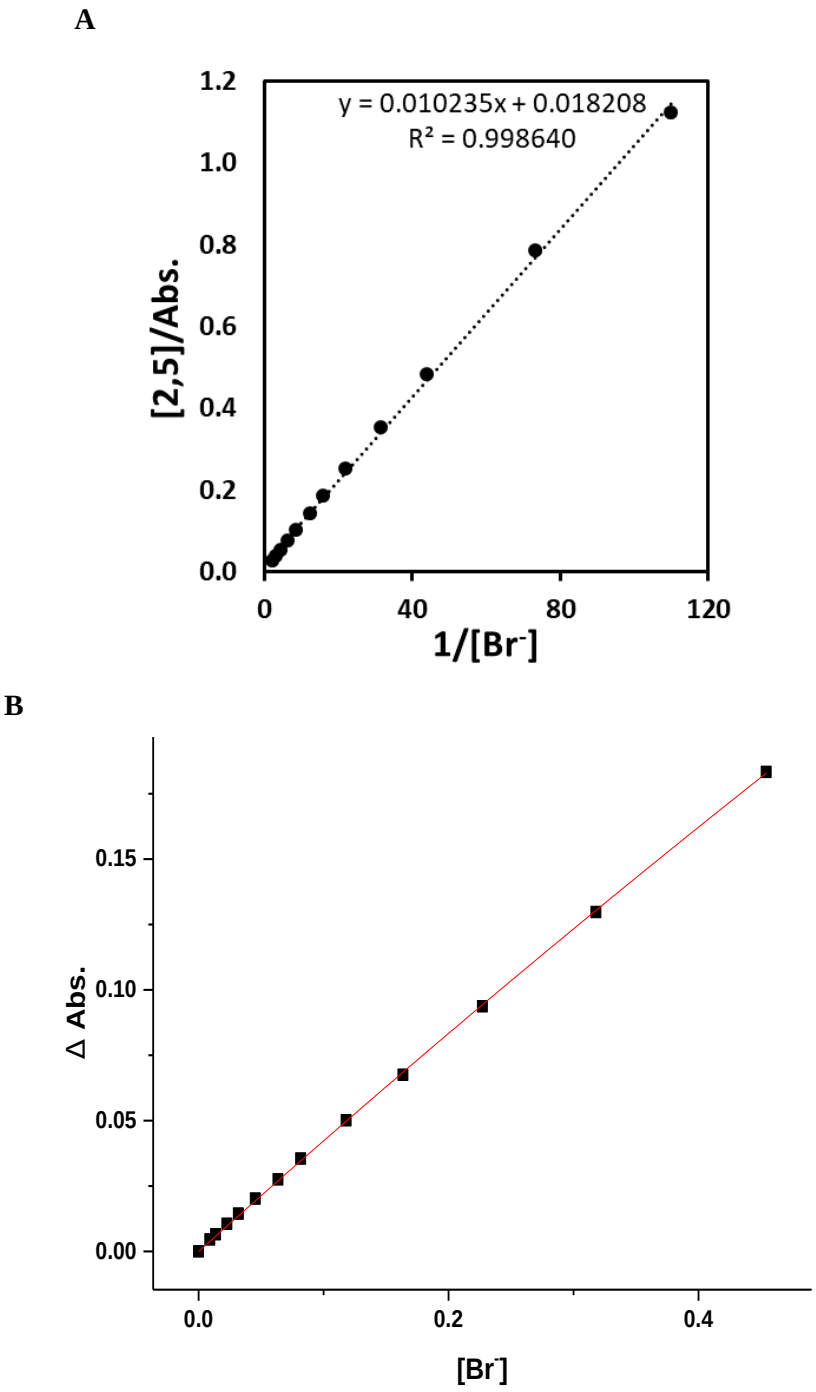

Figure S-10. Graphs using data points obtained from spectral analysis of the 2,5/Br^- interaction shown in Figure 3-26B to determine values for k_{eq} and ε. **A)** Benessi-Hildebrand treatment of the 2,5/Br^- spectral data along with the equation for the linear best-fit line. **B)** Regression analysis treatment of the 2,5/Br^- spectral data.

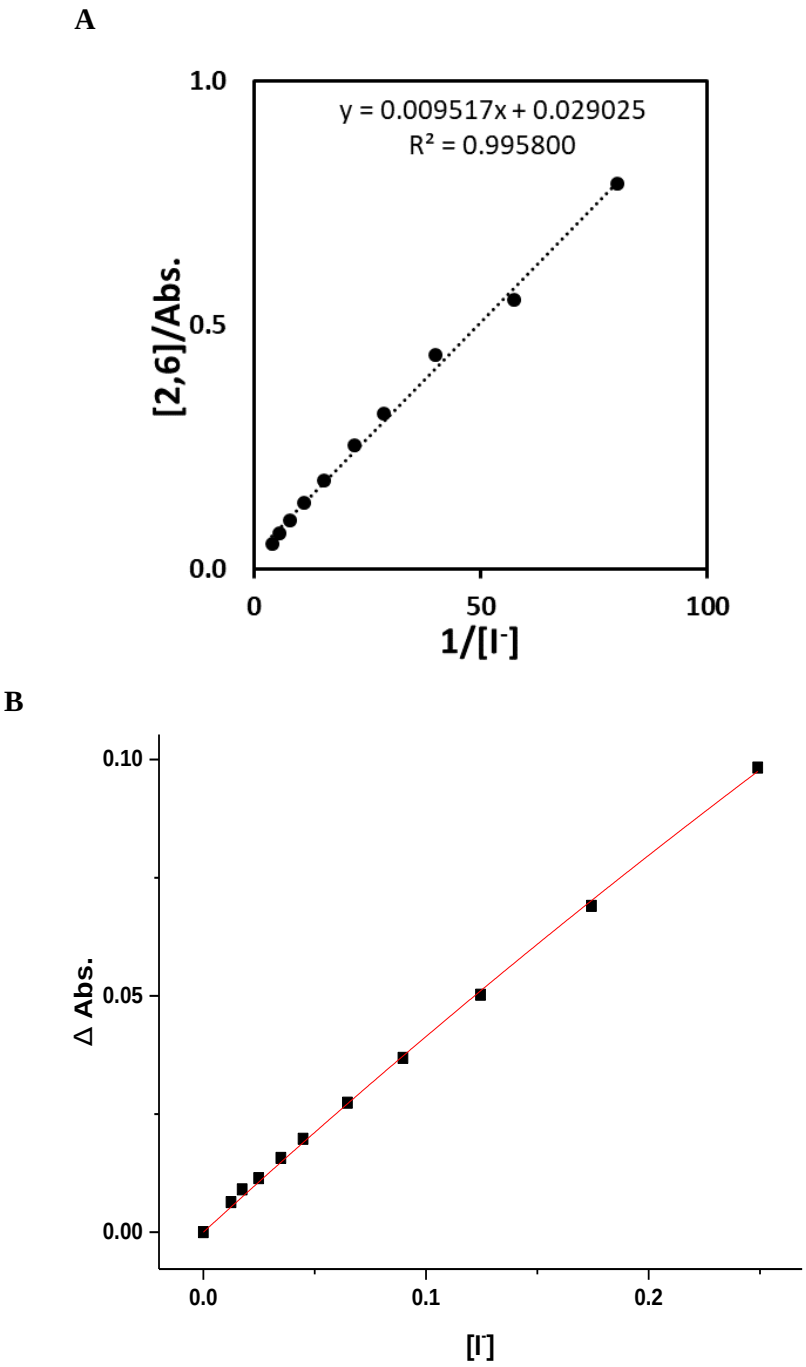

Figure S-11. Graphs using data points obtained from spectral analysis of the 2,6/I^- interaction shown in Figure 3-27A to determine values for k_{eq} and ε. **A)** Benessi-Hildebrand treatment of the 2,6/I^- spectral data along with the equation for the linear best-fit line. **B)** Regression analysis treatment of the 2,6/I^- spectral data.

A

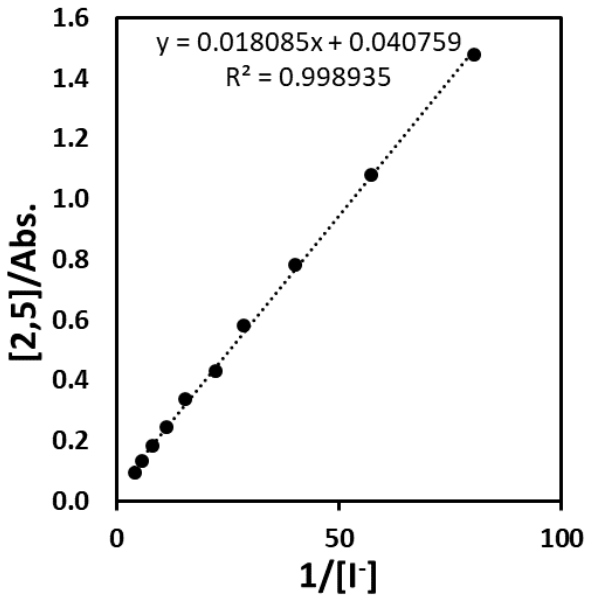

B

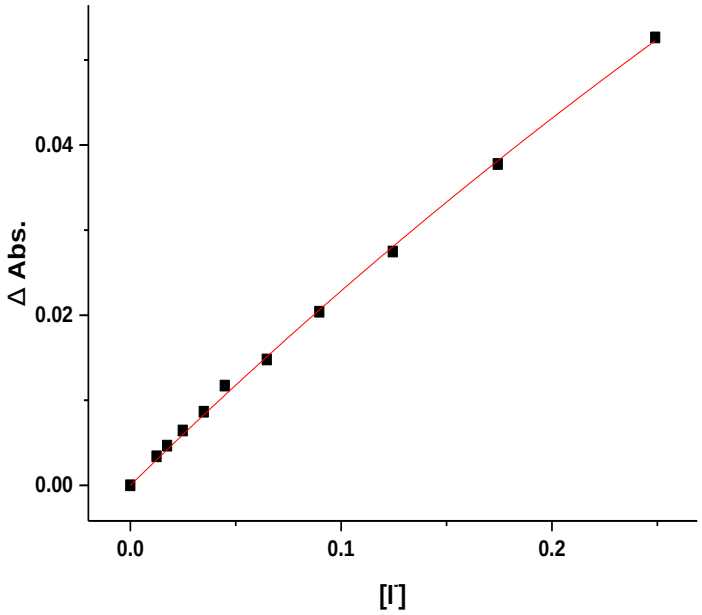

Figure S-12. Graphs using data points obtained from spectral analysis of the 2,5/I^- interaction shown in Figure 3-27B to determine values for k_{eq} and ε. **A)** Benessi-Hildebrand treatment of the 2,5/I^- spectral data along with the equation for the linear best-fit line. **B)** Regression analysis treatment of the 2,5/I^- spectral data.